Star-Cluster Populations and X-ray Binaries in NGC 2276

Student: Panagiotis Kotoulas

Student Identification Number: 5433

Supervisor: Andreas Zezas

Institution: Department of Physics, University of Crete

Abstract

The age and mass of star-cluster populations within a galaxy can be used to trace its star formation history. The spiral galaxy NGC2276, member of the NGC2300 galaxy group, provides an interesting laboratory to study the effects of galaxy harassment on star-formation and cluster populations. The galaxy's west side is compressed due to its super-sonic movement within the intra-group medium, possibly triggering star formation (Rasmussen et al., 2006; Wolter et al., 2015). This asymmetry is evident both in optical and X-ray images, with the west side having an X-ray luminosity ~ 5 times greater than the east side (Anastasopoulou et al., 2019). We use *Hubble Space Telescope WFC3-UVIS* observations of the galaxy in order to detect the clusters and perform photometry. We estimate the cluster ages by comparing our data to evolutionary tracks obtained by using two different stellar population synthesis models; one utilizing the MIST and the other the BPASS isochrones. We estimate that most of the clusters have ages $\sim 10 - 100$ Myrs, while the BPASS model seems to be in better agreement with our data. Using spectral energy distribution fits we are able to derive the age, mass and extinction for a selection of clusters. Ages fall within the $10 - 100$ Myr range, while masses fall in the $10^3 - 10^5 M_{\odot}$ range. The MIST model indicates that the east region clusters might experience smaller extinction in contrast to clusters located in other regions. Cluster masses and ages are consistent between different regions. Finally, we match the X-ray sources catalogue of Anastasopoulou et al., 2019 to our clusters catalogue and perform a spectral energy distribution fit for the best matches. In most cases, clusters in the vicinity of X-ray sources have young ages (< 100 Myr) and large masses, indicating that the corresponding X-ray source is likely a High-Mass X-ray Binary.

Contents

1 Introduction

1.1 Cluster Formation

The age of the stellar populations of galaxies provides critical information on the history of the galaxy and the formation of its stellar content. Star-cluster populations are an excellent tool for inferring the star-formation history of galaxies.

A cluster is formed when a large molecular cloud undergoes fragmentation and each fragment collapses almost simultaneously giving birth to a large number of stars at approximately the same time. Star-clusters can contain from a dozen to hundreds of thousands of stars. Depending on whether the system is gravitationally bound they are categorized in bound clusters and associations (unbound clusters). The bound clusters have two large subcategories: (a) open clusters (OCs): those are relatively small clusters (containing $\sim$ 10 to $\sim$ 1000 stars) and are usually found near starburst areas of the galaxies, e.g. the spirals, and are located almost exclusively on the galactic plane. Because of that, open clusters are usually young in age. (b) Globular clusters (GCs): those are large clusters ($\sim$ 1000 to $\sim 10^5$ stars) and because of their large number of members, the stars have a spherical distribution (hence the name globular), reflecting the spherical symmetry of the gravitational potential. Those are found near the center of most galaxies and the halo. Usually the ones near the center are richer in metals than the ones found in the halo (Zinn and R., 1985). The progenitors of GCs are hypothesised to be young massive star clusters (YMCs), which are clusters with ages $\leq$ 100 Myr, and more massive than $\sim 10^4\, M_\odot$. These are associated with high X-ray luminosity sources (Zwart et al., 2010).

1.2 X-ray Binaries

X-ray binaries (XRBs) are also closely linked with the stellar populations present in a galaxy (Zezas et al., 2008; Gilfanov et al., 2023). These systems are comprised by a compact object (either a neutron star or a black hole) and a companion star (usually a main sequence star) which is also known as the donor star. Matter from the donor star flows towards the compact object, leading to the creation of an accretion disc (see figure 1). This material usually forms an accretion disc as matter flows to the compact object, releasing gravitational energy which heats up the disk up to X-ray emitting temperatures.

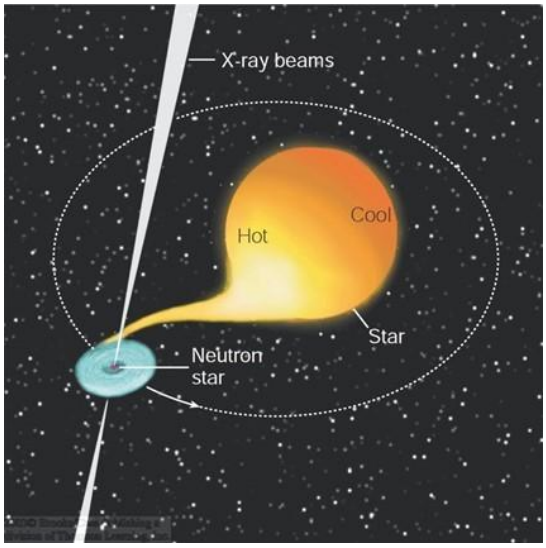

Figure 1: Artistic interpretation of an XRB. The compact object is a neutron star. Mass flows from the donor star to the neutron star resulting to X-ray emission. Credit: Harvard-Smithsonian Center for Astrophysics

XRBs are subcategorized into Low-Mass X-ray Binaries (LMXBs) and High-Mass X-ray Binaries (HMXBs) depending on the companion object's mass (Seward and Charles, 2010). HMXBs have massive companion stars with powerful stellar winds. Those stellar winds are the driving force behind mass transfer (see fig. 2). In contrast, low mass companions have weak stellar winds and matter cannot be transferred that way. The inflow mech-

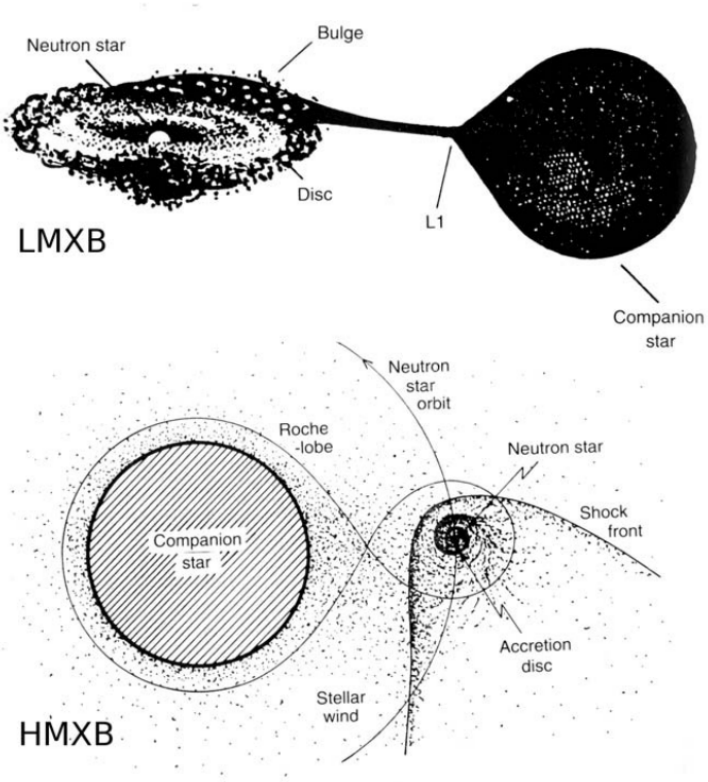

Figure 2: Artistic interpretation of mass inflow in LMXBs versus HMXBs. In the LMXB case, mass is transferred via Roche-lobe overflow, while in HMXBs the donor star is massive enough to create powerful stellar winds. Credit: EXOSAT Observatory, ESA)

anism in this case concerns the system's Roche lobe. The
Roche lobe is defined as the surface on which the gravity of both objects is equal. If the companion star is large enough to fill the Roche lobe, then mass flows through the Lagrange point L_1 (see fig. 3). Roche-lobe overflow can also occur in supergiant systems (which is a subclass of HMXBs). Usually, most starburst galaxies' X-ray emission is dominated by HMXBs.

A rather interesting sub-class of XRBs are Ultra-luminous X-ray sources (ULXs). These sources are extremely bright with X-ray luminosities exceeding $L(0.3-10.0 \text{ keV}) = 10^{39}\text{erg s}^{-1}$. Considering the balance between radiation pressure pushing outwards the outer layers of gas and gravity forcing it to fall onto the compact object, it becomes obvious that there must be a luminosity limit, above which the radiation pressure would be too high and would push excess gas away from the accretion disc. That limit is called the Eddington limit and for spherical accretion it is equal to $1.3 \times 10^{38} M/M_{\odot}$ erg s^{-1} (Seward and Charles, 2010). If we substitute M with $1.4M_{\odot}$ which is a good estimate for the mass of a neutron star, the Eddington luminosity is $\sim 1.8 \times 10^{38}$ erg s^{-1}. Obviously, the ULX luminosity exceeds the Eddington limit, but then we still observe such sources. This phenomenon can be attributed to: (a) non-uniform emission: The classical calculation of the Eddington limit assumes that the source emits radiation uniformly. But if most of the radiation is emitted in a small angle, as can happen for instance in beaming, we would observe a luminosity exceeding the Eddington limit. (b) Accretion involving a stellar mass black hole with $\geq 10M_{\odot}$. Then the Eddington limit for such massive compact objects is above 10^{39} erg s^{-1}, leading naturally to ULX luminosities. What is more interesting is that there are indications of ULXs with

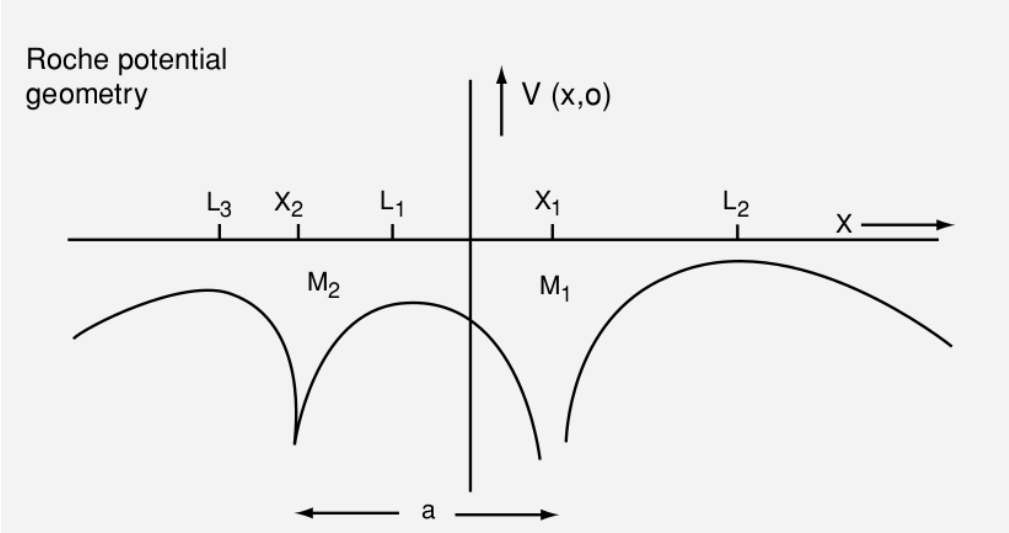

Figure 3: Roche potential on a 2-star system of distance a. L_1 is also known as the Lagrange point 1 and is a point of unstable equilibrium. If the donor's radius exceeds the L_1 point then mass flows through it. This mechanism is known as Roche-lobe overflow. Credit: Seward and Charles, 2010

Intermediate Mass Black Holes (IMBHs; black-holes with masses $100M_{\odot} < M < 100,000M_{\odot}$) as companions. This is important since these objects fall into a relatively gray area of compact object populations that are too massive to form through stellar evolution but not as massive as the supermassive nuclear black holes.

The relevance of XRBs in our study of stellar clusters becomes obvious when we consider the environments that favor their formation. GCs and YMCs contain a very large number of stars and a high compact object density. Given the generally accepted fact that most stars come into binary systems, these clusters seem to pose the perfect environment for XRB creation. Even in the case of lone compact objects, the high stellar density (and especially near the cluster's center) makes it possible for it to either catch a single star or interact with a normal binary system and replace one of the stars. What is more is that there already have been indications of high luminosity XRBs and ULXs being associated with young stellar clusters of ages usually ≤ 10 Myrs (Kaaret et al., 2004; Ptak et al., 2006; Rangelov et al., 2011; Rangelov et al., 2012; Poutanen et al., 2013). Even though they are located near those clusters, most of the time they are not located inside them, suggesting that XRBs might have been ejected from the clusters they were born in via either many-body encounters or by acquiring momentum due to asymmetries in the supernova (SN) explosion that initially created the compact object, a mechanism known as a 'kick' (Zezas and Fabbiano, 2002; Kaaret et al., 2004; Moeckel and Clarke, 2011 Mapelli et al., 2011; Poutanen et al., 2013). Last but not least, if we find an XRB inside a star cluster, and we know that cluster's age, we also know the XRB's age, under the assumption that all stars within a cluster are created in approximately the same age.

1.3 The NGC2276 Spiral Galaxy

NGC2276 is an Sc type starburst galaxy, member of a group comprised of 4-5 other galaxies [1]. The group is gravitationaly dominated by the elliptical galaxy NGC2300. NGC2276 is a relatively nearby galaxy located at a distance of $D \sim 39.97 \pm 2.80$ Mpc [2]. Its major axis length is 1.41 arcmin [3].

The most prominent characteristic of NGC2276 is its asymmetric morphology, resulting from a shock-like feature, present on the galaxy's west side. This is evident in both optical as well as X-ray images (see fig. 4). This feature is likely explained by the supersonic movement of the galaxy within the intra-group medium (IGM) at a speed of $\sim$ 850 km/s, which results to gas-pressure striping as well as viscous striping (Rasmussen et al., 2006). This claim is also supported by Wolter et al., 2015 who used numerical hydrodynamic simulations in a successful attempt to recreate the observed morphology. They assumed a parabolic trajectory for the galaxy, and an initial separation of 170 kpc between the two galaxies. The most prominent effects were observed during the periapsis passage which occurred in 85 Myr (and a minimum separation of 160 kpc was reached). Another 85 Myr later the galaxies reach their current state (again at a separation of 170 kpc). Assuming that a large fraction of the cluster population was created at that time, the age of star-clusters can be used as an order of magnitude test of this interaction model (see Section 3.5). It was also shown that the tidal disruption due to the presence of NGC2300 plays a minimal role, even though it seems to be responsible for the creation of the tidal arms as well as the thickening of the gaseous disc.

The compression of the galaxy resulting from its passing through the IGM of the NGC2300 group, may have triggered star formation and led the formation of young, massive clusters in the compressed side (Rasmussen et al., 2006; Wolter et al., 2015). A qualitative indication of that is evident in the true color images where one can see that the west side of the galaxy seems to host more blue and bright clusters than the east side (fig. 4). This is consistent with the asymmetry also evident in X-ray images, since X-ray sources are correlated with young and massive clusters. Indeed, studies examining the X-ray populations of NGC2276 have detected a large number of X-ray binaries (XRBs) (Anastasopoulou et al., 2019; Wolter et al., 2015). Anastasopoulou et al., 2019 detected 19 point-like X-ray sources with luminosities above 10^{38} erg s^{-1}. What is most impressive is that 11 of these sources are ULXs. This is well above the average number of ULXs for a spiral galaxy which is ~ 1 (Seward and Charles, 2010). Six of them are located on the west side and five on the east side, but the total luminosity of the XRBs on the west side was found to be ~ 5 times greater than on the east side. Even though this could be attributed to a difference in the star formation rate (SFR) in a sub-galactic scale, there are indications that the SFR does not vary significantly over the galaxy (Anastasopoulou et al., 2019).

Regarding the galaxy's metallicity, Wolter et al., 2015 report a metallicity of $Z = 0.22 Z_{\odot}$, based on the integrated spectrum of the galaxy. We adopt this value as our baseline, but since it is relatively low compared to typical metallicities of spiral galaxies, we also explore the effect of higher metallicites in our results.

[1] The other galaxies of the group include NGC2268 and IC455 while whether UCG 03670 belongs in the group is still under debate.

[2] Obtained from NED. The value was calculated using the Virgo infall, Great Attractor and Shapley corrected redshift with a Hubble constant of $H_0 = 67.8$ km/sec/Mpc. We decided to adopt this value since the galaxy's disturbed morphology means that the distance obtained via Tully-Fisher relationships might be untrustworthy.

[3] Value obtained from de Vaucouleurs et al., 1991 where it was calculated using the isophotal method.

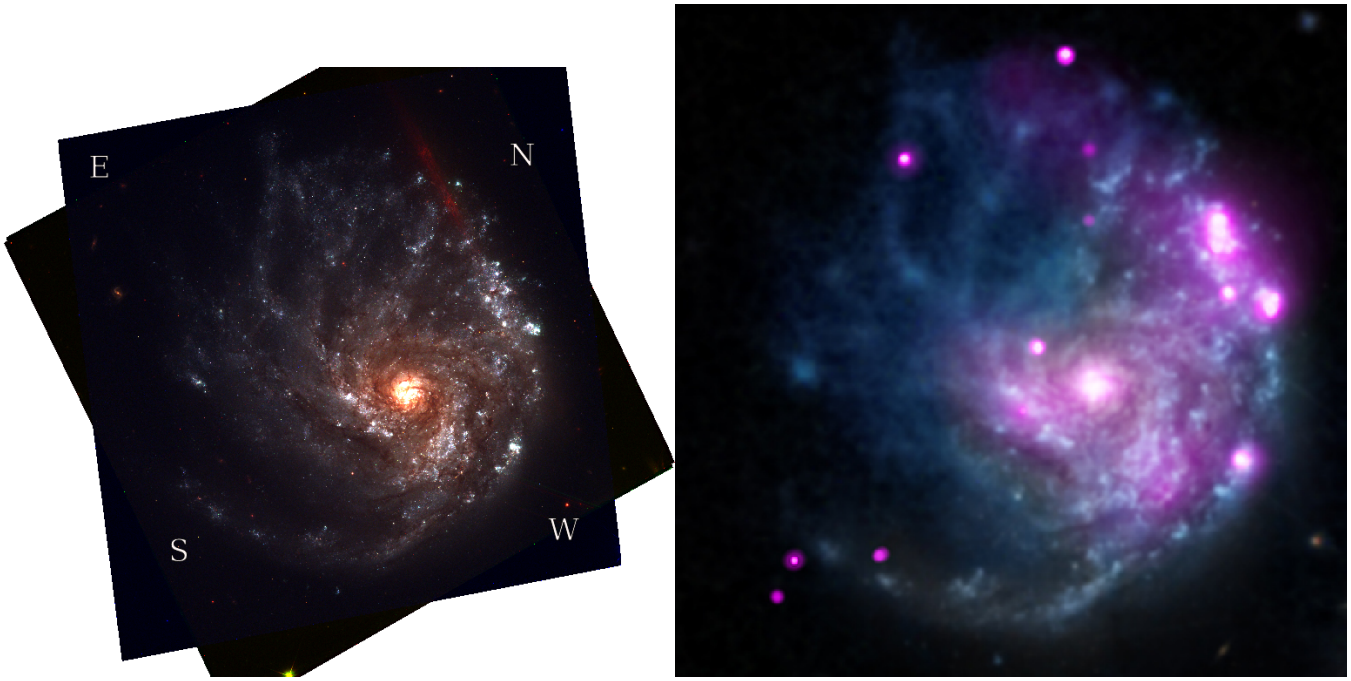

Figure 4: Left: true color image of NGC2276 created using the Hubble Space Telescope observations that were also analysed in the current investigation (see Section 2.2 for more details). Red corresponds to the F814W filter, green to the F555W filter and blue to the F438W filter. The western side spiral has many bright blue sources, indicating recent star formation. Near the north side a region of scattered red light can be seen. This is discussed in Section 2.1. Right: Composite image of optical data (blue) and X-ray data (purple). Many point-like X-ray sources can be seen. Credit: X-ray: NASA/CXC/SAO/M.Mezcua et al & NASA/CXC/INAF/A.Wolter et al; Optical: NASA/STScI and DSS

Studying the stellar populations of starburst galaxies is important since it can help us shed light to galactic evolution. Learning about the conditions under which new populations are born and their initial characteristics, serves as an initial condition when trying to simulate their evolution and derive the properties of older populations. NGC2276 comes with two major additional benefits. One, is having an asymmetrical structure. That structure can be used as a laboratory to study how a recent starburst can affect the stellar populations since the quiescent side of the galaxy provides a direct measure of comparison. Of course it also contains a large number of high X-ray luminosity sources. Investigating possible correlations between population characteristics and the presence of an XRB, is not only interesting because it can indicate what a fertile XRB environment looks like; it can also be used as a guide for future X-ray observations by determining whether a galaxy is a good XRB host candidate based on its stellar populations.

2 Clusters Catalogue

In this section a description of the observations is provided as well as the processing that lead to the creation of the final cluster catalogue.

2.1 Observations

This investigation uses observations of NGC 2276 acquired using the Hubble Space Telescope's WFC3-UVIS detector, in five different filters covering bands from the UV to IR (namely the F275W, F336W, F438W, F555W and F814W filters, whose -arbitrarily normalized- transmission curves are shown in fig. 5). This detector is comprised by two Charge-Coupled Device (CCD) chips. For each filter there are four single-field exposures, covering both of these chips. The (total) field of view of each exposure is 162×162 arcsec. The (average absolute) pixel-scale in the WFC3 detector is 0.039 arcsec/pixel, so assuming a distance of 39.97 ± 2.80 Mpc, one pixel corresponds to 7.56 ± 0.53 pc. Each of those exposures has 699 seconds of exposure time for the F275W and F336W filters and 703 seconds for the F438W, F555W and F814W filters, totalling 2796 seconds and 2812 seconds of exposure time for these filters respectively. The full-width at half maximum (FWHM) of the point-spread functions (PSFs)[4] of the HST-WFC3-UVIS detector. for different wavelengths can be found in table 1.

Wavelength (nm)	FWHM (pixels)	FWHM (arcsec)
200	2.069	0.083
300	1.870	0.075
400	1.738	0.070
500	1.675	0.067
600	1.681	0.067
700	1.746	0.070
800	1.844	0.074
900	1.960	0.078

Table 1: The Full-Width at Half Maximum (FWHM) of the WFC3-UVIS detector's point-source PSFs at different wavelengths.

The observation IDs for each filter (in the above order) are idwx05010, idwx04010, idwx03010, idwx02010 and idwx01010. The data was obtained via the Mikulski Archive for Space Telescopes (*MAST*). We obtained data pre-processed via the CALFW3 pipeline. Charge Transfer Efficiency (CTE) corrections were applied as part of this pre-processing. These corrections account for the charge loss which occurs when the charge is transferred from one pixel to another during readout. Additional processing was done manually, as described in Section 2.2.

The individual exposures for each filter were combined into composite images using the DRIZZLEPAC (Hoffmann et al., 2021) PYTHON package. This code calculates the offsets between the observations and aligns them. It also corrects the images for distortions while it cleans them from bad pixels such as cosmic rays or warm pixels. You can see the individual composite images in fig. 6. Fig. 4 (left) shows a true-color image of the galaxy created using these composite images (red is the F814W composite image, green is the F555W filter and blue is the F438W filter). We can

[4]More on PSFs can be found in C

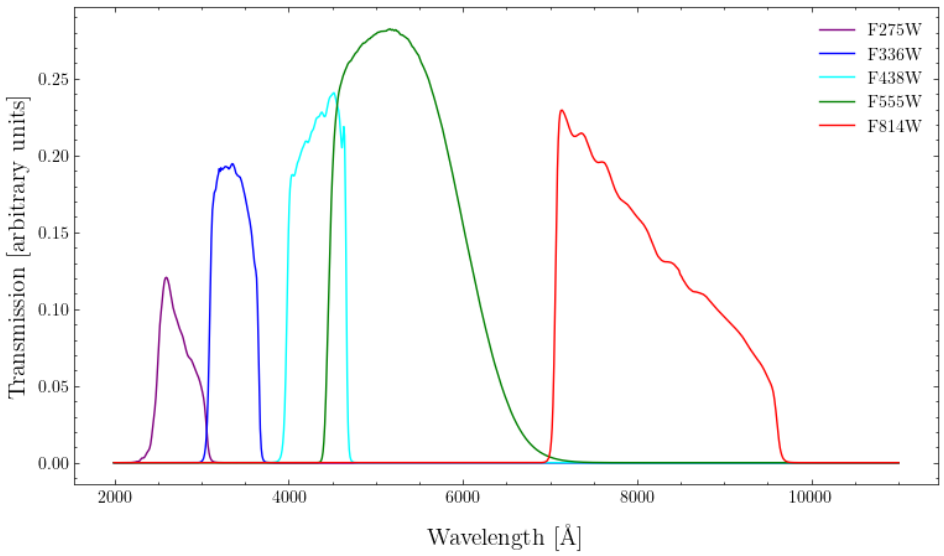

Figure 5: Transmission curves of the HST filters used for acquiring the NGC 2276 photo (arbitrarily normalized).

clearly notice an artifact in the north side of the galaxy. This is shown more clearly in fig. 7. It is also evident but to a much lesser degree in the F555W filter (you can notice it in the F555W image on fig. 6). Due to its appearance, this effect is known as the Dragon's Breath (discussed in more detail in Fowler et al., 2017), and is caused by the scattering of the light of a bright source, that is located just outside the detector. This effect is not negligible and can significantly affect our photometry on the F814W filter. For instance it might lead to an overestimation of the background flux. As discussed later, there is no indication that sources are affected on a large degree by this effect, but we are still cautious when interpreting results for clusters near that area of the detector.

2.2 Data Preparation and Photometry

The next step in our analysis consists of the detection and photometry of the star-clusters. For those tasks, the DOLPHOT code was utilized (Dolphin, 2000, A. Dolphin et al., 2016). DOLPHOT is a specialized code for HST source detection and photometry. It provides an option for aperture photometry as well as Point-Spread Function (PSF) fitting photometry. The greatest benefit of using the PSF fitting mode of DOLPHOT is that it allows the reliable photometry of sources even in mildly confused environments, by using its own library of (quantized) PSFs, created specifically for each detector. It also takes into account the distortion of the PSF in different regions of the detector and filter. This is discussed more thoroughly in C.

Before running DOLPHOT, the data have to be pre-proccesed. This pre-processing is performed on the CTE-corrected exposures which were acquired from the *MAST* database. Each exposure is masked using DOLPHOT's *wfc3mask* routine and then split into two separate files, each of them corresponding to one of the two chips of the detector, using the *splitgroups* routine. Then, using the *calcsky* routine, a map of the background sky is calculated. More details regarding reasoning and the algorithms behind these processes can be found in C.

In order to align and match the detected sources of each exposure, DOLPHOT requires an image to be used as reference. It must contain *World Coordinate System (WCS)* coordinates and

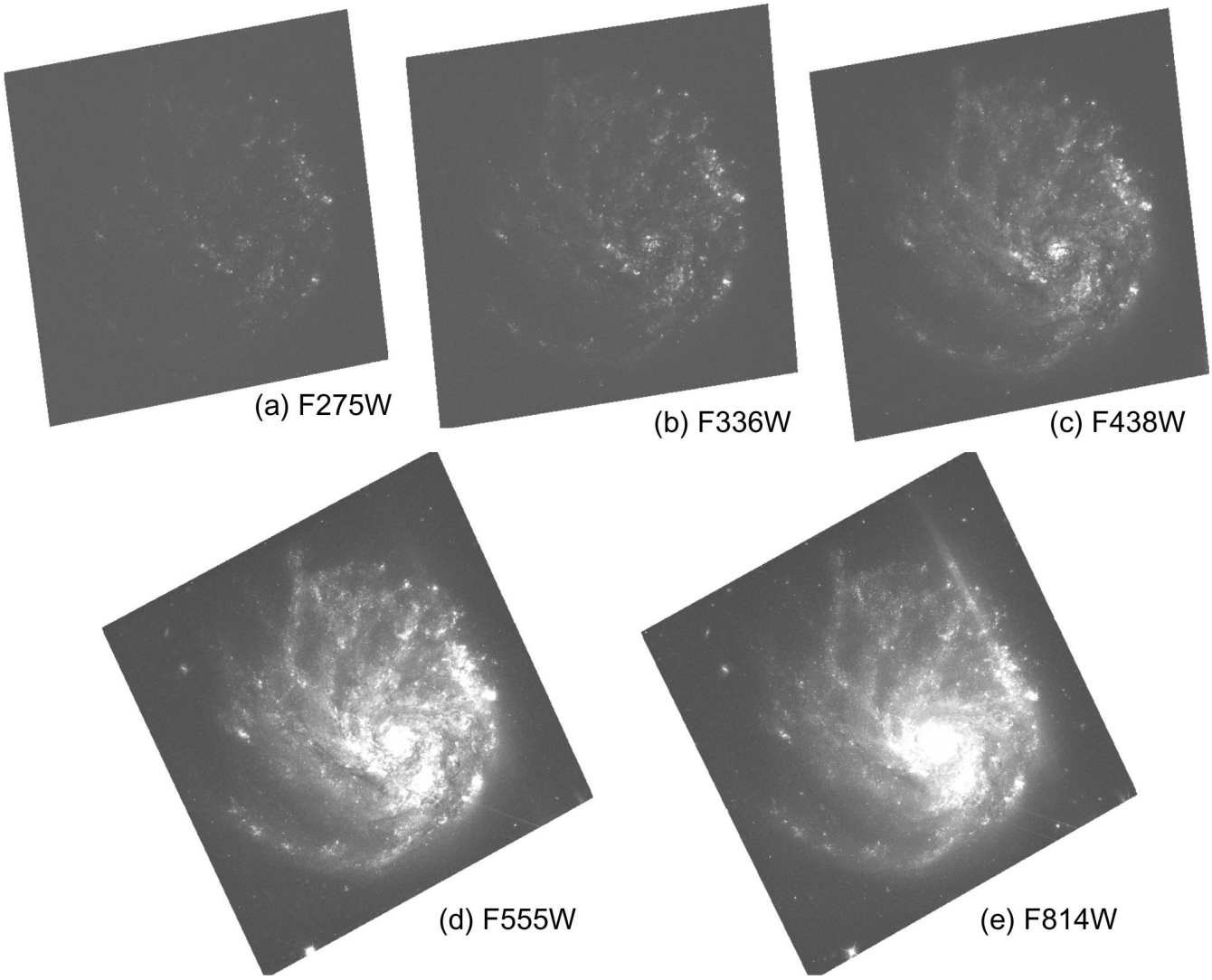

Figure 6: Composite images from the individual exposures for each filter. All images are in the same scale so it is easy to compare their relative brightness. Notice that on that scale the F275W has barely visible sources. That is expected since the UV experiences the greatest dust extinction. An artifact known as the dragon's breath (discussed in Section 2.1) is prominent on the upper right side of the F814W filter composite image. The dragon's breath can also be noticed in the F555W filter, where it is much less prominent. The different orientation of each image is caused by the different rotation of the telescope while obtaining the images.

use *counts* as units. The reference image selected was the deepest one from the composite images created using DRIZZLEPAC, which in our case is the F555W image[5].

Next, DOLPHOT's main module is run to detect the sources and perform the photometry simultaneously at every exposure. Since the field is crowded, the type of photometry was PSF fitting. Using aperture photometry would most likely lead to unintentionally incorporating light from nearby sources resulting in an overestimation of the flux, especially in denser areas of the galaxy such as the galactic center or the compressed west side spiral.

[5]In reality, the F814W image was deeper, but was not used because of the dragon's breath. In the F555W image, even though the dragon's breath is also evident, its brightness is very close to the background so it does not affect the source detection (this is also verified by our residuals as mentioned in 2.3). In any way, the selection of the reference image does not impact our photometry since is used purely for alligning the different exposures.

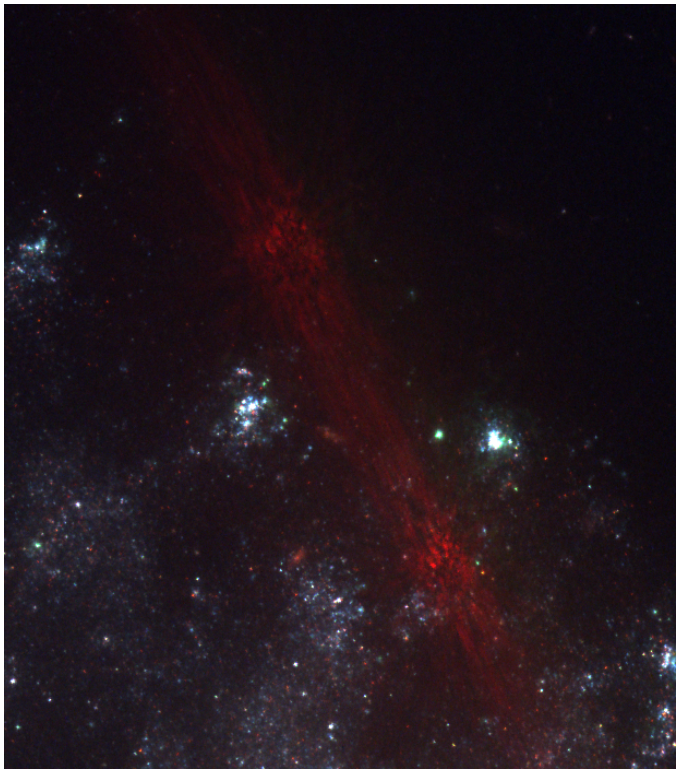

Figure 7: The area of the detector where the dragon's breath appears. The images used for the true color image are the same as in fig. 4 (left).

Most of the parameters for DOLPHOT's source detection algorithm and the photometry were chosen according to the *Dolphot WFC3 User's Guide* (A. Dolphin, 2011) suggestions. The aperture radius to be used for fitting the PSF was set at 3 pixels. The radii defining the inner and outer annulus for the sky are 4 pixels and 10 pixels respectively. Another important parameter is the minimum separation between sources in order for them to be considered separate. This was set, after testing, at 1.5 pixels in order to avoid the combination of separate sources, especially in more crowded areas. The source detection algorithm was ran for 5 iterations to make sure that no sources were missed.

One problem that might arise when using PSF fitting photometry is trying to fit a point source PSF to an extended source. Since NGC2276 is at a distance of ~ 40 Mpc, it is possible that some star-clusters might be partially resolved and appear extended. To obtain an estimate of how much light we miss by trying to fit a point-like PSF to a large cluster at the distance of NGC2276, we calculate aperture corrections on synthetic clusters created with BAOLAB (Larsen et al., 2014). For the cluster effective radius we use a value close to the maximum of the effective radii distribution derived for nearby star clusters in the *LEGUS* galaxies (Brown and Gnedin, 2021). As for the cluster PSF profiles, the WFC3-UVIS PSFs[6] were convolved with either a *MOFFAT15*, a *MOFFAT25* or a *GAUSS* profile (see Appendix C). Then, using DOLPHOT's aperture photometry mode, the correction was calculated for each source as the difference of its magnitude in a 20 pixels aperture and its magnitude in an aperture with the same radius as the one used for PSF fitting photometry (3 pixels). In every case we found the average correction to be negligible (within the same order

[6]A PSF near the center of the detector was chosen for each filter since we are trying to calculate the correction only in the case of un-distorted clusters

of magnitude as the errors of the PSF fitting photometry). Therefore, even the largest clusters are not expected to deviate significantly from a point source. Additional tests of the appropriateness of the PSF fitting technique for star-clusters in NGC2276 are: the inspection of the residual images which shows how many sources were over or under subtracted, and the χ^2 of each fit (see definition in Appendix C), which serves as an indication of poorly fitted sources. Another way to get an idea whether most of our clusters truly are point-like, is to calculate the number of WFC3-UVIS pixels corresponding to clusters of different sizes at the distance of NGC2276. The mean effective radius of star clusters in the *LEGUS* galaxies is 3 pc and the maximum is 10 pc. This mean corresponds to only ~ 0.4 pixels and the maximum to ~ 1.3 pixels. Comparing that to the FWHM of the detector's point source PSFs (see table 1), we expect those clusters to be unresolved in every filter. For these reasons, we opted to not use aperture corrections.

The initial source catalogue contains 141,323 sources. The output magnitudes as well as their errors, are all in the *VEGAMAG* system[7]. Even though the DOLPHOT detection and photometry parameters were selected after extensive testing, the output catalogue will still contain a large number of unreliable sources. Those will be removed later in the analysis by imposing additional criteria, as discussed in the following section.

2.3 Catalogue Cleaning and Example Sources

The initial output photometry is expected to contain many poorly fitted sources with unreliable photometry, background fluctuations incorrectly identified as sources, as well as artifacts such as background galaxies detected as faint sources, diffraction spikes, or foreground stars. For that reason several constraints were applied in order to only include trustworthy sources. For each filter except F275W we only selected sources with SNR > 5. As for F275W a more relaxed constraint of SNR > 3 was selected given the higher noise of these data. Also, the PSF fit χ^2 was selected to be in the range $0.4 < \chi^2 < 3$. The lower limit was selected to avoid overfitted sources while the upper limit cuts poorly fitted sources such as very extended sources. Dolphin, 2000 also suggests a $\chi^2 < 3$ but also mentions it can be relaxed to $\chi^2 < 4$ for crowded fields. Another criterion is a cut on the magnitude uncertainty at mag error < 0.5. This ensures that the sources have small photometric errors, leading to meaningful colors. It is important to note that all of the above criteria were imposed in all filters simultaneously. Even if a source had good photometry in every filter except one, it was excluded from the cleaned catalogue. Especially in the case of Spectral Energy Distribution (SED) fitting (discussed in Section 3.5), high quality photometry is required for every filter in order to obtain accurate results. This cleaning, results to a catalogue containing 7,682 sources. By investigating the residuals we see that most removed sources are attributed to bad photometry in the F275W filter. Specifically, in that filter, many of the sources show significant residuals, suggesting poor PSF fitting. Some of them even have a negative SNR, meaning their photometry in F275W is invalid. This is also the case for some sources on the F336W filter but their number is much smaller. Applying the above criteria will eliminate those sources from the final catalogue, even though the photometry on other filters is usually fine. Finally, their χ^2 is usually higher, meaning they are not fit well. On the other hand, the residuals on the region suffering from the dragon's breath show well removed sources with good χ^2 and SNR in most filters (including F814W), while most of the bad-pixels have been masked out. No false sources attributed to dragon's breath seem to have been

[7]In the *VEGAMAG* magnitude system, the magnitude of Vega is by definition zero in every filter which means that the magnitudes are defined as $m = -2.5 \times \log \frac{f_{Source}}{f_{Vega}}$ where f_{Source} is the source's flux and f_{Vega} is the flux of Vega in the corresponding filter.

included in the uncleaned catalogue.

In an attempt to investigate variations of the star-cluster populations between different regions of the galaxy, the clusters were separated into four regions, each representing the west inner spiral, west outer spiral, center and east side of the galaxy (see fig. 8). Table 2 presents a portion of the source catalogue. Those sources were selected to have reliable photometry and be representative of various sub-galactic regions as can be seen in fig. 9. The boundaries of these regions were chosen arbitrarily but in a way that follows the structure of the galaxy. Postage-stamp images of those clusters are shown in fig. 10.

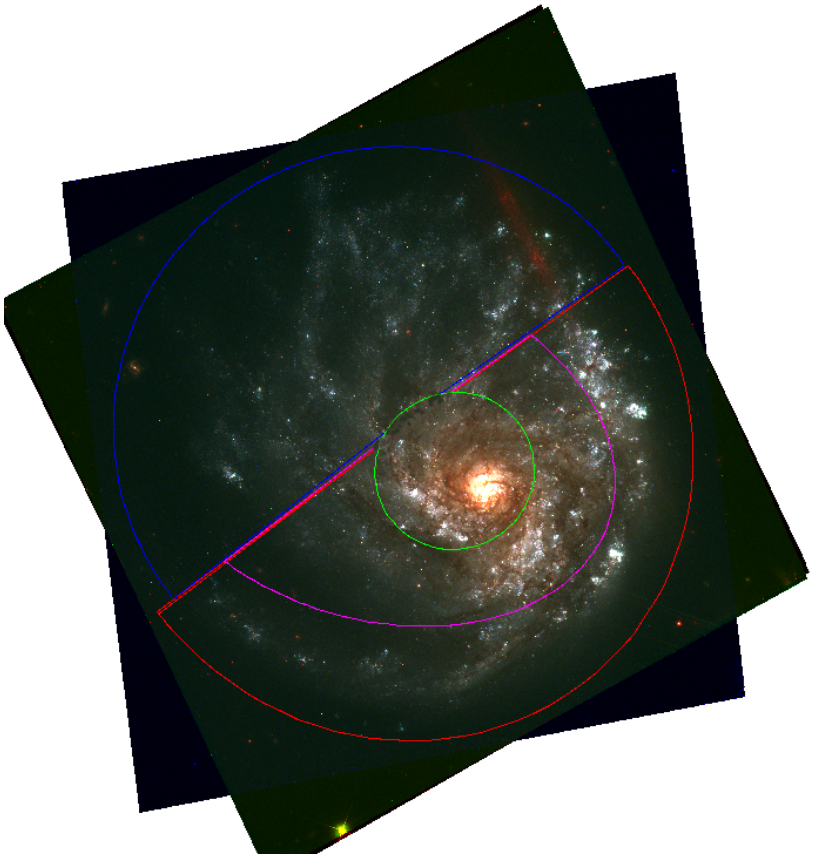

Figure 8: The different sub-galactic regions that were considered in the analysis. Hereinafter they will be called center region (green region), west-inner spiral (magenta), west-outer spiral (red) and east region (blue).

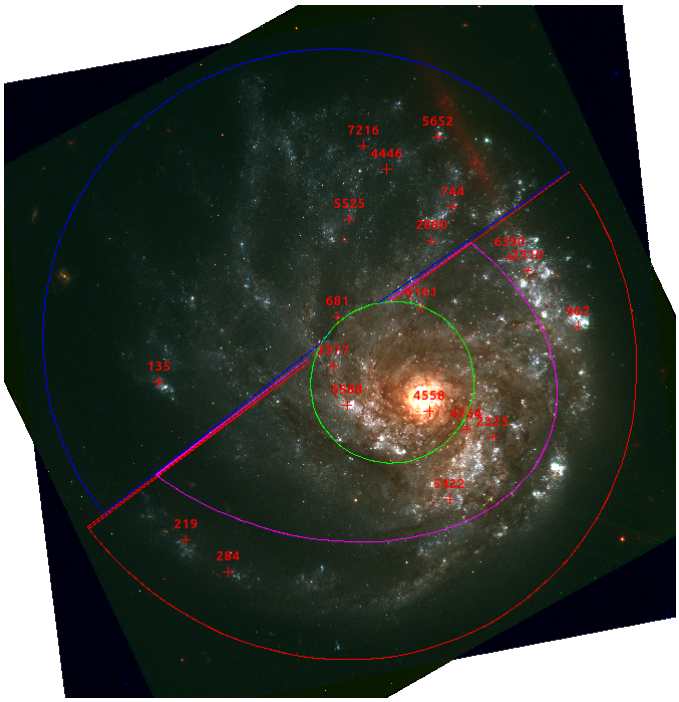

Figure 9: The selection of 20 random clusters from the cleaned catalogue (red crosses). The number above them is their ID in table 2.

ID	RA (J2000) (h:mm:ss)	DEC (J2000) (dd:mm:ss)	mag(F275W) $\pm\Delta$mag	mag(F336W) $\pm\Delta$mag	mag(F438W) $\pm\Delta$mag	mag(F555W) $\pm\Delta$mag	mag(F814W) $\pm\Delta$mag
4558	7:27:12.63	85:45:13.87	25.433 ± 0.224	25.420 ± 0.147	26.099 ± 0.095	25.646 ± 0.056	25.109 ± 0.092
4764	7:27:4.05	85:45:9.26	25.353 ± 0.244	25.152 ± 0.105	26.067 ± 0.083	25.766 ± 0.047	25.372 ± 0.092
6161	7:27:14.31	85:45:40.41	24.995 ± 0.168	25.235 ± 0.106	26.552 ± 0.108	26.054 ± 0.060	25.717 ± 0.125
135	7:28:15.17	85:45:21.22	23.245 ± 0.079	23.141 ± 0.028	24.092 ± 0.030	23.856 ± 0.012	23.099 ± 0.015
962	7:26:38.26	85:45:35.54	23.434 ± 0.061	23.339 ± 0.034	24.659 ± 0.032	24.605 ± 0.022	24.615 ± 0.056
681	7:27:33.80	85:45:38.05	23.318 ± 0.054	23.276 ± 0.031	24.451 ± 0.030	24.380 ± 0.017	24.428 ± 0.037
2880	7:27:11.93	85:45:57.57	24.198 ± 0.094	24.232 ± 0.060	25.561 ± 0.057	25.336 ± 0.038	25.397 ± 0.079
744	7:27:7.17	85:46:6.12	23.317 ± 0.054	23.334 ± 0.034	24.597 ± 0.030	24.484 ± 0.019	24.053 ± 0.029
5652	7:27:10.55	85:46:24.16	24.236 ± 0.107	24.824 ± 0.098	26.124 ± 0.095	26.058 ± 0.059	26.196 ± 0.157
284	7:27:59.04	85:44:32.64	25.163 ± 0.175	24.172 ± 0.048	24.857 ± 0.030	23.997 ± 0.012	23.416 ± 0.018
2510	7:26:49.76	85:45:49.81	24.410 ± 0.123	24.168 ± 0.065	25.364 ± 0.057	25.200 ± 0.034	25.270 ± 0.086
2325	7:26:57.89	85:45:7.16	25.212 ± 0.232	24.879 ± 0.096	26.386 ± 0.105	25.914 ± 0.055	23.968 ± 0.031
5525	7:27:31.06	85:46:3.15	25.321 ± 0.218	25.821 ± 0.168	26.298 ± 0.085	26.043 ± 0.047	25.753 ± 0.088
6390	7:26:53.99	85:45:53.33	25.667 ± 0.282	25.192 ± 0.106	26.168 ± 0.083	26.264 ± 0.087	25.728 ± 0.102
6588	7:27:31.56	85:45:15.59	25.188 ± 0.246	25.603 ± 0.194	26.777 ± 0.176	26.188 ± 0.078	26.240 ± 0.215
219	7:28:8.82	85:44:40.85	24.929 ± 0.147	23.519 ± 0.032	23.991 ± 0.019	23.907 ± 0.012	23.540 ± 0.019
2377	7:27:34.74	85:45:25.58	25.459 ± 0.226	25.453 ± 0.123	26.009 ± 0.071	25.349 ± 0.032	24.229 ± 0.037
4446	7:27:22.38	85:46:15.88	25.625 ± 0.248	25.778 ± 0.148	26.091 ± 0.069	25.746 ± 0.037	25.458 ± 0.066
5422	7:27:8.017	85:44:51.35	24.756 ± 0.143	25.056 ± 0.104	25.950 ± 0.077	25.916 ± 0.053	26.083 ± 0.158
7216	7:27:27.78	85:46:21.93	25.938 ± 0.340	25.107 ± 0.093	26.707 ± 0.117	26.742 ± 0.074	26.728 ± 0.181

Table 2: Coordinates and photometry of 20 random sources from the cleaned catalogue (in the Vega system).

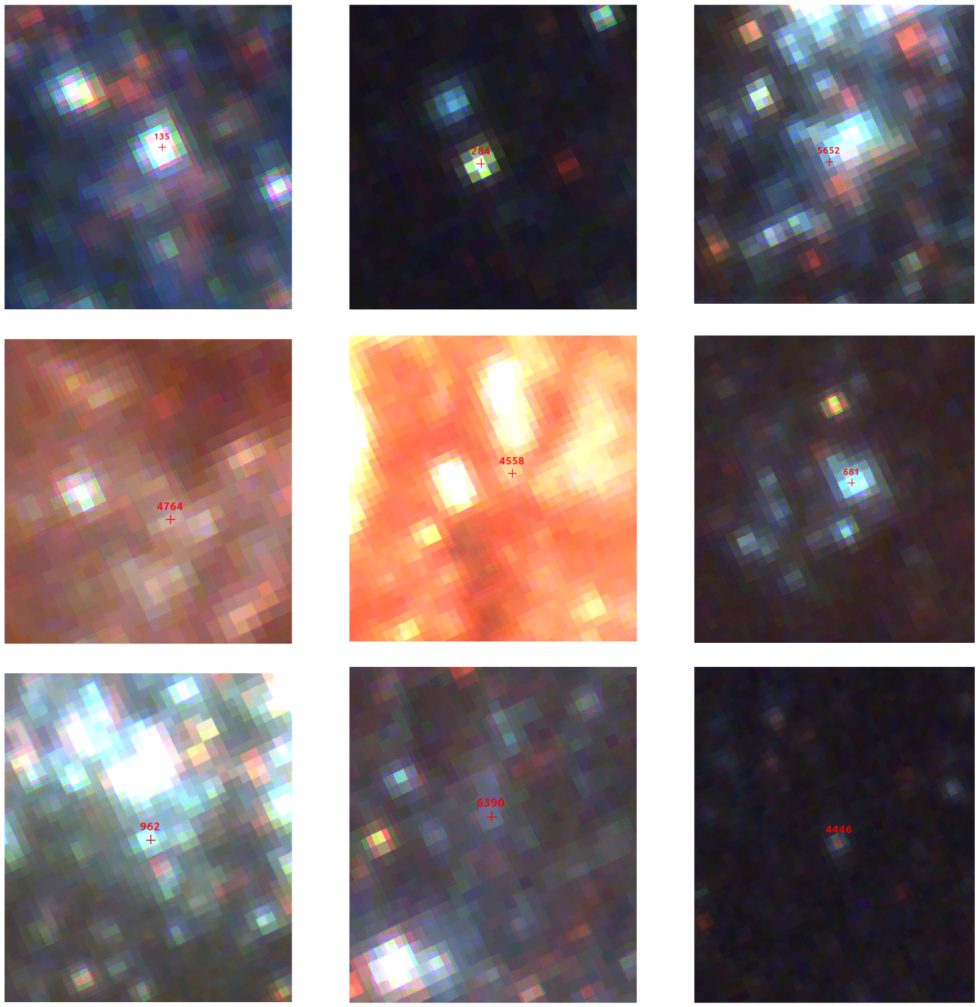

Figure 10: Some of the random clusters used in this section (red crosses). The number above corresponds to their ID in table 2.

3 Star Cluster Properties

3.1 Stellar Population Synthesis

A very useful tool for studying the properties of star-clusters is stellar population synthesis (SPS) models (a review of SPS can be found at Conroy, 2013). The composite spectrum of a stellar population is affected by its age, its metallicity (and metallicity abundance pattern[8]), its dust content (the grain size, distribution and density) and nebular emission, the star formation history (SFH), the initial mass function (IMF)[9] and the total mass.

Since in this investigation we want to create stellar populations that represent star-clusters, we assume that all stars were created simultaneously (that is called a simple stellar population; SSP). In this context, we can obtain the SSP's spectrum by adding all the individual stellar spectra. Stellar spectra depend on the star's effective temperature, which is a function of its mass ($T_{eff}(M)$), and its metallicity abundance pattern, for a given star of age t and metallicity Z. If $\Phi(M)$ is the IMF, then the composite spectrum is:

$$f_{SSP}(t, Z) = \int_{m_0}^{m_{up}(t)} f_{star}[T_{eff}(M)|\, t, Z]\, \Phi(M) dM \tag{1}$$

The lower limit of integration is usually chosen to be the minimum mass required to reach temperatures where hydrogen undergoes nuclear fusion (usually 0.08 or 0.1 $M_{\odot}$). The upper limit depends on the choice of a stellar evolution model. To this SSP spectrum we also include the dust spectrum and the nebular emission spectrum, as discussed below[10]. A useful graph that shows how each of these components contributes to the composite spectrum can be seen in fig. 11. Notice that in the case of a SSP, the star formation rate (SFR) would be a delta function. The code we use for the stellar population synthesis is FSPS (Flexible Stellar Population Synthesis) (Conroy and Gunn, 2010a; Conroy and Gunn, 2010b).

Stellar evolution models for SSPs come in the form of isochrones, curves that describe the position on the Hertzsprung-Russel (HR) diagram of each star of the population, given the age of the population. The relationship between temperature, metallicity abundance pattern and mass (for a given age and metallicity) is also encoded in the isochrones. The choice of isochrone will affect the SPS and between the many available isochrone models, there is no correct choice. Some of them are more focused in different areas of stellar evolution than others. The first set of isochrones used in this investigation are the MIST (MESA Isochrones and Stellar Tracks) isochrones (Dotter, 2016; Choi et al., 2016). This is currently the most modular and sophisticated model and for that reason it is preferred over other popular isochrone models, such as the PADOVA (Bertelli et al., 1994; Girardi et al., 2000, Marigo et al., 2008) or GENEVA (Schaller et al., 1992; Meynet and Maeder, 2000) isochrones. The other set of isochrones used here are the BPASS (Binary Population And Spectral Synthesis) isochrones (Eldridge et al., 2007; Eldridge and Stanway, 2009, Stanway and Eldridge, 2018), which incorporate binary evolution. Modelling binaries is extremely important in the evolution of a population since most stars are formed in binary systems and mass transfer in the binary affects the evolution and the atmosphere of the stars.

[8] Abundance pattern refers to each element's contribution to the total chemical composition of the star.

[9] The IMF is the initial mass distribution of stars born simultaneously.

[10] One can also assume a time-dependent metallicity for the population as well as a time-dependent SFH. In that case we say we have a Composite Stellar Population (CSP).

The (individual) stellar spectra depend on all the aforementioned physical parameters and are provided in the form of stellar spectral libraries. In this study, the MILES library (Sanchez-Blazquez et al., 2006) was used. This is an empirical spectral library, meaning it was derived from observations. Once again, there is no correct answer when having to choose between empirical and theoretical spectral libraries. Theoretical libraries are limited by the incompleteness and inaccuracy (due to lack of knowledge) of the theoretical models, while empirical libraries suffer from observational constraints. An important problem empirical libraries face is the assignment of physical parameters to stars as well as the interpolation when a parameter value falls between values of the library's parameter grid.

Regarding the IMF, its form affects the mass-to-light (M/L) ratio of the population, the rate of luminosity evolution for evolving populations and the shape of the population's spectral energy distribution (SED; discussed in Section 3.5). The IMF we chose was the Kroupa IMF (Kroupa, 2001). This IMF has the form of a broken power-law and is perharps the most widely used IMF for star-clusters nowadays. In FSPS, the output population's mass is normalized to $1M_{\odot}$.

As for metallicity, we adopt the value of $Z = 0.22Z_{\odot}$ as reference (as reported in Wolter et al., 2015), but we also compare it with other values to investigate its effect. Higher metallicity leads to redder spectra in two ways: first, higher metallicity means lower effective temperatures which in turn means redder colors. Also, even if we assume two populations comprised of stars with the same effective temperatures, increasing the metallicity leads to stronger absorption which of course means that we also get redder colors. The metallicity abundance pattern affects the resulting spectrum since it quantifies the chemical composition. Later, when trying to do SED fitting to derive cluster parameters, we are forced to assume a constant value of metallicity for the clusters, since there is no way to distinguish whether the red color comes from higher metallicity or age, based on the limited amount of data we have available.

When it comes to the composition of dust, usually small sized dust grains are associated with polycyclic aromatic hydrocarbons (PAHs) while larger ones are associated with graphite (Shivaei et al., 2022). Silicate grains are also present. As can be seen in fig. 11, dust contributes to both absorption and emission. Regarding absorption, dust grains absorb photons or scatter them, reducing the radiation's intensity along the line of sight (dust extinction). Absorption depends on the wavelength of photons and the dust's chemical composition. When taking into account the fact that light can also be scattered towards the line of sight as well as the geometrical distribution of the dust, we refer to the effect this has on the observed intensity as attenuation. In this study we create populations of zero extinction but we also compare them with populations with a reference extinction of one magnitude in the V band ($A_V = 1$). The first model we consider is the Cardelli attenuation law (Cardelli et al., 1989), which was derived using Milky Way observations. The second one we use is the Calzetti attenuation law (Calzetti et al., 2000). Notice that the Calzetti attenuation law is derived from starburst galaxies and is therefore, theoretically, more fit to describe the populations in NGC2276. These attenuation laws are discussed in more detail in Appendix A. Again, it is not easy to distinguish whether reddening in a population is the result of dust or aged stars, but since dust affects significantly the colors (in contrast to metallicity which does not have a great effect on the colors; see Section 3.4), it is possible to use it as a free parameter during the SED fitting (see Section 3.5).

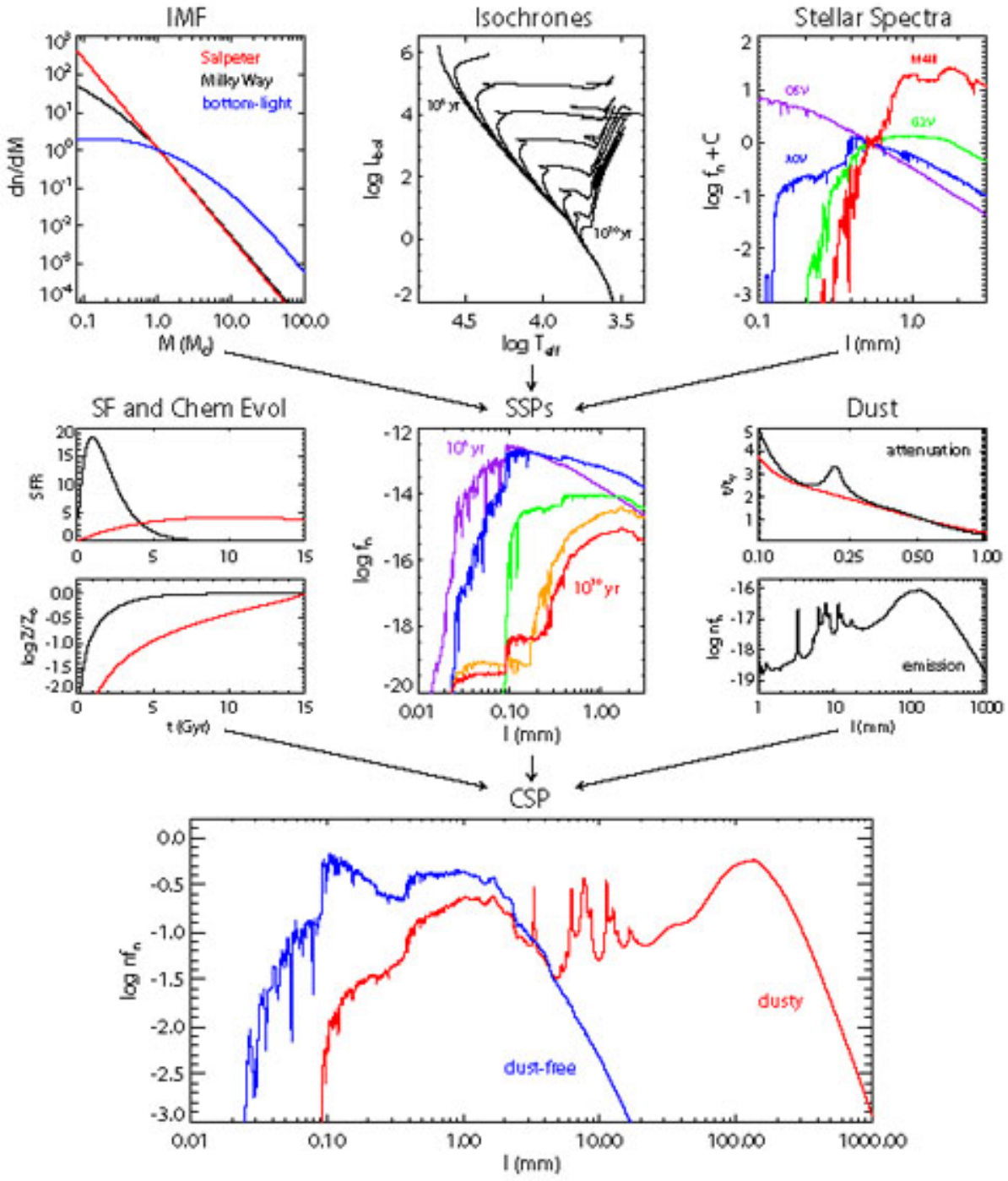

Figure 11: The recipe for SPS. A SSP is comprised of stellar spectra by stars of the same age but different evolutionary stages. This information is encoded in the isochrone, together with the IMF, which informs us of how the initial masses were distributed and therefore how many stars are in each evolutionary stage. Then we only need to add the effect of dust (attenuation and nebular emission) to get the composite spectrum. In the general case we also take into account the SFH and the chemical evolution, but for star clusters we consider both of those a delta function. Credit: Conroy, 2013

Star light heats up the dust which then re-emits photons in the IR and FIR therefore contributing to the observed spectrum (it dominates the emission spectrum for wavelengths $\geq 10\mu m$). This dust emission depends on the strength of the interstellar radiation field, the size distributions of the grains as well as their chemical composition. The PAH emission lines are located at $3.3\mu m$, $6.2\mu m$, $7.7\mu m$, $8.6\mu m$ and $11.3\mu m$. In fact, wavelengths $\leq 12\mu m$ are dominated by PAH emission (this emission amounts to about 1/3 of the total emission). The long wavelengths emission ($\lambda \geq 50\mu m$) amounts to about 2/3 of the total observed emission and comes from constant temperature dust grains (at $\sim 10 - 20$ K). Regarding the dust spectra, the DL07 library (Draine and Li, 2007) was used, which is the default library used in FSPS. This library includes theoretically calculated dust emission spectra assuming a mixture of different size silicate and carbon grains as well as different concentrations of PAHs[11].

An integral part of a young star-cluster are nebulae whose ionized gas contributes to both continuum emission through free-free, free-bound and two photon emission, and line emission via electron recombination. FSPS implements its own nebular emission model (Byler et al., 2017) which utilizes the CLOUDY photoinization code (Ferland et al., 2013). CLOUDY calculates photoinization by accounting for all the radiative transfer effects that take place when light travels through a gas cloud. Since nebular emission plays a major role especially in young populations of low metallicites, we expect it to be rather important in the case of NGC2276. In order to be self-consistent, we set the gas metallicity equal to the population's metallicity[12]. To quantify the degree of ionization in the gas we use the fraction of the gas ionization flux to the gas density, which for that reason is known as the gas ionization parameter[13]. We set that to: log(gas ionization) $= -2$, which is the default value suggested by FSPS. We also tried to exclude nebular emission but the data were in disagreement with these models.

In the context of this investigation, populations are synthesized for different ages and then, for each filter used, the resulting spectrum is convolved with the filter's transmission curve (fig. 5). That way we obtain a theoretical estimation of the intensity in each spectral band for a stellar population of a given age and other parameters such as metallicity, dust content etc. We can then create diagnostic plots (e.g. color-color or color-magnitude diagrams) and compare the observational data with a theoretically calculated evolutionary track (the path of the integrated emission of a stellar population on a color-color or color-magnitude diagram as it ages). Even though these diagrams are not able to provide exact values for these parameters, they serve as a qualitative tool to explore trends in the cluster populations. To obtain values for these parameters for each cluster, a SED fitting algorithm must be used (discussed in Section 3.5).

SPS is a wide subject covering many topics from nuclear reactions and radiative transfer to dust geometry models and astro-chemistry. For a detailed description see Conroy, 2013 and references within. Also, most of these models are a simplified one-dimensional version and omit effects that necessary require a three-dimensional space to be studied[14]. For these reasons, we do not expect the theoretical models to follow our data very closely and this is something that cannot be avoided since each model and each parameter choice gives a different, but not necessarily wrong, answer. At

[11] An assumption of the model is that there are no aggregations of grains. This is consistent with observations but not a confirmed feature.

[12] That is controlled via the *gas_logz* FSPS parameter.

[13] This is set via FSPS's *gas_logu* parameter.

[14] Such effects include convection, rotation and mass loss.

the very least the synthetic populations can provide a qualitative estimate of the observed cluster parameters. These subjects are studied in greater detail in Sections 3.2 and 3.3.

3.2 Star-Cluster Ages Based on Color-Color and Q-Q Diagrams

In order to obtain an idea of the clusters' ages, we will utilize the so called Color-Color diagrams and Q-Q diagrams. Color is defined as the difference in magnitude between two filters. For instance, for the B and V filters:

$$B - V \equiv \mathrm{mag}(B) - \mathrm{mag}(V) \tag{2}$$

This reflects the temperature (and hence the mass) of the stars. Since the mass distribution of a stellar population is a strong function of its age, the color is a function of the population's age (for a given metallicity and extinction).

If we plot a color against another color we have a Color-Color (C-C) diagram. Comparing the observed distribution of clusters on a C-C diagram with evolutionary tracks calculated from theoretical SPS models we can infer the ages of the star-clusters.

Instead of color we can also calculate a quality which is known as the reddening-free parameter or just the Q parameter defined as:

$$Q_{m_1,\,m_2,\,m_3,\,m_4} \equiv (m_1 - m_2) - \frac{E(m_1 - m_2)}{E(m_3 - m_4)}(m_3 - m_4) \tag{3}$$

Where m_1, m_2, m_3, m_4 are the magnitudes in four different bands, and:

$$E(m_1 - m_2) = A(m_1) - A(m_2) \tag{4}$$

is the color excess between bands 1 and 2. These depend on our choice of attenuation model. Their values for the filters used in this study are shown in table 3. A_m is the magnitude of the absorption on filter m. We can also define Q parameters using only three bands. For instance:

$$Q_{m_1,m_2,m_3} = (m_1 - m_2) - \frac{E(m_1 - m_2)}{E(m_2 - m_3)}(m_2 - m_3)$$

These parameters are similar to color but do not depend on the reddening of each source (they only depend on the choice of the attenuation model). For more details on the Q parameters see Appendix B. Plotting two Q parameters calculated from different sets of filters against each other constitutes what is known as a Q-Q diagram. They are used in the exact same way as C-C diagrams but are useful since they eliminate intrinsic dust reddening.

Based on the cleaned catalogue (Section 2.3) we create C-C and Q-Q diagrams for different combinations of filters, shown in figs. 12, 13, 14 and figs. 15, 16, 17 respectively. In these plots we separate the sources depending on their location on the galaxy (Section 2.3; fig. 8): 2175 sources in the east, 1245 in the center region, 2136 in the west inner spiral and 2126 in the west outer spiral. This way we can investigate possible trends in the star-cluster ages in a sub-galactic scale. In these diagrams, we chose to merge the west (inner and outer) spiral with the central region (red points on the plots), since they did not differ substantially in color. The east region is considered independently (blue points). On the sides of each diagram we also show histograms of the clusters

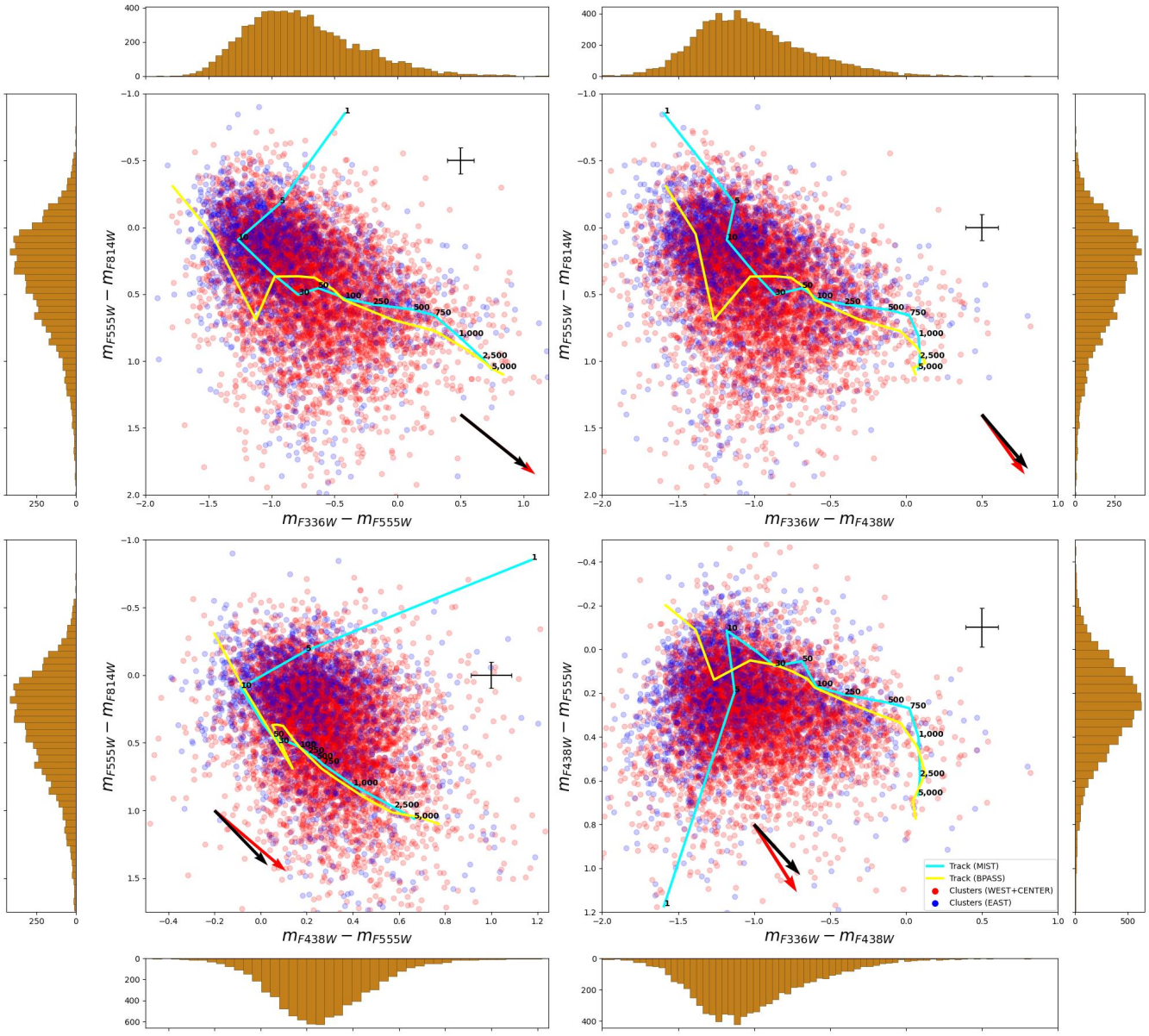

Figure 12: Color-Color diagrams for the cleaned catalogue sources. The points are color coded according to the region in which each cluster belongs to (regions are shown in fig. 8). The west inner and outer spiral regions have been combined with the central region (red points) while the east region clusters remained separate (blue points). The point with the error bars denotes the average photometry error (calculated using error propagation). The solid lines correspond to the evolutionary tracks (MIST tracks are the cyan lines and BPASS tracks are the yellow lines). The number above the MIST tracks denotes the age of that point in Myrs. The same ages hold for the BPASS tracks points following the same direction as in the MIST tracks. The vectors show how the tracks would move with an extinction of $A_V = 1$ mag (extinction vectors). The black extinction vector was calculated using the Calzetti attenuation law and the red using the Cardelli attenuation law (see Appendix A). The histograms located at the edges of each diagram depict the distribution of the corresponding color. The data are in general agreement with the tracks, considering that the dust content is non-zero and therefore the tracks will move along the length of the extinction vectors.

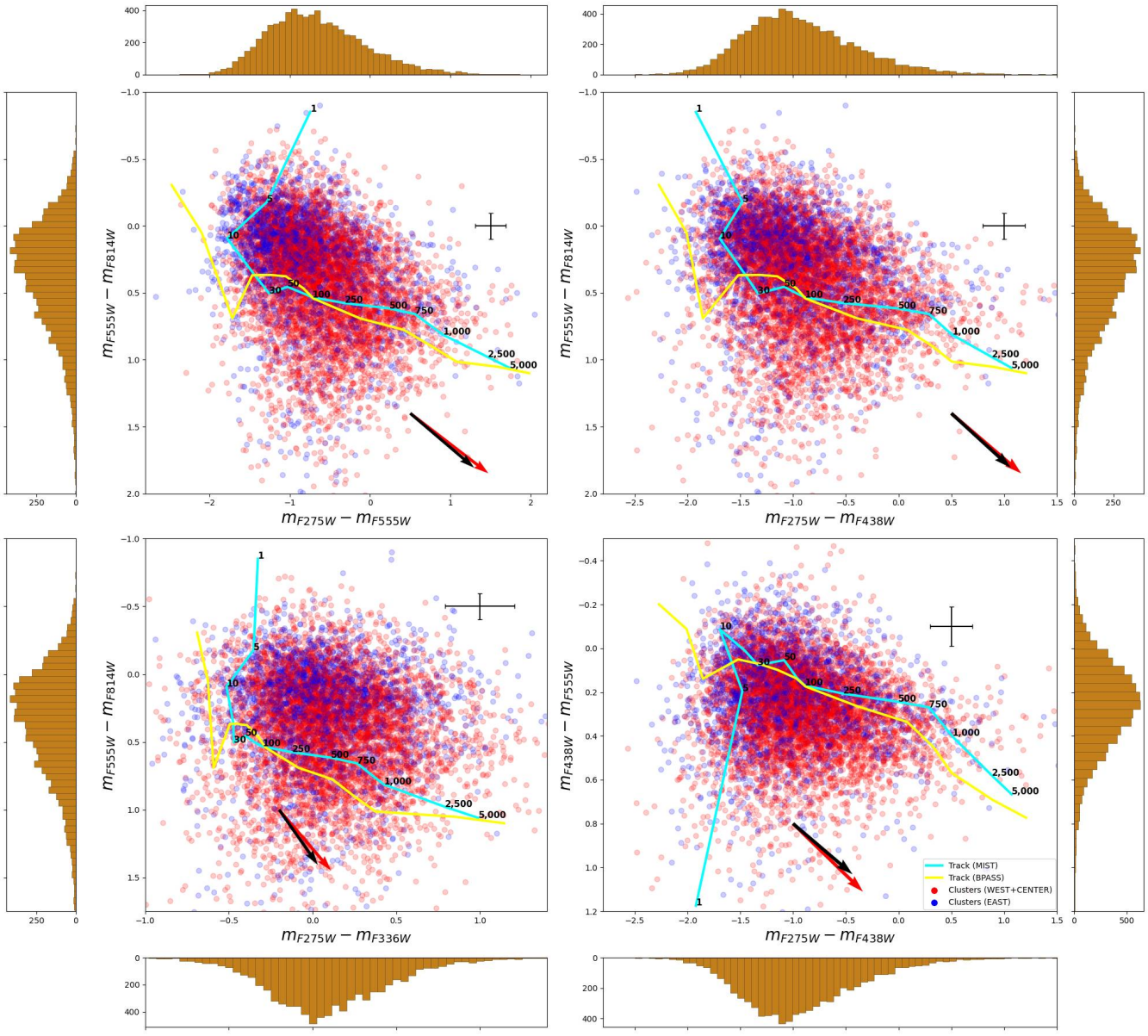

Figure 13: Color-Color diagrams for the cleaned catalogue sources. See fig. 12 for a more thorough description. The data are in general agreement with the tracks, considering that the dust content is non-zero and therefore the tracks will move along the length of the extinction vectors.

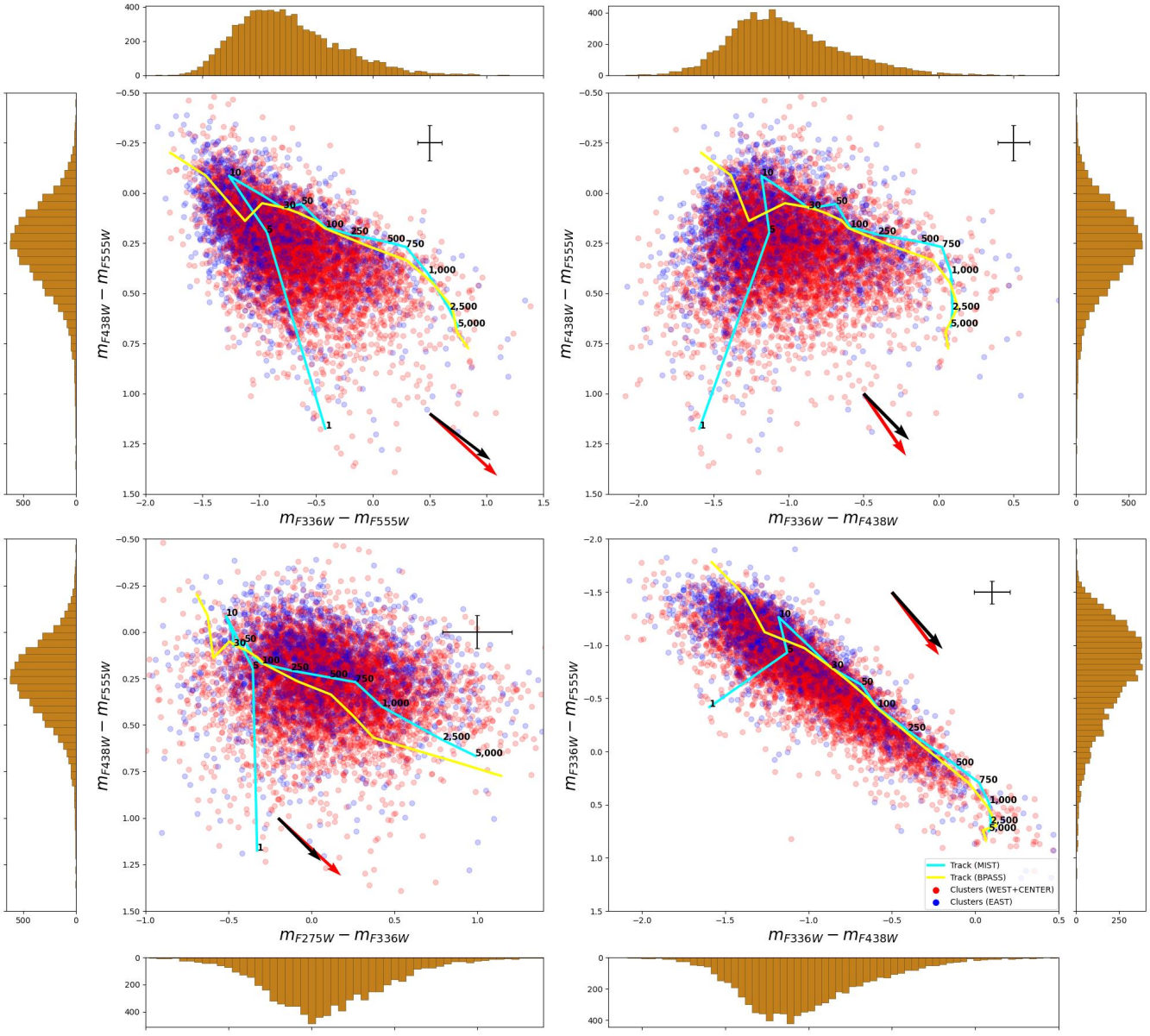

Figure 14: Color-Color diagrams for the cleaned catalogue sources. See fig. 12 for a more thorough description. The data are in general agreement with the tracks, considering that the dust content is non-zero and therefore the tracks will move along the length of the extinction vectors.

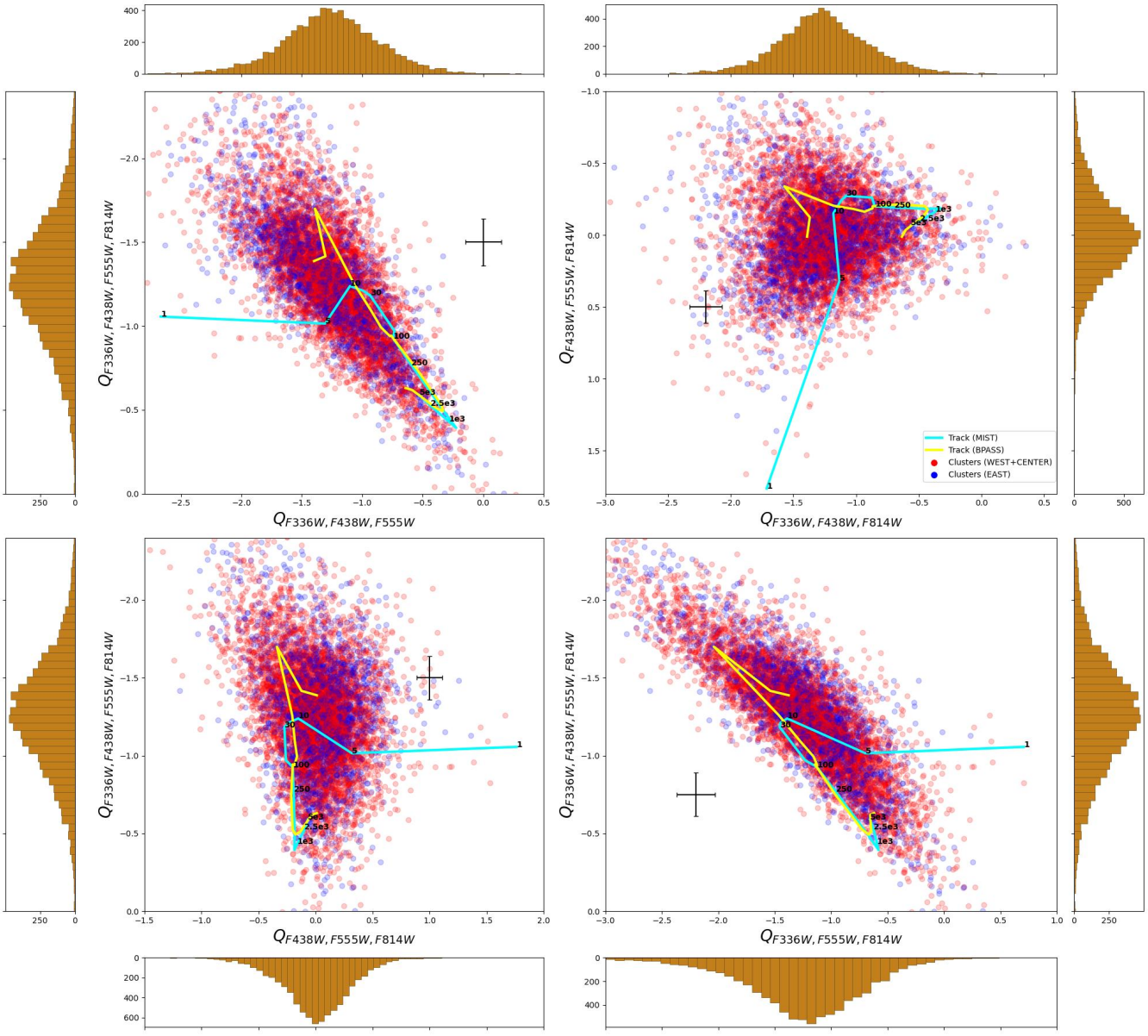

Figure 15: Q-Q diagrams created using the cleaned catalogue sources and the Cardelli attenuation law as described in Section 3.2 and Appendix A. Their structure is the same as described in fig. 12. Notice that the data towards the top of the diagram can not be explained by the tracks created assuming the MIST isochrones. The tracks do not seem to cover the full spread of the data. This is explained by the variation in metallicity, as discussed in Section 3.4.

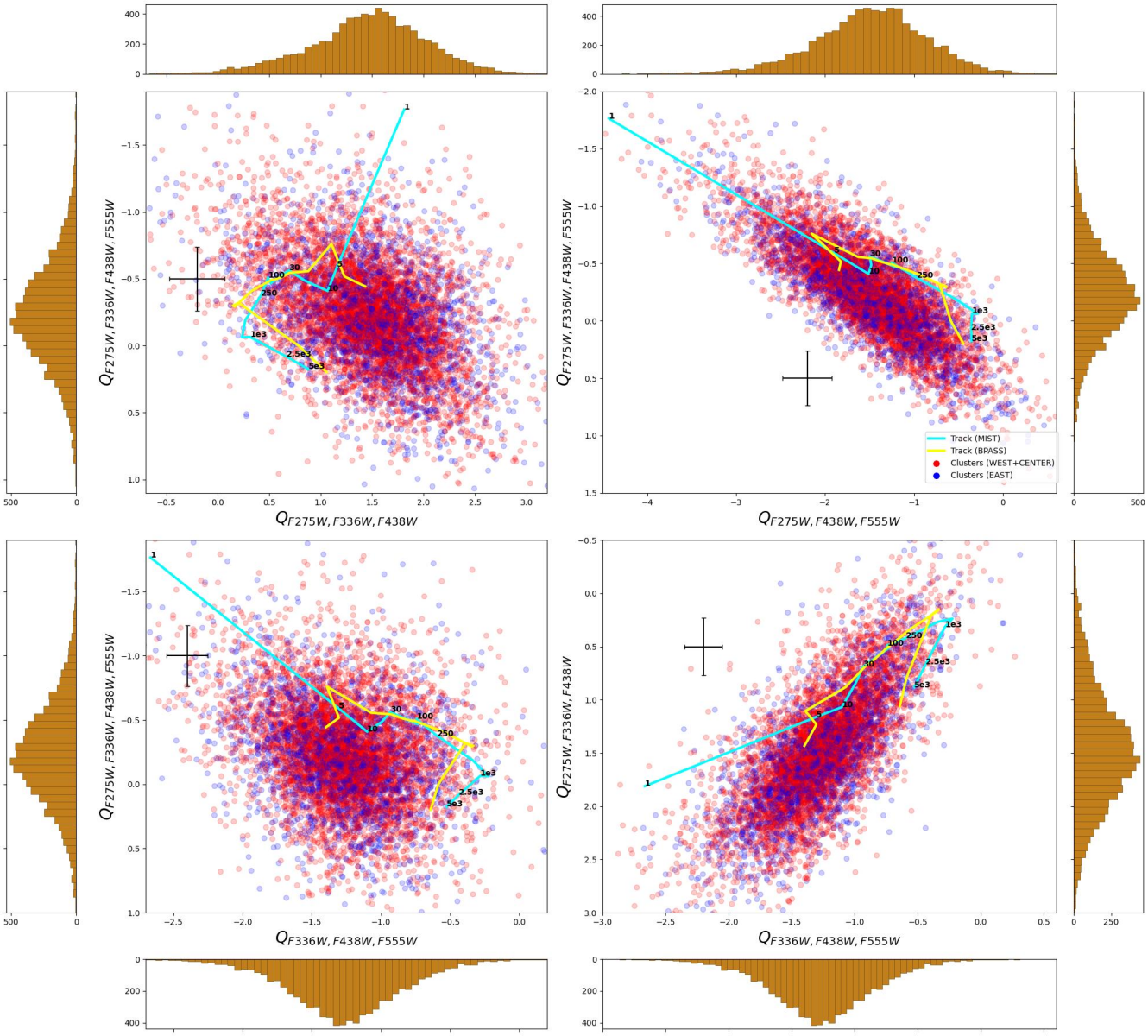

Figure 16: Q-Q diagrams created using the cleaned catalogue sources and the Cardelli attenuation law, following the structure of fig. 12. Notice that for these diagrams, contrary to fig. 15, the distribution of the data does not agree with the evolutionary tracks, which trace only a small part of the data. That disagreement could be explained to some degree by poor F275W photometry (which was used instead of F336W, in contrast to fig. 15). Another possible explanation is the variation in metallicity, which however, is not the case, as discussed in Section 3.4.

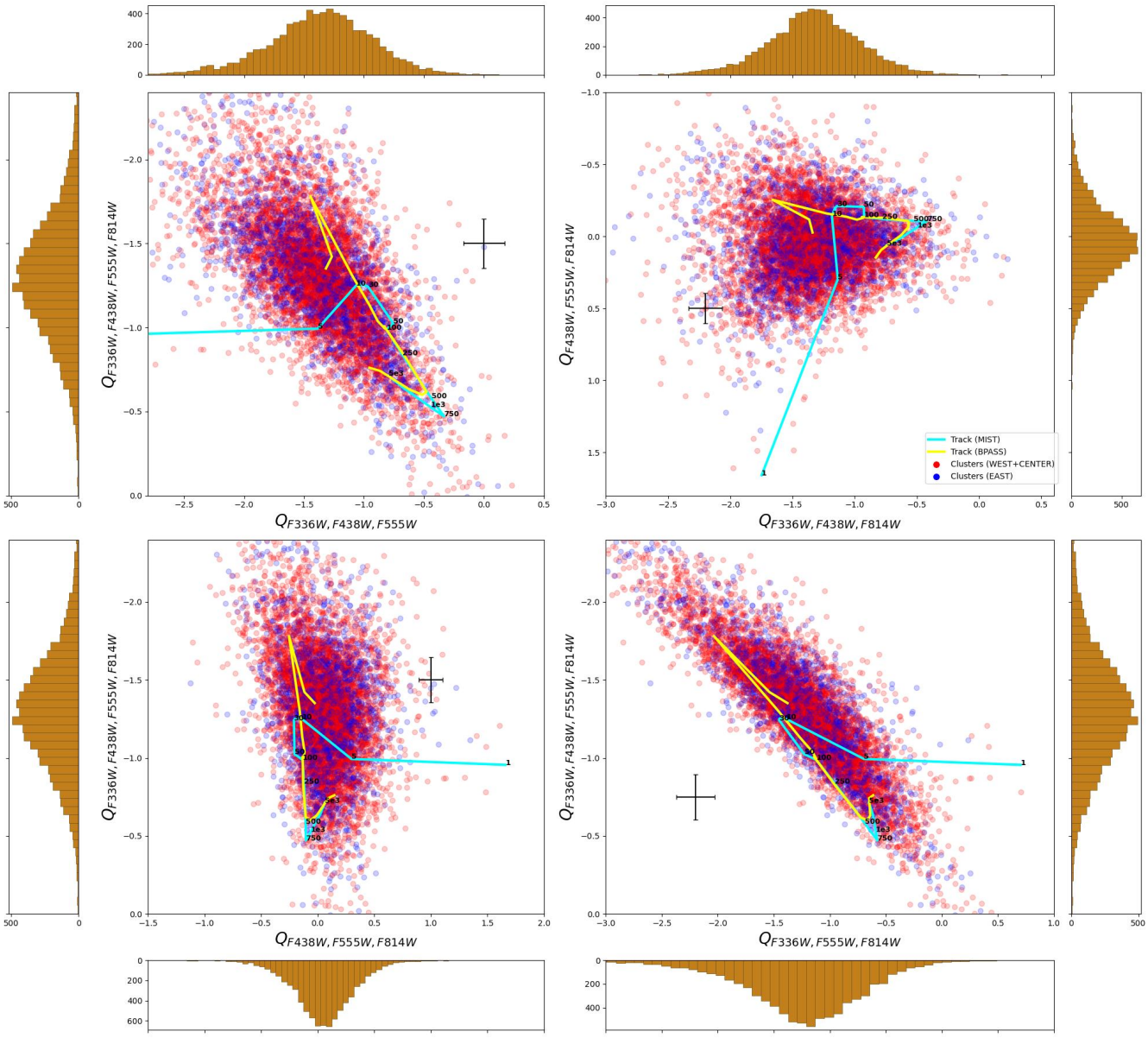

Figure 17: Q-Q diagrams created using the cleaned catalogue sources and the Calzetti attenuation law. Their structure is the same as described in fig. 12. The diagrams seem slightly more compact in comparison to the ones calculated using the Cardelli attenuation law (figs. 15 and 16) though they do not make a great difference and we cannot infer something regarding how well each attenuation law describes our data.

Color Excess	Cardelli ($R_V = 3.1$)	Calzetti ($R_V = 4.05$)
$E(F275W - F336W)$	0.38	0.26
$E(F275W - F438W)$	0.66	0.56
$E(F275W - F555W)$	0.97	0.80
$E(F275W - F814W)$	1.42	1.20
$E(F336W - F438W)$	0.28	0.30
$E(F336W - F555W)$	0.59	0.54
$E(F336W - F814W)$	1.04	0.94
$E(F438W - F555W)$	0.31	0.23
$E(F438W - F814W)$	0.76	0.64
$E(F555W - F814W)$	0.45	0.41

Table 3: Color excess between the different pairs of filters used in our work. We consider the Cardelli attenuation law with $R_V = 3.1$ and the Calzetti attenuation law with $R_V = 4.05$. The R_V parameters are discussed in Appendix A.

color.

The two solid lines correspond to evolutionary tracks created using MIST (blue line) and BPASS (yellow line) isochrones, with no absorption and a metallicity $Z = 0.22Z_{\odot}$. The two vectors in each diagram show how the track would be offset if we had a 1 mag absorption in the visual band ($A_V = 1$; absorption vector). The red vector was calculated using the Cardelli attenuation law and the black one using the Calzetti attenuation law (see Appendix A).

In all of the C-C diagrams, we can see that the data seem to be well explained by the evolutionary tracks, if a range of extinction values is considered. With that in mind we also observe that most clusters seem to be young, concentrated around ages of 5-10 Myr. This is consistent for both the MIST and BPASS tracks. Additionally, there appears to be a lack of clusters with ages ≥ 75 Myr. This order of magnitude is in agreement with the simulations of Wolter et al., 2015 who argue (based on their model of the NGC2276 interaction with the NGC2300 group) that most of the clusters were created ~ 85 Myr ago. When considering the BPASS tracks and an extinction of $A_V = 1$ mag, the center of the color-color distribution is located near the 1 Myr point. In general, offsets between the zero-extinction tracks and the data in the C-C diagrams can be explained if we consider an absorption of $A_V \sim 0.5$ mag (that would bring the tracks near the center of the distribution if we move them along the extinction vectors).

Regarding the sub-galactic effects, with a first look it seems that the east region clusters seem to be more concentrated towards the upper left side of the diagrams. This means that they appear bluer than the clusters located on either the center or the west spiral. Although this could be a result of poorer sampling of the distribution by the eastern clusters (2175 vs 5507 clusters) it could also be due to extinction. The Q-Q diagrams will help to clarify that.

Since the Q parameters depend only on the choice of attenuation law, we show diagrams for the Cardelli attenuation law (figs. 15, 16) and the Calzetti attenuation law (fig. 17). If we compare fig. 15 with fig. 17 where the same Q-Q plots are shown for the two different attenuation laws, we observe that the Calzetti-calculated Q-Q diagrams are slightly more compact (less scatter). Since this difference is insignificant, both attenuation laws seem to describe our data equally well.

We can see that now both east region clusters and west/center region clusters are now distributed in the same way. That means that extinction does play an important role in the difference we observed in the distribution of clusters in the Color-Color diagrams and the imbalanced sample was not the only culprit. Then this would mean that there is a difference in the dust content between the east region and the other regions of the galaxy. In fact, clusters found in the central or western side should have a larger dust content since they appear redder on the C-C diagrams. That could support the claim that the west/center region clusters experienced recent starburst and therefore contain more young massive clusters, which are expected to have a larger dust concentration.

An interesting result only evident in the Q-Q diagrams is that now the structure of the data is inconsistent with the MIST tracks but in agreement with the BPASS tracks. This is an indication that effects of binary evolution are non-negligible. Also, the center of the distribution seems to be near the 1 Myr point on the BPASS tracks and near the 10 Myr point on the MIST tracks. One might argue that the disagreement between the data distribution and the MIST tracks can be explained when we consider different metallicities. This is to some degree correct, but as we discuss in Section 3.4, the BPASS tracks still seem necessary to explain the data.

3.3 Color-Magnitude Diagrams and Q-Magnitude Diagrams

Another very important kind of diagrams are the Color-Magnitude Diagrams (CMDs), which are plots of the absolute magnitude[15] on the y-axis and the color on the x-axis (see fig. 18). These diagrams encode important information regarding star cluster characteristics such as their age and mass. Of course, we can also use Q-Magnitude diagrams (QMDs) in the same manner (see fig. 19).

The total luminosity of a cluster depends on its stellar mass and its mass-to-light ratio, M/L. Therefore, the absolute magnitude will also depend on M/L. The evolutionary tracks are normalized to a total mass of $M = 1M_{\odot}$. For illustration purposes the cluster tracks overplotted on these diagrams are shifted arbitrarily on the y-axis. We assume a M/L ratio of 1 for this shift. Of course since this only shifts the y-axis, we apply the same on the Q-Magnitude diagrams. It is important to note that this does not provide an estimation for the cluster masses, since the value $M/L = 1$ was arbitrarily chosen, but it proves a sanity check for the cluster mass range. An accurate estimation of masses is obtained in Section 3.5.

If we imagine the tracks moving about halfway along the extinction vector (that would correspond to $A_V = 0.5$ mag), most clusters have total masses consistent with $\sim 5 \times 10^3\, M_{\odot}$. This is consistent with the average mass of large clusters detected in HST observations of similar galaxies (e.g. the *LEGUS* galaxies). In general, we can see that the BPASS tracks seem to closely follow the distribution of the data, contrary to the MIST tracks which generally tend to produce more luminous and bluer clusters.

The same results hold when we look at the QMDs. Though, it is interesting to notice that now some cluster populations can only be explained via the BPASS tracks (for instance the lower right diagram in fig. 19). To summarize, the cluster distribution seems to be centered near young clusters with masses between $5 \times 10^3\, M_{\odot}$ - $2 \times 10^4\, M_{\odot}$. There is also a large fraction of lower mass clusters

[15]The absolute magnitude of a source is defined as the magnitude the source would have if it was located at a distance of 10pc from Earth.

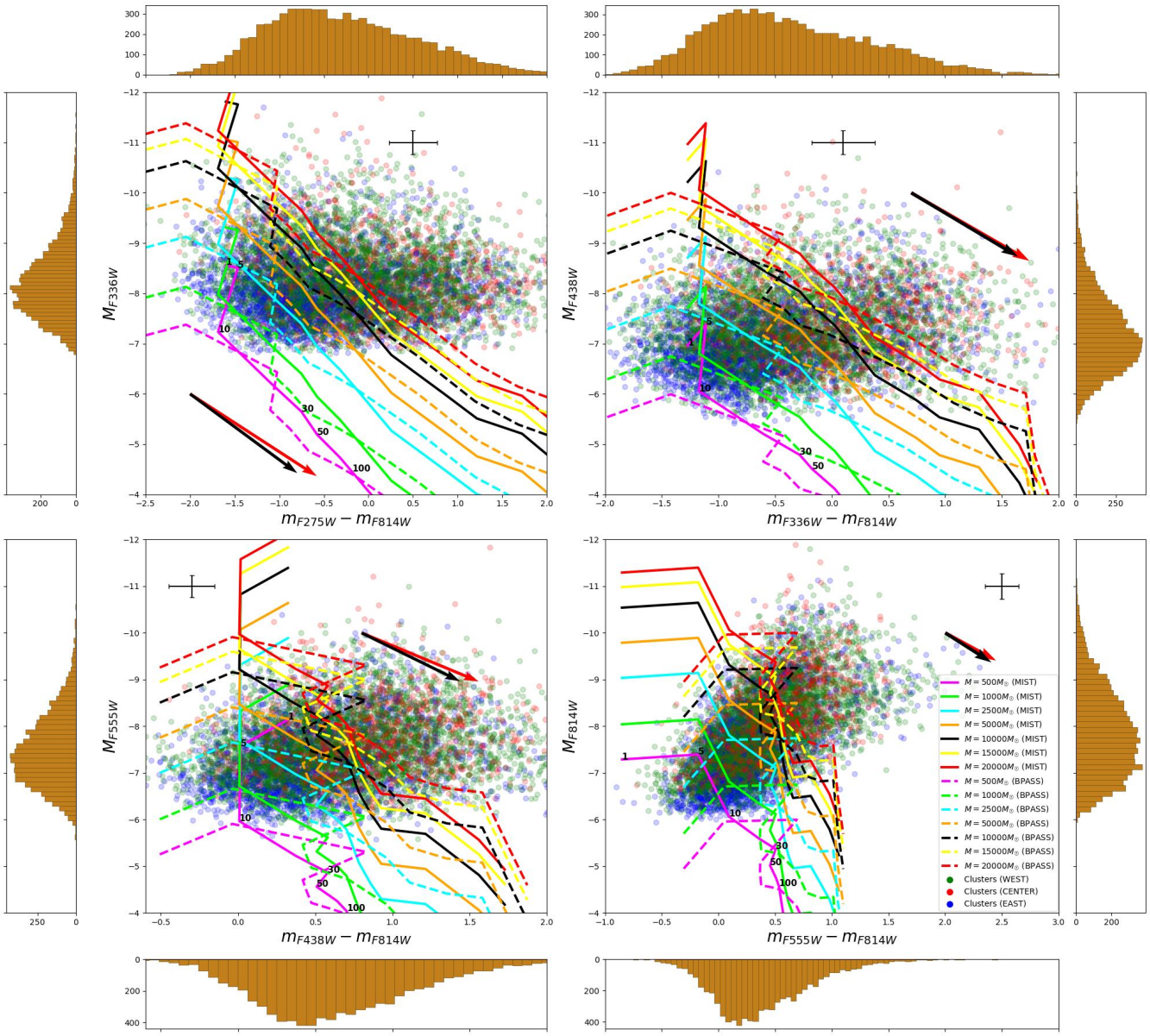

Figure 18: Color-Magnitude diagrams created using the cleaned catalogue sources. The red and the black vector show the effect of extinction of $A_V = 1$ mag for the Cardelli and the Calzetti attenuation laws respectively. The point with the error bars indicates the average errors of the data on the plot. This time only the west inner and outer spiral sources are plotted with the same symbol (green points). The central sources are colored red and the east region sources are colored blue. The solid lines correspond to MIST models while the dashed lines to the BPASS models. The various colors indicate different masses. Notice that the east side clusters tend to be less luminous. This was expected even from the true color image where the east side clusters appear dimmer in comparison to those in the west side (left image in fig. 4)

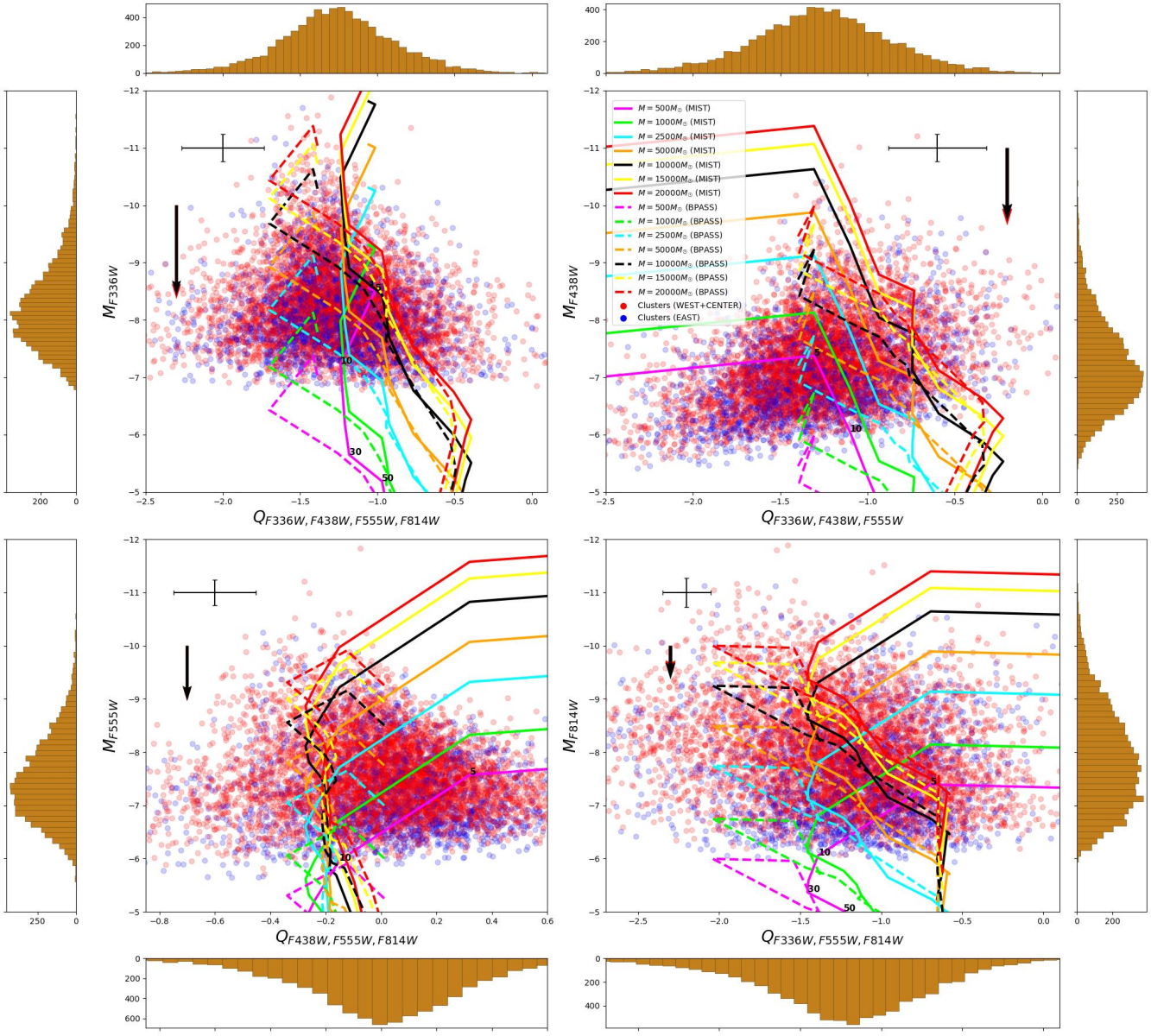

Figure 19: Q-Magnitude diagrams created using the cleaned catalogue sources and the Cardelli attenuation law. The structure is the same as in fig. 18, with the exception that now only east region sources were considered separately (blue points) from all other regions (red points). The structure seems to be in better agreement with the BPASS tracks contrary to the MIST tracks.

(though not lower than $10^3\,M_\odot$). Regarding the variation of the cluster population between the different regions of the galaxy, we can see that there is now a difference in the Q-Q diagrams, with the east side clusters generally being less luminous.

3.4 The Effect of Metallicity and Absorption

So far we only assumed the metallicity of Wolter et al., 2015, $Z = 0.22Z_\odot$. In this section we create Color-Color, Q-Q, Color-Magnitude and Q-Magnitude diagrams with evolutionary tracks of different metallicities to investigate how variations on metallicity affect the tracks. Since not all clusters are expected to have the same metallicity, and the observed data are essentially a combination of evolutionary tracks of different metallicities (of course other parameters may vary as well), this is necessary to see to what degree the variation of the tracks can explain the scatter of the data.

In the C-C diagrams shown in fig. 20 and the Q-Q diagrams shown in figs. 21 and 22, we have plotted tracks (again both for MIST and BPASS isochrones; solid and dashed lines respectively) with metallicities $Z = 0.22Z_\odot$, $Z = 0.5Z_\odot$ and $Z = Z_\odot$. CMDs (fig. 23) and QMDs (fig. 24) tracks for clusters of different metallicities are also plotted, but assuming only a single mass of $M = 5000M_\odot$ (and $M/L = 1$ as was done in Section 3.3) to avoid confusion.

Notice that on the C-C diagrams, as metallicity increases, the tracks generally move towards redder colors, as explained in Section 3.1. However, varying the metallicity does not have a great effect on the form of the tracks. Though, it indicates that some clusters might have super-solar metallicities. Contrary, in the Q-Q diagrams we see that varying the metallicity changes the shape of the tracks significantly. Even though they vary enough to explain most of the data, when the F275W filter was used in the calculation of some Q parameter (see fig. 22), the tracks are systematically shifted away from the data. This could be because of poor F275W photometry (see Section 2.1). It is also important to note the large errors in the Q-Q diagrams which explains the large scatter of the data. Similar results can be inferred by the CMDs (fig. 23) and QMDs (fig. 24).

So far, we also assumed for the tracks that they have zero absorption and used the extinction vectors to indicate the effect of absorption. For illustration purposes, in the C-C diagrams of fig. 25, we have plotted evolutionary tracks for MIST and BPASS models (solid and dashed lines respectively) for zero extinction (green lines) and $A_V = 1$ mag extinction (orange lines). Comparing the shape of the tracks and the observed distribution of the clusters indicates that most of the clusters have an extinction less than $A_V = 1$ mag (probably around $A_V \sim 0.5$ mag).

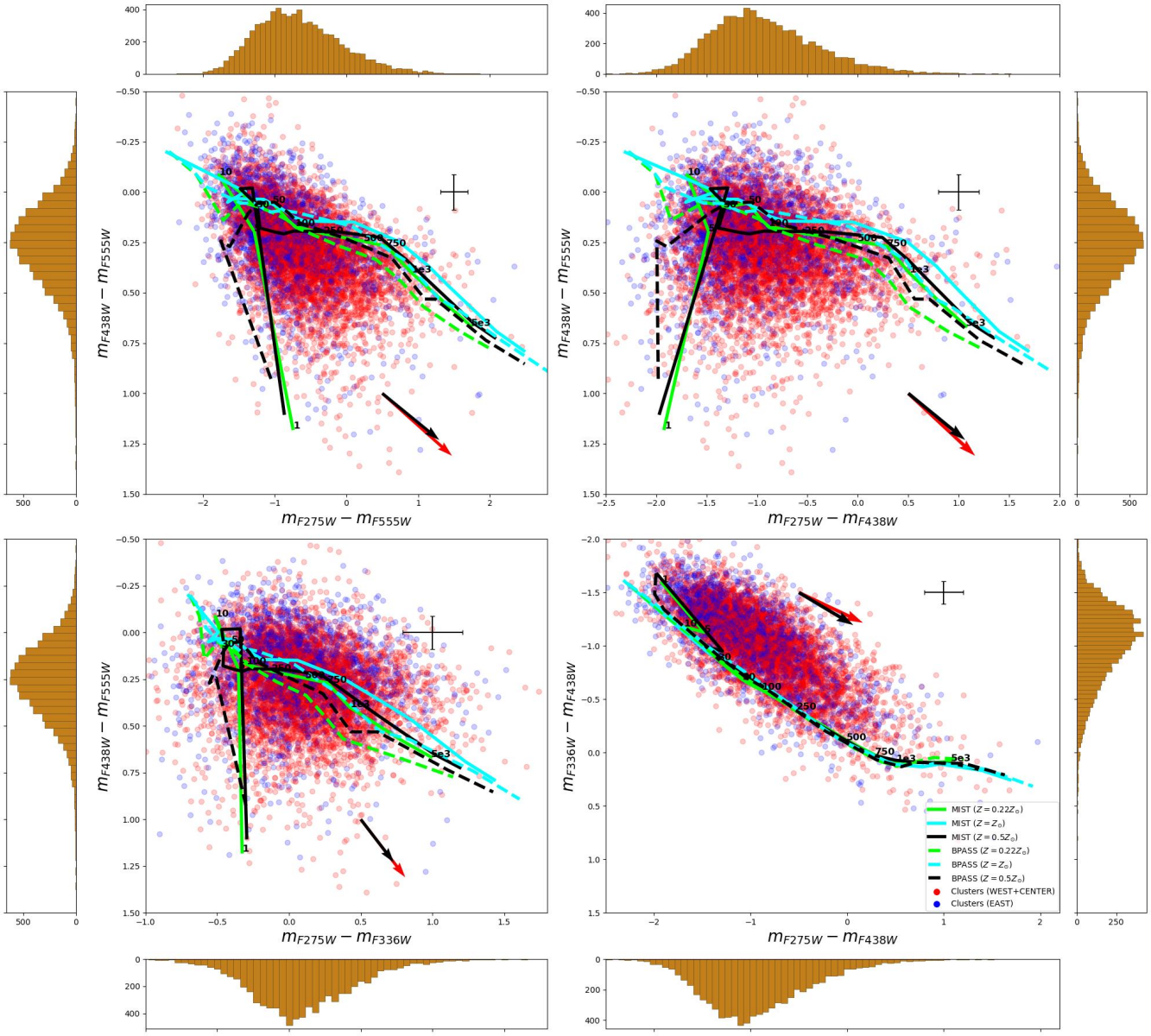

Figure 20: Color-color diagrams for different metallicities. See fig. 12 for a description of the points. The dashed lines correspond to BPASS tracks and the solid lines correspond to MIST tracks, of varying metallicity.

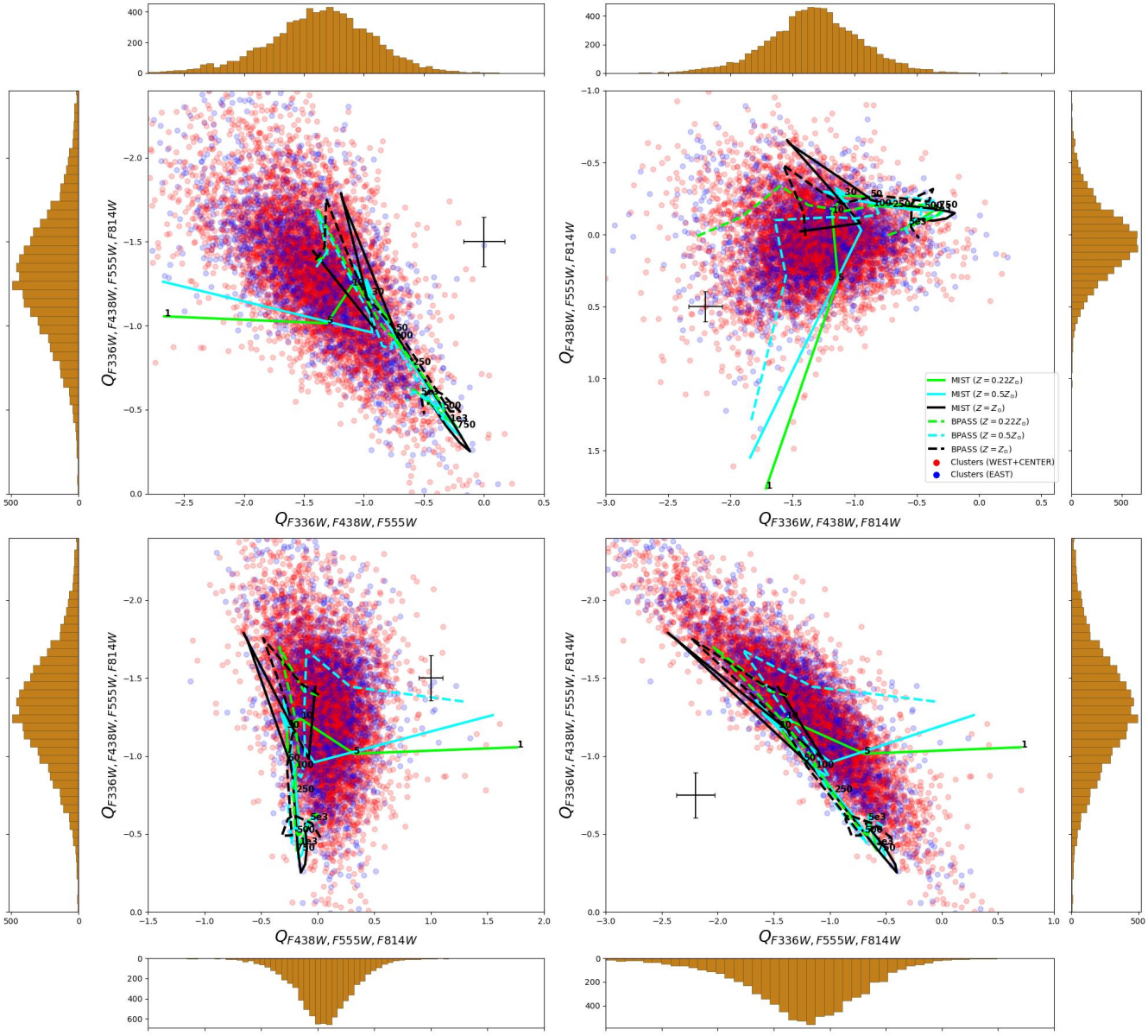

Figure 21: Q-Q diagrams for different metallicities. For a description of the points see fig. 12. The dashed lines correspond to BPASS tracks and the solid lines correspond to MIST tracks, of varying metallicity. The disagreement between the tracks and the data we noticed for $Z = 0.22Z_\odot$ (see fig. 15) seems to be fully explained by the variation in metallicity.

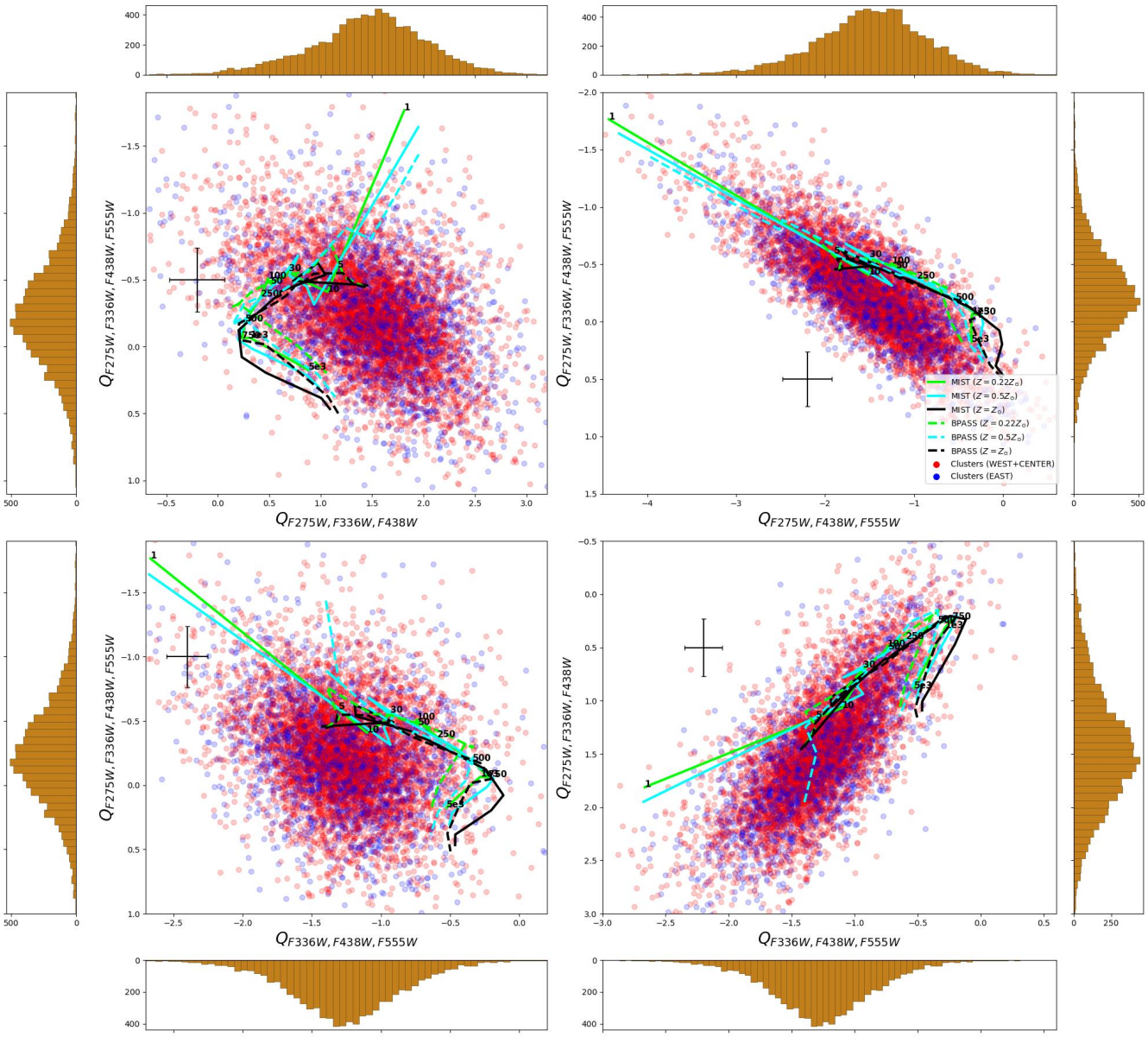

Figure 22: Q-Q diagrams for different metallicities. For a description of the points see fig. 12. The dashed lines correspond to BPASS tracks and the solid lines correspond to MIST tracks, of varying metallicity. Different metallicity does not seem to completely explain the disagreement between the offset tracks and the data.

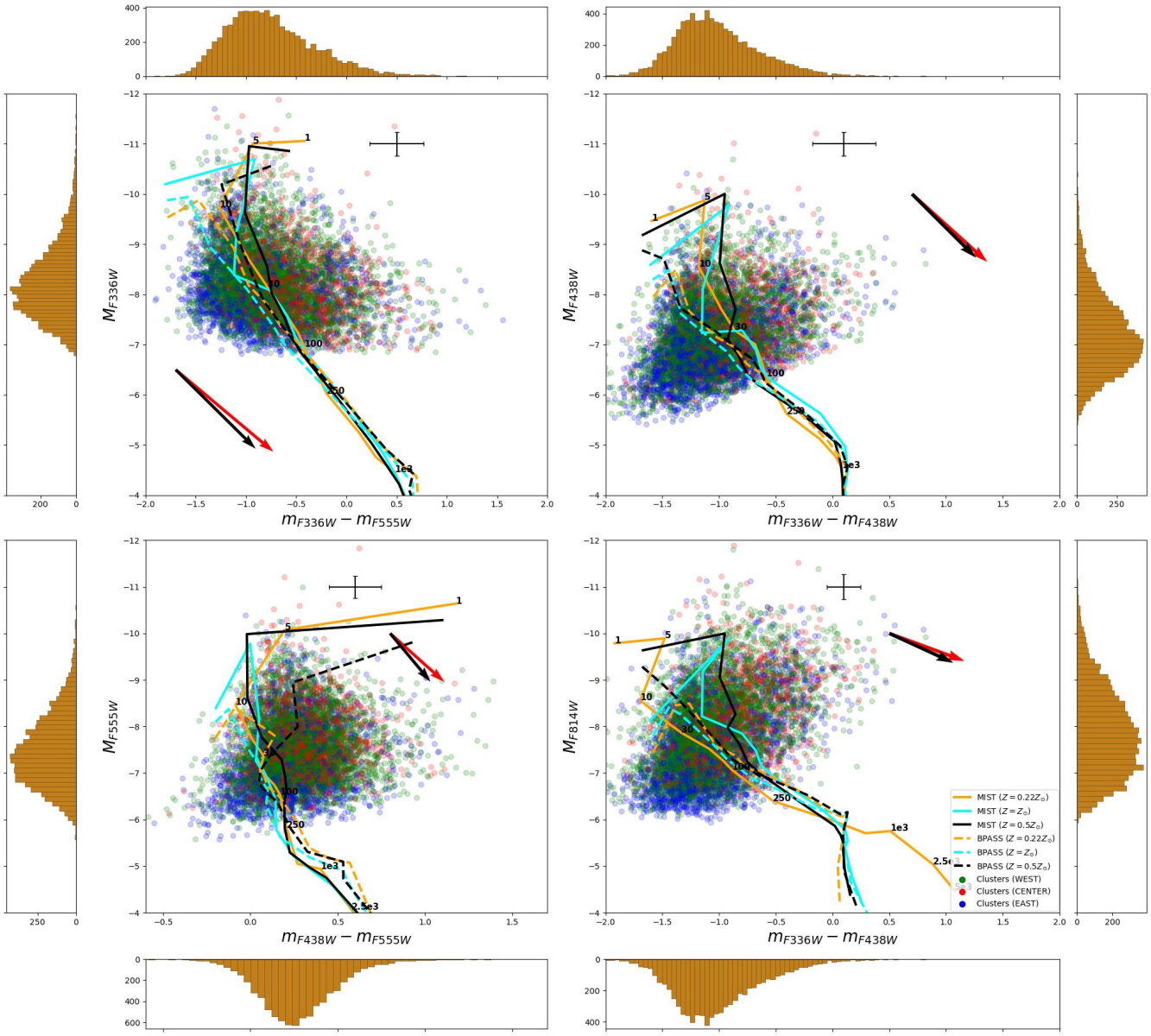

Figure 23: Color-Magnitude diagrams for different metallicities. For a description of the points see fig. 18. Only a single track was chosen for clarity (which corresponds to total cluster mass of $5000 M_\odot$)

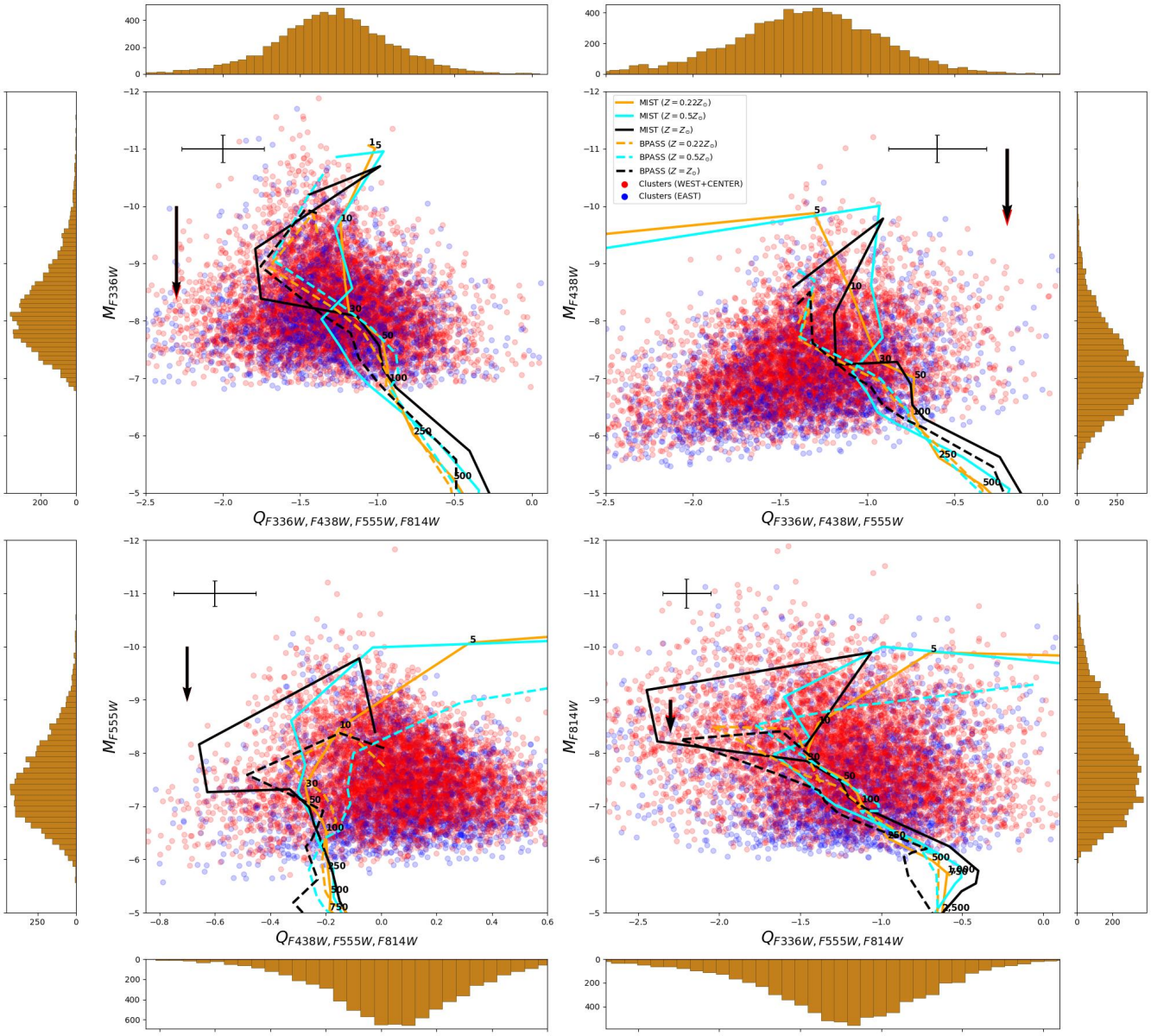

Figure 24: Q-Magnitude diagrams for different metallicities. For a description of the points see fig. 19. Only a single track was chosen for clarity (which corresponds to a total cluster mass of $5000 M_\odot$)

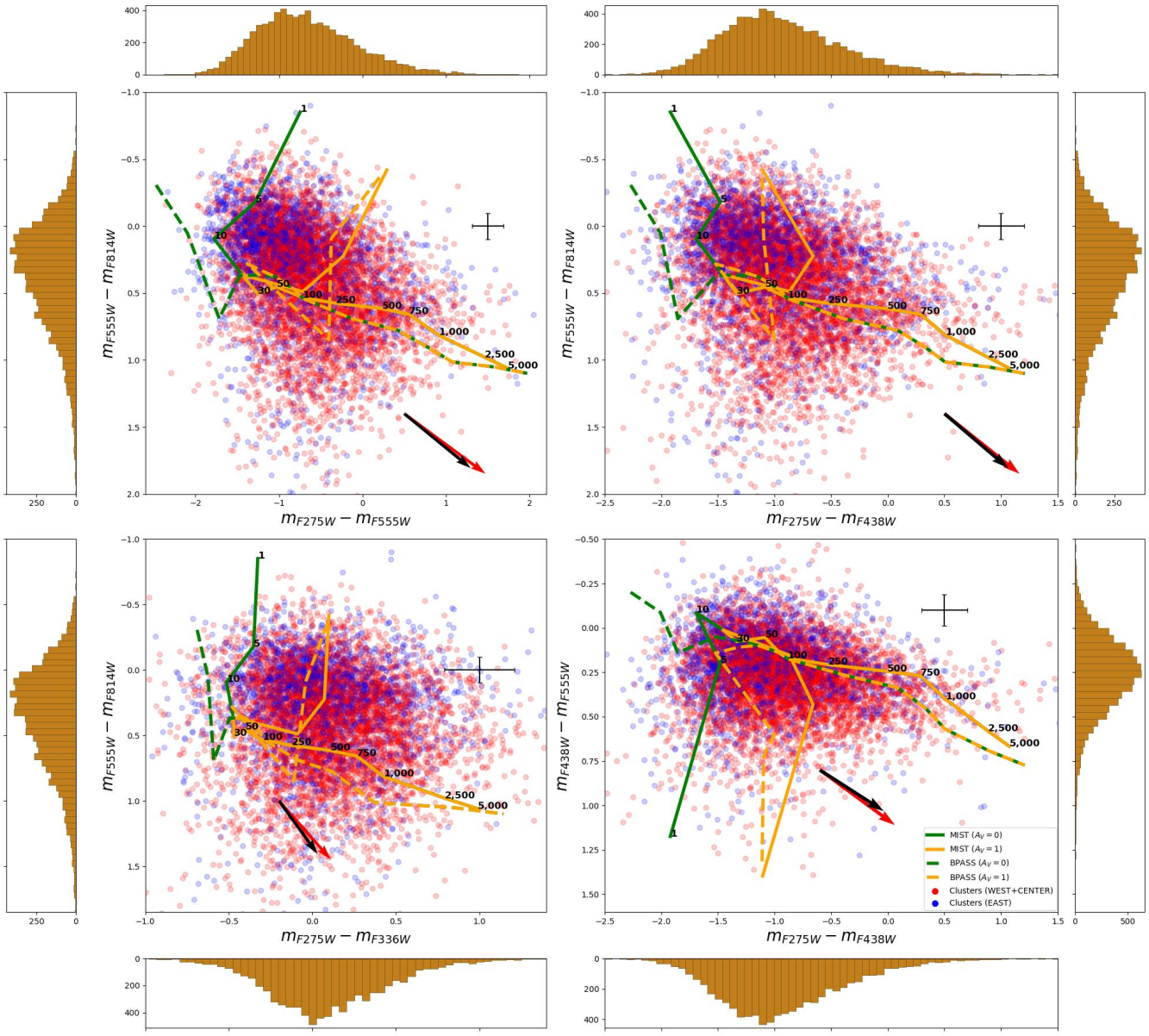

Figure 25: C-C diagrams for zero extinction $A_V = 0$ (green colored tracks) and for $A_V = 1$ mag (orange colored tracks; using a Calzetti attenuation law). the MIST tracks are shown with solid lines, while the BPASS tracks are shown with the dashed lines. Notice how the peak of the cluster distribution is closer to the $A_V = 0$ lines than than the $A_V = 1$ mag lines, indicating an extinction larger than $A_V = 0$, but not as high as $A_V = 1$ mag.

3.5 Spectral Energy Distribution Fitting

In order to determine more accurately the characteristics of each cluster, a method known as spectral energy distribution (SED) fitting is utilized. SED refers to the energy of the cluster as a function of wavelength. Since only 5 filters were used, each cluster's SED must be derived using only 5 points. The magnitude on each filter gives the luminosity of the cluster, at the effective wavelength of that filter. Measuring the cluster parameters (e.g. mass, age, extinction, metallicity) boils down to finding the best fitting SPS model to the SED of each cluster. Since we expect our parameters to have non-Gaussian and perhaps correlated errors, a simple maximum-likelihood estimation (χ^2 minimization) is not optimal. Rather one needs to follow a Bayesian approach and calculate the probability density function (PDF) of obtaining a set of parameters Θ (i.e. cluster parameters), given our data, D (i.e. the cluster SED), and our model M (i.e. the SPS models). That is known as a posterior probability, $P_M(\Theta|D)$, and can be calculated, according to Baye's rule, as:

$$P_M(\Theta|D) = \frac{P_M(D|\Theta)P_M(\Theta)}{P_M(D)} \tag{5}$$

On the right hand side we have the probability of obtaining the data given a set of parameters Θ, $P_M(D|\Theta)$ for a given set of models (i.e. isochrones), which is known as the likelihood, and the probability of the model parameters $P_M(\Theta)$ for the same set of models, which is known as the prior (since it just constitutes an initial guess of the parameters PDF, therefore encoding our "prior" knowledge), on the nominator. On the denominator, we have the so called evidence, which is basically a normalization constant. The most common notation is:

$$\mathcal{P}(\Theta) = \frac{\mathcal{L}(\Theta)\pi(\Theta)}{\mathcal{Z}} \tag{6}$$

In this investigation, the Prospector code (B. D. Johnson et al., 2021) was used for the SED fitting. For the SPS it uses Fsps and implements a dynamic nested sampling algorithm (nested sampling was developed in Skilling et al., 2004; Skilling, 2006, while dynamic nested sampling was developed by Higson et al., 2019) which is provided in the Dynesty code. The main motivations behind using Dynesty instead of other popular codes such as emcee (Foreman-Mackey et al., 2013); (Speagle, 2020; Koposov et al., 2023) which applies a Markov Chain Monte Carlo method, are the well defined stopping criteria as well as the computational efficiency. Dynamic nested sampling gives high quality posteriors in a fraction of the time required by MCMC methods.

Regarding our SPS model, every parameter available in Fsps can be used as a free parameter that can be fit in Prospector. Given the small number of bands and the increased computational time for a larger set of fitted parameters, the free parameters used for the fit were only the age, attenuation and mass of the cluster. Fitting metallicity did not give any useful constraints. For that reason we chose to keep a constant metallicity at $Z = Z_\odot$ and fit for the other parameters (this is a common practice). Although attenuation can also be strongly correlated with the age of the clusters, it is easier to constrain, since we use five filters, meaning we have access to different colors and can infer the attenuation by comparing how much each color is affected[16]. All other Fsps parameters were fixed to the same values as in Section 3.1. Of course, nebular emission was also included. For each cluster, two different Prospector runs were carried out, one with a model

[16]Metallicity also affects colors but to a much smaller degree.

using the MIST isochrones and the other using the BPASS isochrones.

The prior mass distribution was selected to be a *log-uniform* distribution[17] with a lower bound of $50M_{\odot}$ and an upper bound of $10^6 M_{\odot}$. This is an informative prior covering a wide range of masses. As for the normalization of the optical depth in the V band (as described in Conroy et al., 2009; dust2 parameter) we select a uniform distribution bounded between 0 and 2. Regarding age we select a uniform distribution bounded between 0.1 Myr - 4 Gyrs.

Since this is a very computationally expensive task, it was only performed to 20 randomly selected clusters that cover all galactic regions (see fig. 9 and fig. 10). BPASS runs took significantly more time to run. The photometric errors for each band had a minimum value of 0.175 mag. This value was introduced to account for uncertainties in the photometry that are not reflected in the photometric error that is calculated based on the number of counts. In table 4, the values of each parameter are shown for each one of the 20 clusters (whose photometry is shown in table 2). The lower limit corresponds to the 16% quantile of the posterior, the actual value of the parameter to the 50% quantile and the upper limit to the 84% quantile, therefore spanning a 1σ interval. In figs. 26, 27, 28, 29 the posteriors are plotted in the form of corner plots (top row) for SPS models with MIST (left) or BPASS (right) isochrones. The best-fit spectra together with the residuals (in units of σ) are also plotted (bottom row). The flux is in units of maggies[18].

The way to assess the goodness of the fit is to look at the residuals (for instance see fig. 26 (c) or (d) where the residuals are shown on the upper side of the diagram in units of σ). By convolving the best-fit spectrum with the transmission curves of our filters we compare with our input photometry. If their difference is small (small residuals), it means that the best-fit describes well our data.

An extremely helpful diagnostic tool are the cornerplots (for instance see fig. 26 (a) or (b)). Located on the diagonal of the corner plots are the posterior distributions for each parameter of the fit. The off diagonal plots showcase the correlation between any pair of those parameters. There is additional information that can be inferred from the posteriors. For instance, if a posterior is multimodal (has multiple peaks), that indicates the existence of a degeneracy. It is hard to know whether that is attributed to bad model selection or there is an intrinsic degeneracy in the free parameters of the model and more data are required to constrain our fitting to only one solution. Additionally, if a posterior is the same as the prior, that means that the parameters did not provide any information on the model. Finally, a very spread out posterior means large uncertainty in the parameter estimation. This could also be attributed to the lack of data that would allow us to restrict the model.

Note that there is a large discrepancy (of $\sim$ 1 order of magnitude) between the best-fit parameters obtained using a model with MIST isochrones versus a model with BPASS isochrones, for most sources. For some of them, this can be explained by one of the two models providing a better fit than the other. An example can be seen in fig. 26. In that case it is easy to see from the residuals, that the BPASS fit has significant residuals in comparison to the MIST fit. Fig. 27 shows a similar case. Here, the MIST residuals are larger and show some structure compared to the BPASS residuals, so one could argue that the BPASS fit is much better. In other cases, such as the one shown in fig. 28, it is not so easy to judge the results. Even though the residuals in panel (d) show some structure, they have similar degree of deviation as the other fit. Additionally,

[17] *log-uniform*$(x|a,b) = \frac{1}{x \times \log \frac{b}{a}}$ for $a < x < b$ and 0 otherwise.

[18] Maggies are defined as $f_{vmaggies} = 10^{0.4 \times m_{AB}}$ where m_{AB} is the magnitude in the AB magnitude system.

ID	$M_{MIST}(\times 10^3 M_\odot)$	t_{MIST} Myr	$\mathrm{dust2}_{MIST}$	$M_{BPASS}(\times 10^3 M_\odot)$	t_{BPASS} Myr	$\mathrm{dust2}_{BPASS}$	Region
4558	$9.54^{+3.43}_{-2.68}$	$90.35^{+46.69}_{-36.75}$	$0.26^{+0.23}_{-0.17}$	$0.47^{+0.17}_{-0.11}$	$2.75^{+1.5}_{-1.8}$	$0.54^{+0.23}_{-0.26}$	Center
4764	$6.09^{+2.55}_{-1.79}$	$65.08^{+38.4}_{-25.06}$	$0.12^{+0.14}_{-0.08}$	$0.88^{+0.26}_{-0.20}$	$3.69^{+1.03}_{-1.31}$	$0.52^{+0.18}_{-0.21}$	West (inner)
6161	$0.56^{+1.49}_{-0.16}$	$3.21^{+20.01}_{-1.56}$	$0.61^{+0.26}_{-0.50}$	$9.86^{+2.16}_{-1.82}$	$111.80^{+47.21}_{-38.09}$	$0.17^{+0.25}_{-0.13}$	Center
135	$41.42^{+14.79}_{-11.18}$	$58.21^{+30.29}_{-23.52}$	$0.22^{+0.21}_{-0.15}$	$36.62^{+11.18}_{-9.00}$	$60.16^{+56.23}_{-28.91}$	$1.26^{+0.34}_{-0.42}$	East
962	$9.35^{+1.10}_{-0.99}$	$32.69^{+3.84}_{-2.69}$	$0.029^{0.046}_{0.021}$	$111.49^{+17.77}_{-15.29}$	$340.26^{+49.23}_{-55.42}$	$0.15^{+0.18}_{-0.11}$	West (outer)
681	$11.18^{+1.35}_{-1.18}$	$32.92^{+4.07}_{-2.71}$	$0.03^{+0.04}_{-0.02}$	$2.39^{+0.78}_{-1.21}$	$23.13^{+11.73}_{-14.86}$	$0.14^{+0.24}_{-0.10}$	East
2880	$4.51^{+0.55}_{-0.47}$	$32.81^{3.98}_{-2.90}$	$0.03^{+0.05}_{-0.02}$	$5.50^{+1.33}_{-1.18}$	$53.06^{+29.19}_{-21.14}$	$0.15^{+0.20}_{-0.11}$	East
744	$12.90^{+2.54}_{-1.86}$	$32.27^{+6.96}_{-4.89}$	$0.05^{+0.07}_{-0.04}$	$5.76^{+1.28}_{-1.27}$	$59.52^{+29.98}_{-24.62}$	$0.18^{+0.22}_{-0.13}$	East
5652	$2.25^{+0.25}_{-0.23}$	$32.64^{+3.61}_{-2.35}$	$0.03^{+0.04}_{-0.02}$	$11.23^{+4.80}_{-3.49}$	$9.39^{+3.55}_{-1.71}$	$1.52^{+0.26}_{-0.28}$	East
284	$128.72^{+39.98}_{-27.21}$	$375.86^{+230.24}_{-173.18}$	$0.41^{+0.50}_{-0.31}$	$6.99^{+1.25}_{-1.03}$	$27.46^{+8.86}_{-3.72}$	$0.07^{+0.09}_{-0.05}$	West (out)
2510	$5.07^{+0.76}_{-0.56}$	$33.60^{+5.45}_{-3.01}$	$0.04^{+0.05}_{-0.03}$	$115.87^{+28.28}_{-19.94}$	$333.06^{+97.82}_{-115.78}$	$0.42^{+0.37}_{-0.29}$	West (out)
2325	$8.23^{+3.12}_{-2.54}$	$13.13^{+1.37}_{-1.51}$	$1.19^{+0.22}_{-0.23}$	$0.65^{+0.16}_{-0.14}$	$3.99^{+0.97}_{-1.05}$	$0.15^{+0.14}_{-0.10}$	West (in)
5525	$4.06^{+2.03}_{-1.20}$	$58.95^{+42.20}_{-21.98}$	$0.10^{+0.13}_{-0.07}$	$13.40^{+6.75}_{-7.47}$	$16.95^{+14.18}_{-13.94}$	$0.25^{+0.68}_{-0.19}$	East
6390	$3.84^{+1.69}_{-1.02}$	$53.80^{+32.65}_{-18.69}$	$0.10^{+0.12}_{-0.07}$	$1.54^{+0.47}_{-0.36}$	$3.06^{+1.37}_{-2.09}$	$0.52^{+0.19}_{-0.22}$	West (out)
6588	$0.32^{+0.13}_{-0.09}$	$2.51^{+1.61}_{-1.64}$	$0.51^{+0.25}_{-0.27}$	$4.05^{+1.32}_{-0.96}$	$3.22^{+1.24}_{-2.10}$	$0.59^{+0.19}_{-0.24}$	Center
219	$24.56^{+10.28}_{-7.50}$	$64.49^{+42.37}_{-30.16}$	$1.10^{+0.26}_{-0.30}$	$12.10^{+1.75}_{-2.79}$	$24.78^{3.14}_{8.10}$	$0.04^{+0.06}_{-0.03}$	West (out)
2377	$125.47^{+22.24}_{-20.22}$	$418.48^{+80.74}_{-78.47}$	$0.12^{+0.16}_{-0.08}$	$61.82^{+14.65}_{-12.72}$	$56.73^{+32.23}_{-26.25}$	$0.36^{+0.30}_{-0.23}$	Center
4446	$9.71^{+3.12}_{-2.86}$	$138.49^{+57.56}_{-53.98}$	$0.13^{+0.17}_{-0.09}$	$2.98^{+1.21}_{-1.30}$	$17.74^{+13.10}_{-11.09}$	$0.24^{+0.35}_{-0.16}$	East
5422	$2.51^{+0.28}_{-0.25}$	$32.76^{+3.38}_{-2.31}$	$0.03^{+0.04}_{-0.02}$	$8.38^{+1.74}_{-1.74}$	$63.09^{+28.54}_{-27.25}$	$0.21^{+0.23}_{-0.15}$	West (in)
7216	$0.17^{+0.05}_{-0.03}$	$3.48^{+0.72}_{-1.44}$	$0.26^{+0.19}_{-0.16}$	$12.15^{+2.94}_{-2.31}$	$86.27^{+46.17}_{-41.93}$	$0.35^{+0.33}_{-0.24}$	East

Table 4: Cluster parameters obtained by PROSPECTOR SED fitting using DYNESTY for 20 random clusters from the cleaned catalogue (see table 2). The first column is the ID of the clusters in table 2; columns (2) and (5) give the mass (in units $10^3 M_\odot$) of the cluster for the MIST and BPASS isochrones fits respectively; columns (3) and (6) give the ages of the clusters in Myr; columns (4) and (7) give the normalization of the optical depth in the optical band (as described in Conroy et al., 2009; dust2 parameter); column (8) indicates the region where the cluster is located, as defined in fig. 8

.

the corresponding cornerplots show some bi-modality, even though it is not extreme. This causes trouble in interpreting the results, especially in a case like that where the parameters differ by an order of magnitude. Another similar example is shown in fig. 29. In that case the residuals on panel (c) (MIST model) are very small (not a single value exceeds 0.5σ), but the difference with panel (d) (BPASS) is not extraordinary (only 1 point of the BPASS model has $\sim 1\sigma$ residual). Additionally, the dust2 posterior from the MIST model (a) has a very prominent bi-modality with two peaks being almost as likely. However, the uncertainty in model selection when coming to SED fitting has been a matter of discussion for a long time, and there does not seem to be a clear answer (Conroy, 2013).

These uncertainties on model selection make it hard to reach to a conclusion regarding any difference of the star-cluster population in sub-galactic scale. However, we can still examine the subject in the context of each model separately. For instance, we can see that if we consider the MIST model, the extinction seems to be smaller on the east side (dust2 is of the order ~ 0.01), contrary to the other regions (where dust2 is of the order ~ 0.1). This is in agreement with the Color-Color diagrams discussed in Section 3.2. On the other hand, considering the BPASS model, there is no significant difference on the extinction between different regions of the galaxy. Regarding the cluster mass and age, there is not any apparent difference between regions under any of the two models.

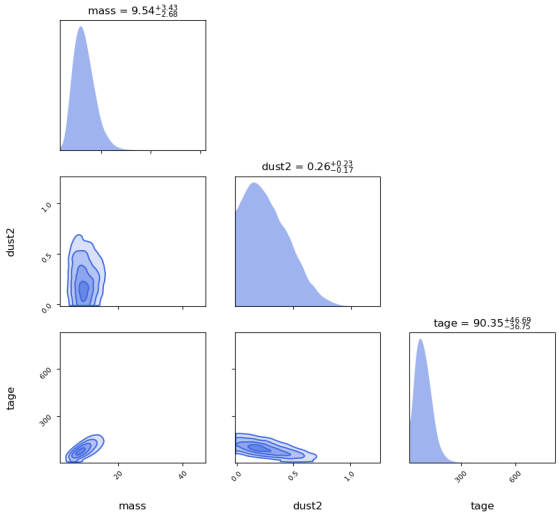

(a) Corner plots (MIST)

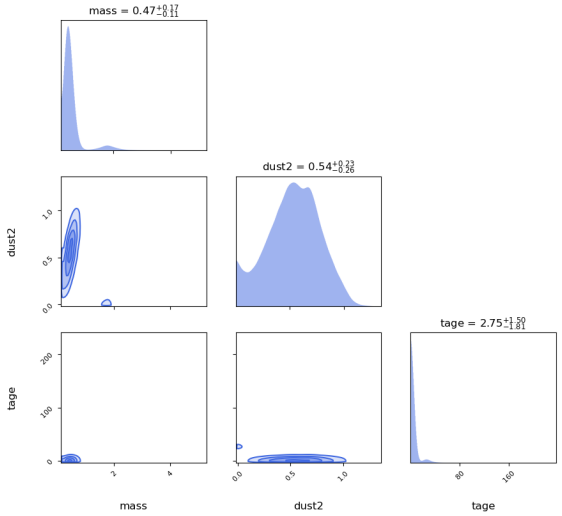

(b) Corner plots (BPASS)

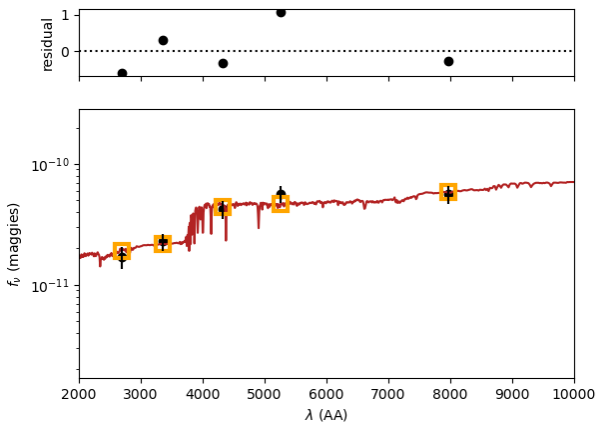

(c) Best-fit spectrum (MIST)

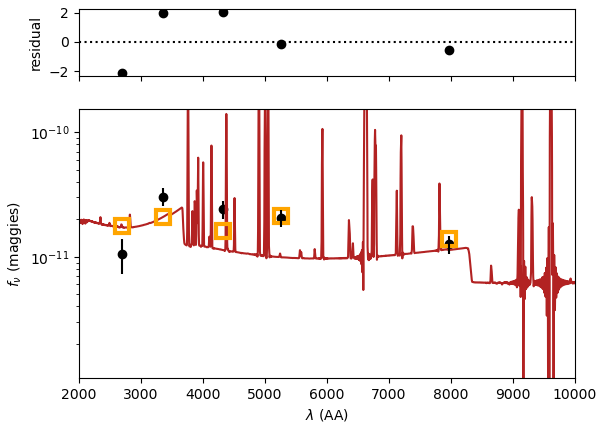

(d) Best-fit-spectrum (BPASS)

Figure 26: Corner plots (above) and best-fit spectra (bellow) for the cluster with ID 4558, fitted using MIST (left) or BPASS (right) isochrones. Notice that the fit using MIST isochrones is much better (small residuals) than the one using the BPASS isochrones. That could possibly mean that the large discrepancy between the mass and age for this cluster is attributed to one model providing a much better fit than the other.

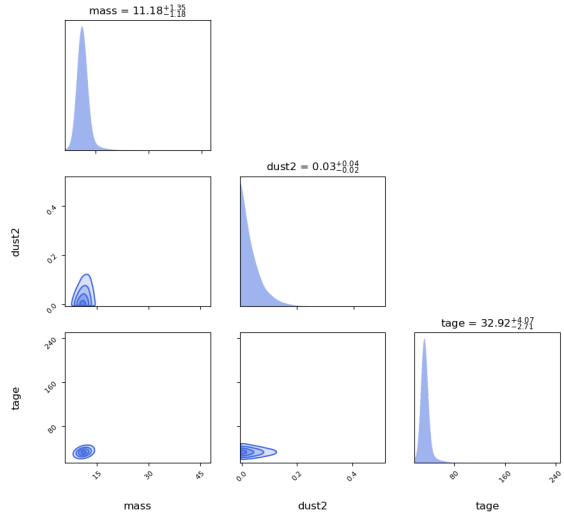

(a) Corner plots (MIST)

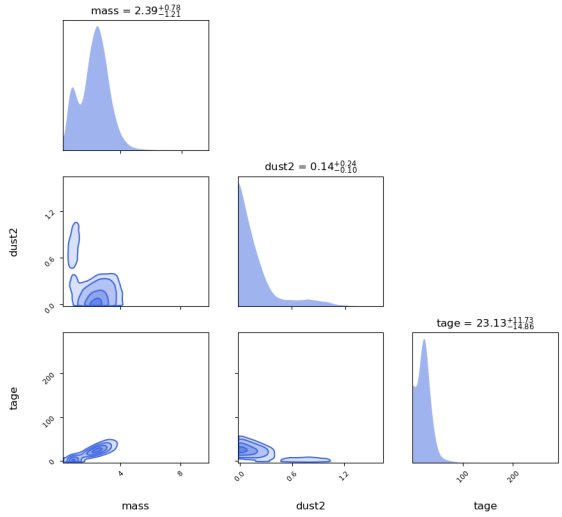

(b) Corner plots (BPASS)

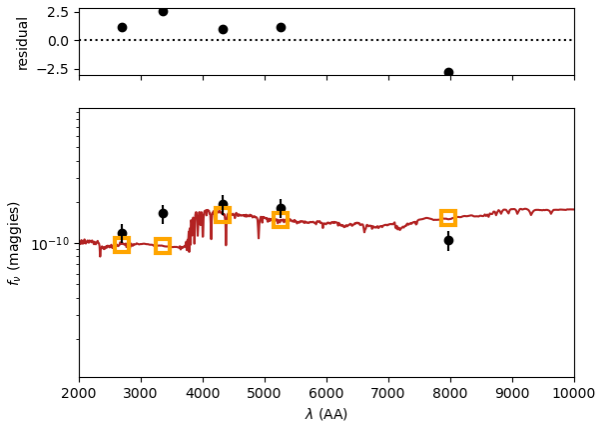

(c) Best-fit spectrum (MIST)

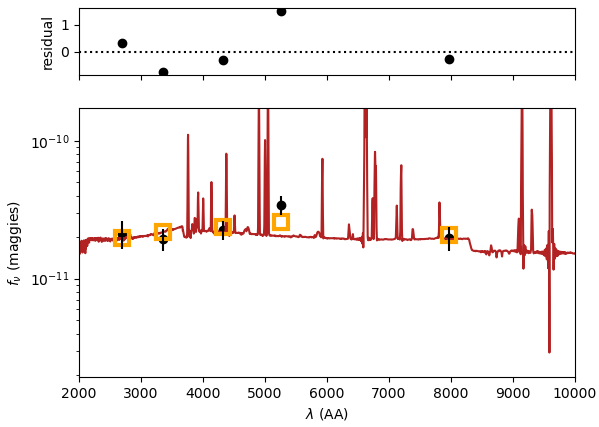

(d) Best-fit-spectrum (BPASS)

Figure 27: Corner plots (above) and best-fit spectra (bellow) for the cluster with ID 681, fitted using MIST (left) or BPASS (right) isochrones. Note that the residuals are larger in the MIST case and more structured so one could argue that the BPASS fit is better.

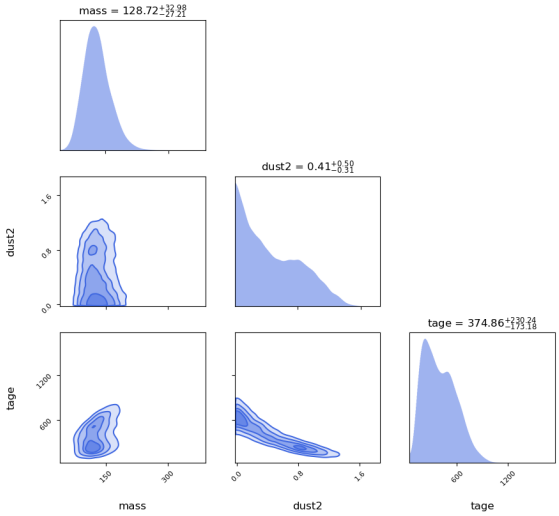

(a) Corner plots (MIST)

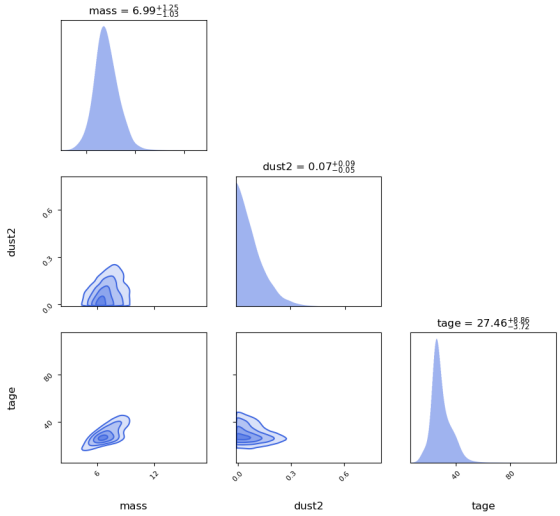

(b) Corner plots (BPASS)

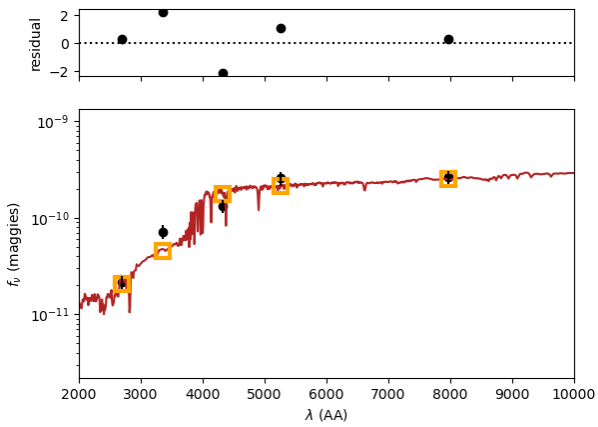

(c) Best-fit spectrum (MIST)

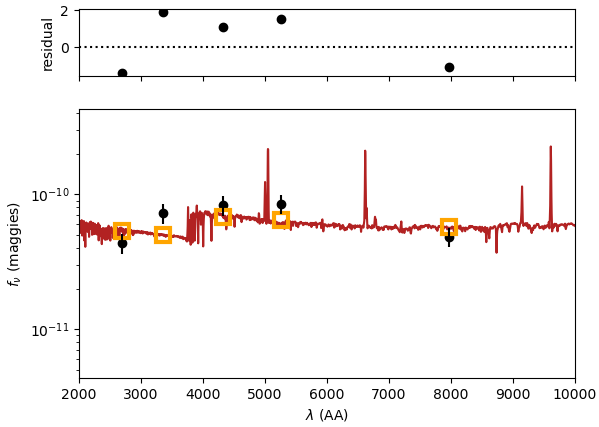

(d) Best-fit-spectrum (BPASS)

Figure 28: Corner plots (above) and best-fit spectra (bellow) for the cluster with ID 284, fitted using MIST (left) or BPASS (right) isochrones. In this case the discrepancy between the mass and age obtained by the two different models is not the result of a much worse fit by one of the two models, although the BPASS model shows more structured residuals than the MIST model.

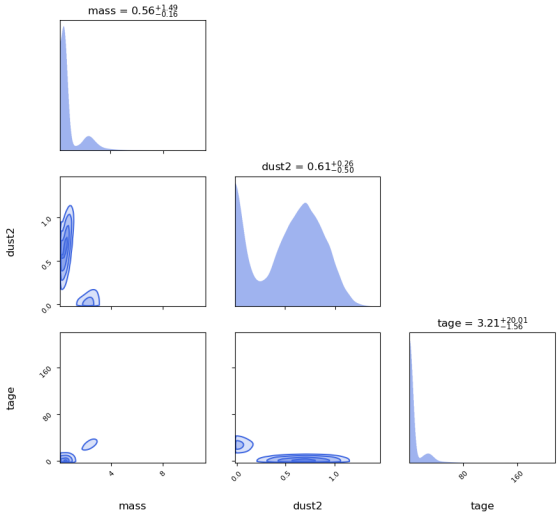

(a) Corner plots (MIST)

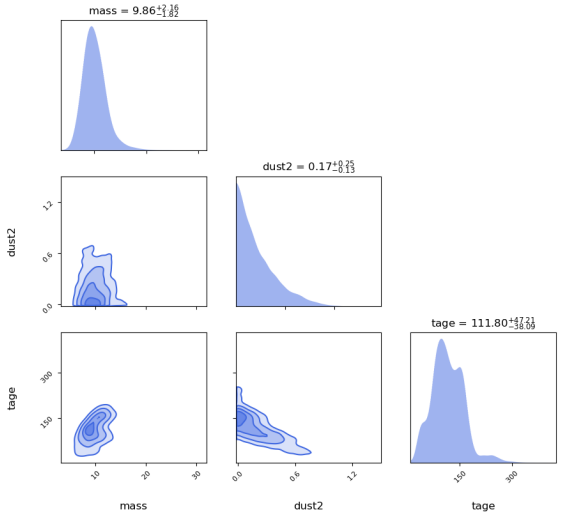

(b) Corner plots (BPASS)

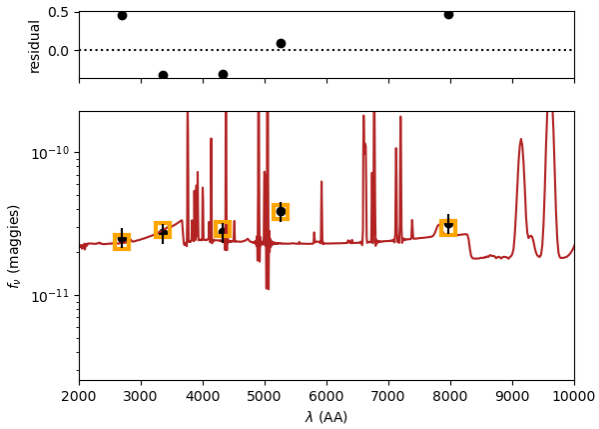

(c) Best-fit spectrum (MIST)

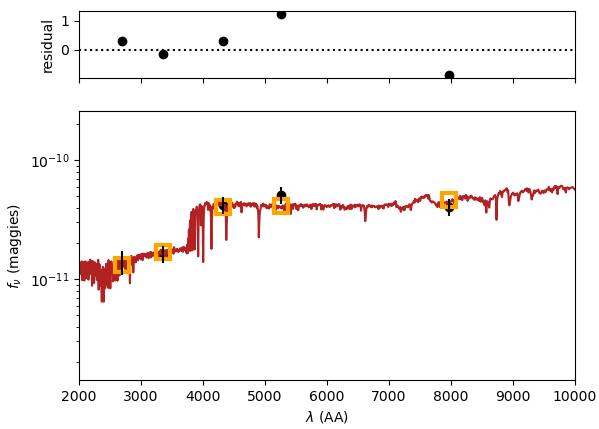

(d) Best-fit-spectrum (BPASS)

Figure 29: Corner plots (above) and best-fit spectra (bellow) for the cluster with ID 6161, fitted using MIST (left) or BPASS (right) isochrones. Note that residuals under both models look similar but for the model using MIST isochrones they are below 0.5σ so the fit can be considered better. However, there is only 1 point on (d) that exceeds 1σ, so the selection of one model instead of the other is not certain.

4 Cross Identification with X-ray Sources

The abundance of high luminosity X-ray sources and ULXs is one of the most exciting characteristics of NGC2276. Using the present catalogue along with the Anastasopoulou et al., 2019 catalogue of X-ray sources (see table 5), we can study possible correlations between the presence of XRBs and the age, mass or dust content of the cluster. The location of the X-ray sources on the galaxy can be seen in fig. 30. The X-ray catalogue contains two very interesting sources. Namely, source 6a is classified as a potential Intermediate Mass Black Hole (IMBH) candidate (Mezcua et al., 2018), while source 9b is thought to be the nucleus of the galaxy.

In order to identify possible XRB host clusters, we create a new catalogue using more relaxed criteria. Specifically, we require $\chi^2 < 4$ in F336W, F438W and F555W, and $\chi^2 < 5$ for F814W. For F275W no criteria are imposed this time (all other criteria for the remaining filters remain the same). This catalogue contains 37,765 sources. Then we search for all sources within a 1 arcsec radius centered on the X-ray source coordinates. This corresponds to a ~ 200 pc radius. We also find the nearest cluster to the X-ray source, which we consider to be the "best" optical counterpart candidate. In fig. 31 we show the X-ray sources (red cross), the search radius (red circle - sometimes cannot be seen whole), the best matched sources (magenta cross) and all the other possible sources (black crosses). Notice that source 18 has no matches. The photometry of best matched clusters is shown in table 6.

SED fitting was performed for the best-match clusters only, in the same manner as in Section 3.5. For the fitting, only the filters with good photometry (as in Section 3.5) were used. Inspecting table 7, we can see that the best-fit parameters calculated using models with MIST isochrones do not differ that much from the ones that used BPASS isochrones. In figs. 32-37 we show the corner plots and the best-fit spectra of selected sources. The best-fit spectra have relatively small residuals in general.

Inspecting the best-fit parameters, we note that the ages are rather large, most of them at ~ 100 Myrs. This is in disagreement with what we would expect. As discussed in 1, we would expect to find XRBs, and especially ULXs in YMCs. As already discussed, one source of error is the assumed isochrones, but both sets of isochrones give clusters with ages $10 - 100$ Myrs. Another issue is possible missidentification of the actual cluster counterpart of the X-ray source. In crowded fields, it is rather possible that the X-ray source was created in a different cluster than the one we considered as the 'best match'. That would be very probable in the case of sources like # 1, #3 or #5. Also source # 9^b which corresponds to the nucleus might have been confused. There is also the case of source #8, where there are obviously clusters closer to it but their photometry was so bad due to crowding that it did not even make into the relaxed catalogue. Then, there is the case of source # 18 which does not have a match within our catalogue. That could be a background source or an LMXB. Source # 19 could also be a background galaxy. Looking at the mass posterior (fig. 37), we can see its peak is at the upper limit of the prior, meaning that its mass is probably even higher than $10^6 M_\odot$, which is very unusual for clusters. That happens for both models. Other sources that could be background sources or LMXBs are # 15 and # 16. Those have only 2 and 1 matches in our catalogue respectively, even though we can see some cluster-like sources in the same frames that did not meet our cleaning criteria. For such X-ray sources we do not trust that their age is that of the corresponding clusters. A more physical explanation for the large ages, stemming from the clusters' very large masses, which indicate a high-density cluster, is the following: there is

higher chance of a lone compact object to acquire a companion star via N-body interactions. That could explain why the west-side X-ray emission is ~ 5 greater than the east-side, since dynamical formation may lead to more compact binaries and a higher fraction of Roche-lobe over-flow systems.

ID_X	RA (J2000) h:mm:ss	DEC (J2000) dd:mm:ss	L_X^{obs} (L_X^{cor}) $\times 10^{39}$ erg s^{-1} (0.3-10.0 keV) (OBSID 4968)	L_X^{obs} (L_X^{cor}) $\times 10^{39}$ erg s^{-1} (0.3-10.0 keV) (OBSID 15648)
1	7:26:36.6	+ 85:45:36.9	$1.0^{+270.3}_{-1.0}$(116.3)	0.47 ± 0.23(150.31)
2	7:26:37.4	+ 85:45:34.4	$16.9^{+2.0}_{-2.4}$(35.5)	8.2 ± 2.0(18.1)
3	7:26:43.3	+ 85:44:59.8	$2.2^{+2.8}_{-1.2}$(2.2)	0.8 ± 0.6(0.8)
4	7:26:46.1	+ 85:45:47.9	0.15 ± 0.16(0.19)	2.2 ± 0.6(2.8)
5	7:26:46.3	+ 85:45:38.2	$1.2^{+5.8}_{-1.0}$(3.8)	0.8 ± 0.2(2.4)
6^a	7:26:47.9	+ 85:45:52.2	7.2 ± 1.4(9.6)	8.0 ± 1.0(10.2)
7	7:26:48.2	+ 85:45:48.9	$7.2^{+1.4}_{-2.6}$(12.3)	23.9 ± 0.8(57.5)
8	7:26:48.2	+ 85:45:54.7	$11.6^{+1.0}_{-1.2}$(25.7)	12.5 ± 1.2(29.7)
9^b	7:27:13.0	+ 85:45:16.8	$0.4^{+3.8}_{-0.4}$(23.3)	0.63 ± 0.3(16.01)
10	7:27:14.8	+ 85:46:11.4	$0.5^{+0.4}_{-0.2}$(0.4)	0.201 ± 0.174(1349.1)
11	7:27:15.5	+ 85:45:54.7	0.31 ± 0.16(0.5)	1.2 ± 0.4(1.6)
12	7:27:19.8	+ 85:46:32.6	$0.6^{+0.4}_{-0.3}$(0.6)	$5.2^{+8.4}_{-3.8}$(7.6)
13	7:27:25.6	+ 85:45:25.8	$1.6^{+8.8}_{-1.4}$(30.9)	$1.6^{+2.0}_{-1.0}$(48.0)
14	7:27:28.7	+ 85:45:11.0	$0.4^{+0.8}_{-0.2}$(1.0)	0.4 ± 0.4(0.8)
15	7:27:34.4	+ 85:44:57.7	$0.4^{+83.9}_{-0.4}$(12.5)	0.1 ± 0.15(6.32)
16	7:27:53.5	+ 85:46:09.0	$1.6^{+4.2}_{-1.2}$(4.4)	$1.6^{+1.2}_{-1.0}$(4.4)
17	7:27:58.5	+ 85:44:37.7	$4.6^{+13.3}_{-3.8}$(4.6)	0.1 ± 0.28(0.12)
18	7:28:15.9	+ 85:44:36.1	1.0 ± 0.4(1.4)	$4.6^{+5.0}_{-2.4}$(5.8)
19	7:28:19.7	+ 85:44:28.0	$0.6^{+11.0}_{-0.6}$(0.7)	0.8 ± 0.6(1.0)

Table 5: The WCS coordinates and broad band photometry of X-ray sources in NGC2276 from Anastasopoulou et al., 2019 for two different *Chandra* observations (OBSID 4968 and OBSID 15648). The luminosities given in the parentheses are corrected for absorption. For more information on the observations and data reduction see Anastasopoulou et al., 2019.

ID_X	ID	RA (J2000) h:mm:ss	DEC (J2000) dd:mm:ss	mag(F275W) $\pm \Delta$mag	mag(F336W) $\pm \Delta$mag	mag(F438W) $\pm \Delta$mag	mag(F555W) $\pm \Delta$mag	mag(F814W) $\pm \Delta$mag
1	615	7:26:36.453321	85:45:36.818955	22.395 ± 0.046	22.917 ± 0.069	24.172 ± 0.034	24.232 ± 0.025	23.67 ± 0.031
2	17885	7:26:37.445271	85:45:34.520315	26.033 ± 0.382	27.15 ± 0.634	27.812 ± 0.29	26.552 ± 0.076	25.793 ± 0.101
3	20	7:26:43.276058	85:44:59.708404	20.874 ± 0.014	20.94 ± 0.009	22.09 ± 0.008	21.791 ± 0.005	21.194 ± 0.006
4	7505	7:26:46.120922	85:45:47.977623	25.351 ± 0.271	25.011 ± 0.107	25.644 ± 0.063	25.656 ± 0.045	25.565 ± 0.12
5	3327	7:26:46.291013	85:45:38.214869	25.33 ± 0.351	24.191 ± 0.101	25.663 ± 0.077	25.119 ± 0.037	24.583 ± 0.059
6^a	3933	7:26:47.818528	85:45:52.267900	-	25.459 ± 0.176	26.19 ± 0.097	25.565 ± 0.045	24.336 ± 0.042
7	4464	7:26:48.237602	85:45:48.762654	28.273 ± 3.342	26.642 ± 0.324	26.321 ± 0.088	25.513 ± 0.035	24.312 ± 0.043
8	2184	7:26:47.976383	85:45:54.917793	26.322 ± 0.729	24.513 ± 0.08	25.457 ± 0.061	24.954 ± 0.039	23.628 ± 0.034
9^b	383	7:27:12.857591	85:45:16.596902	23.934 ± 0.089	23.326 ± 0.034	24.152 ± 0.025	23.673 ± 0.014	22.854 ± 0.021
10	15457	7:27:14.978899	85:46:11.733722	25.778 ± 0.284	25.322 ± 0.103	26.462 ± 0.091	26.305 ± 0.054	26.414 ± 0.136
11	4670	7:27:15.350571	85:45:54.562160	26.727 ± 0.651	25.776 ± 0.154	25.944 ± 0.065	25.367 ± 0.031	24.754 ± 0.043
12	20608	7:27:19.747926	85:46:32.622563	25.384 ± 0.235	25.646 ± 0.15	26.365 ± 0.095	26.776 ± 0.084	27.35 ± 0.342
13	5144	7:27:25.588642	85:45:25.734122	25.972 ± 0.379	25.55 ± 0.136	26.402 ± 0.11	25.47 ± 0.035	24.529 ± 0.046
14	27082	7:27:28.586001	85:45:11.069924	28.009 ± 2.199	-	27.66 ± 0.32	27.044 ± 0.119	26.078 ± 0.158
15	36659	7:27:34.564036	85:44:57.967535	-	-	27.782 ± 0.283	27.446 ± 0.151	26.699 ± 0.212
16	26641	7:27:53.049700	85:46:8.678692	-	29.924 ± 5.798	27.0 ± 0.153	27.109 ± 0.1	26.14 ± 0.123
17	2677	7:27:58.444626	85:44:37.665800	-	25.45 ± 0.134	25.974 ± 0.065	25.212 ± 0.042	23.613 ± 0.024
18	-	-	-	-	-	-	-	-
19	38	7:28:19.511124	85:44:27.895908	-	24.938 ± 0.075	24.074 ± 0.019	22.908 ± 0.007	21.31 ± 0.006

Table 6: Photometry of star-clusters best matching the X-ray sources in the catalogue of Anastasopoulou et al., 2019 (ID_X refers to their ID). The - indicates that the photometry was invalid on that filter. Notice that for source 18 there are no matches in our catalogue

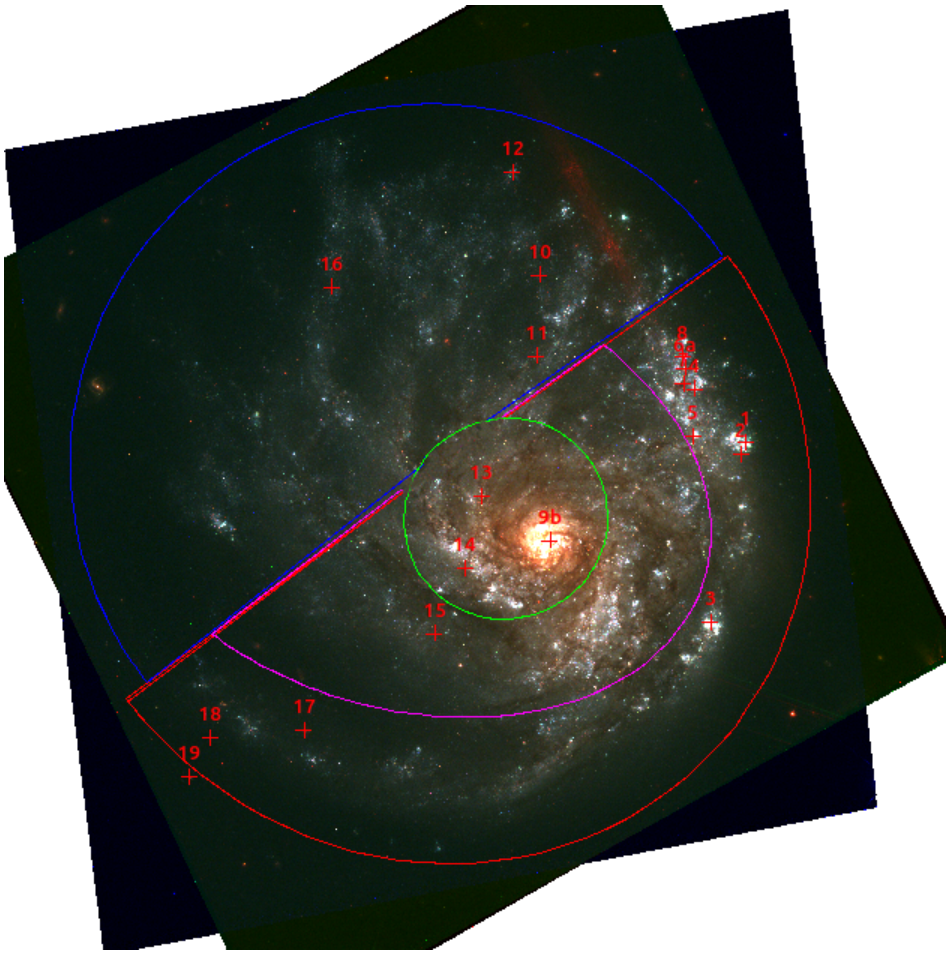

Figure 30: The location of the X-ray sources on the true color image of NGC2276 (red crosses). The number indicates their ID in the Anastasopoulou et al., 2019 catalogue.

ID_X	ID	$M_{MIST}(\times10^3 M_\odot)$	t_{MIST} (Myr)	$dust2_{MIST}$	$M_{BPASS}(\times10^3 M_\odot)$	t_{BPASS} (Myr)	$dust2_{BPASS}$	Region
1	615	$1.93^{+0.55}_{-0.31}$	$4.17^{+0.52}_{-0.64}$	$0.15^{+0.21}_{-0.11}$	$13.86^{+6.03}_{-5.60}$	$12.28^{+4.81}_{-5.20}$	$0.09^{+0.12}_{-0.07}$	West (out)
2	17885	$29.16^{+16.10}_{-10.34}$	$1125.67^{+1253.81}_{-711.82}$	$0.44^{+0.75}_{-0.33}$	$28.85^{+20.33}_{-15.10}$	$1392.49^{+1096.24}_{-1067.18}$	$0.27^{+0.67}_{-0.20}$	West (out)
3	20	$163.35^{+69.46}_{-47.71}$	$32.62^{+22.31}_{-10.96}$	$0.13^{+0.17}_{-0.09}$	$264.96^{+80.00}_{-81.35}$	$31.48^{+22.02}_{-15.55}$	$0.29^{+0.30}_{-0.20}$	West (out)
4	7505	$5.17^{+2.65}_{-1.48}$	$57.58^{+40.31}_{-21.31}$	$0.06^{+0.09}_{-0.05}$	$7.05^{+1.71}_{-1.52}$	$52.48^{+30.02}_{-19.41}$	$0.11^{+0.17}_{-0.08}$	West (out)
5	3327	$17.28^{+6.65}_{-4.90}$	$99.66^{+56.50}_{-39.72}$	$0.32^{+0.25}_{-0.20}$	$21.09^{+5.64}_{-4.35}$	$88.68^{+60.44}_{-44.91}$	$0.42^{+0.34}_{-0.28}$	West (out)
6^a	3933	$24.88^{+25.19}_{-10.06}$	$73.54^{+103.13}_{-41.03}$	$1.11^{+0.31}_{-0.48}$	$35.21^{+16.08}_{-10.03}$	$71.23^{+108.85}_{-34.06}$	$1.21^{+0.38}_{-0.57}$	West (out)
7	4464	$141.82^{+57.63}_{-44.05}$	$1715.64^{+1305.19}_{-946.61}$	$0.42^{+0.70}_{-0.29}$	$140.22^{+74.07}_{-63.60}$	$1723.43^{+1196.21}_{-867.89}$	$0.32^{+0.35}_{-0.22}$	West (out)
8	2184	$120.98^{+69.74}_{-47.04}$	$654.97^{+779.54}_{-542.61}$	$0.54^{+0.86}_{-0.45}$	$96.78^{+53.77}_{-25.29}$	$371.65^{+777.13}_{-223.88}$	$0.73^{+0.76}_{-0.63}$	West (out)
9^b	383	$108.69^{+31.37}_{-26.11}$	$121.88^{+61.48}_{-50.11}$	$0.62^{+0.27}_{-0.29}$	$127.57^{+30.59}_{-26.13}$	$128.93^{+73.91}_{-59.95}$	$0.58^{+0.44}_{-0.36}$	Center
10	15457	$1.93^{+1.69}_{-0.57}$	$54.85^{+75.05}_{-20.68}$	$0.06^{+0.09}_{-0.05}$	$2.32^{+0.72}_{-0.47}$	$38.68^{+31.74}_{-11.62}$	$0.11^{+0.14}_{-0.08}$	East
11	4670	$40.57^{+12.56}_{-10.25}$	$453.53^{+240.56}_{-188.23}$	$0.27^{+0.35}_{-0.20}$	$32.66^{+8.14}_{-6.26}$	$314.16^{+87.19}_{-97.37}$	$0.33^{+0.31}_{-0.22}$	East
12	20608	$1.19^{+0.16}_{-0.14}$	$33.14^{+4.19}_{-2.44}$	$0.03^{+0.04}_{-0.02}$	$0.30^{+0.09}_{-0.07}$	$3.53^{+0.85}_{-1.10}$	$0.23^{+0.19}_{-0.15}$	East
13	5144	$22.40^{+11.43}_{-7.22}$	$75.70^{+46.87}_{-30.83}$	$1.15^{+0.26}_{-0.33}$	$29.87^{+9.86}_{-7.48}$	$53.94^{+56.56}_{-24.87}$	$1.37^{+0.31}_{-0.41}$	Center
14	27082	$18.10^{+10.62}_{-6.05}$	$749.42^{+896.48}_{-427.14}$	$0.54^{+0.58}_{-0.39}$	$14.93^{+16.89}_{-6.47}$	$606.98^{+1369.67}_{-385.35}$	$0.38^{+0.58}_{-0.28}$	Center
15	36659	$7.15^{+3.73}_{-3.13}$	$422.81^{+365.24}_{-236.09}$	$0.39^{+0.42}_{-0.27}$	$4.99^{+2.98}_{-1.92}$	$256.39^{+178.57}_{-152.30}$	$0.36^{+0.41}_{-0.25}$	West (in)
16	26641	$8.70^{+4.82}_{-3.91}$	$300.94^{+251.23}_{-163.87}$	$0.35^{+0.35}_{-0.23}$	$6.29^{+3.04}_{-2.34}$	$180.33^{+150.66}_{-103.92}$	$0.31^{+0.34}_{-0.21}$	East
17	2677	$224.37^{+99.41}_{-83.88}$	$2010.23^{+1094.32}_{-722.92}$	$0.26^{+0.35}_{-0.18}$	$171.76^{+125.77}_{-80.13}$	$1387.45^{+1085.20}_{-697.27}$	$0.29^{+0.40}_{-0.20}$	West (out)
18	-	-	-	-	-	-	-	West (out)
19	38	$929.22^{+50.66}_{-101.53}$	$727.45^{+555.65}_{-377.86}$	$1.15^{+0.57}_{-0.41}$	$924.54^{+55.41}_{-104.09}$	$687.50^{+117.28}_{-108.61}$	$1.15^{+0.17}_{-0.16}$	West (out)

Table 7: Cluster parameters obtained by PROSPECTOR SED fitting for the best-matching sources with the X-ray catalogue of Anastasopoulou et al., 2019 (the ID_X refers to their identification on that catalogue). X-ray source #18 does not have a match with our catalogue.

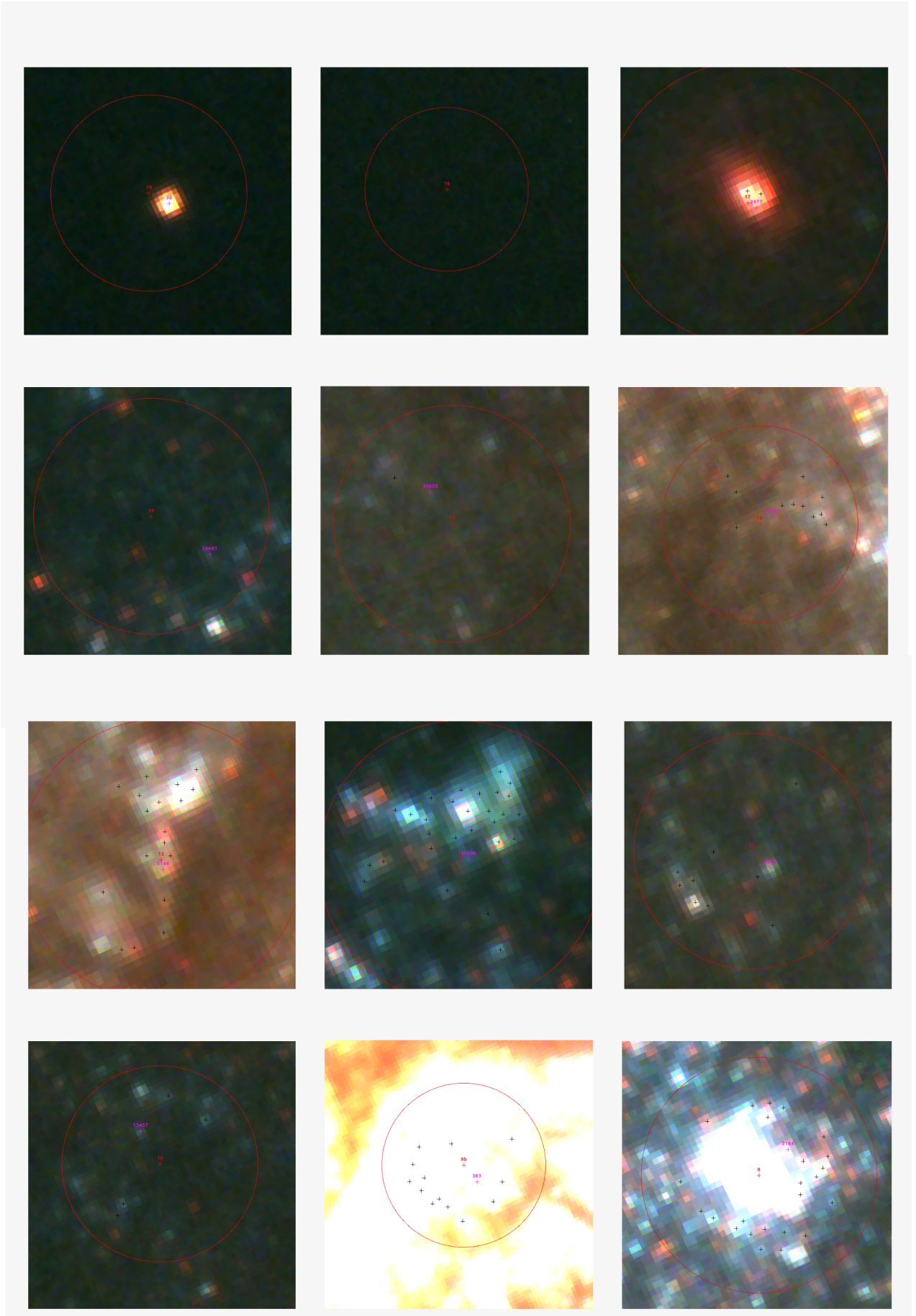

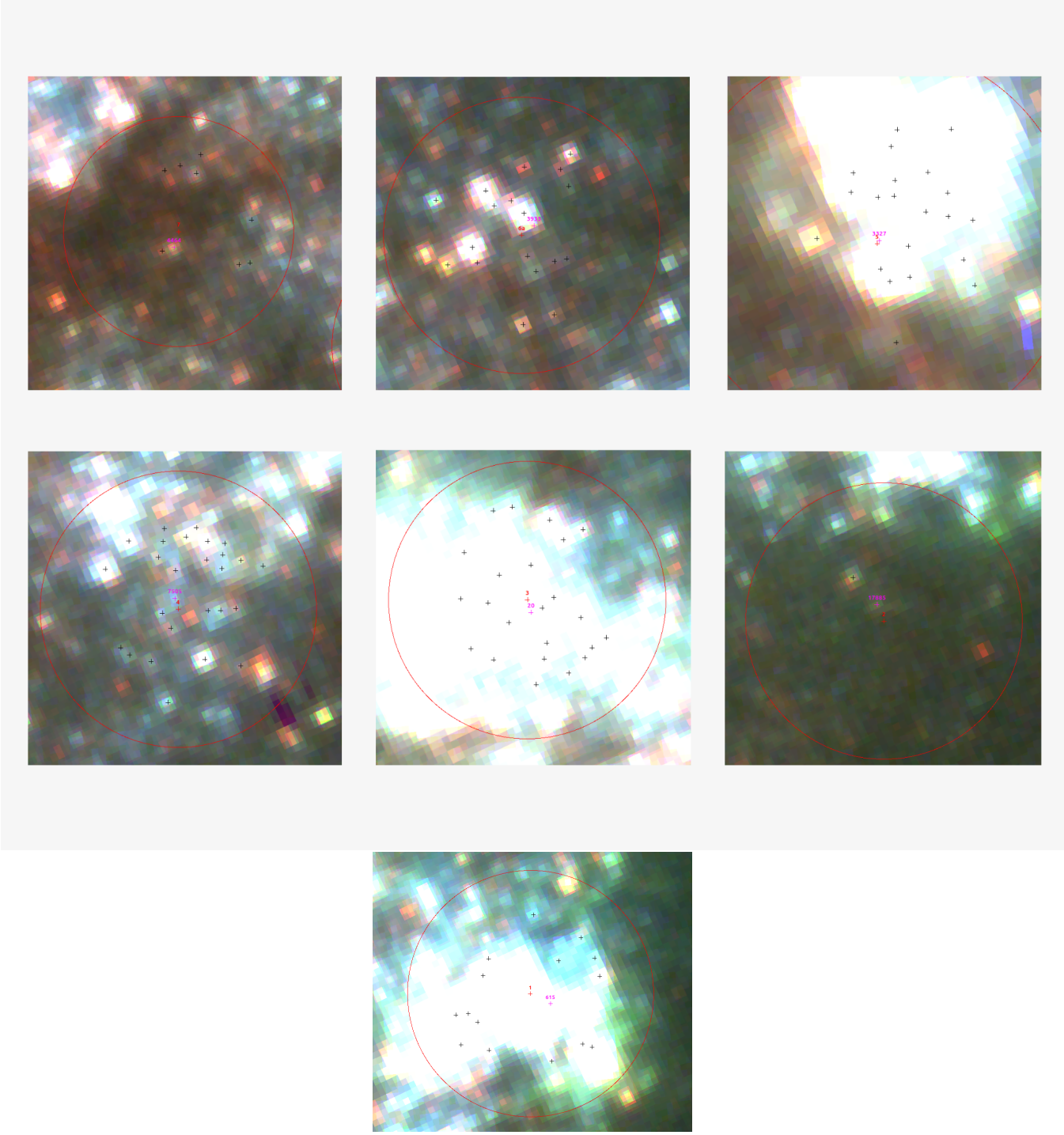

Figure 31: Cross-matching of the current clusters catalogue (Section 4) with the X-ray sources catalogue of Anastasopoulou et al., 2019 (red crosses) in a 1 arcsec radius ($\sim$ 200 pc) (red circle). The numbering of the X-ray sources refers to their ID in the catalogue of Anastasopoulou et al., 2019 (ID_X on table 5). The best-matched sources from our catalogue (magenta crosses) are identified by their ID in our catalogue. All other candidate sources within the search area can also be seen (black crosses). Most interesting sources are sources 6a and 9b which are an IMBH candidate and the galactic nucleus respectively. Additionally, source 18 has no matches.

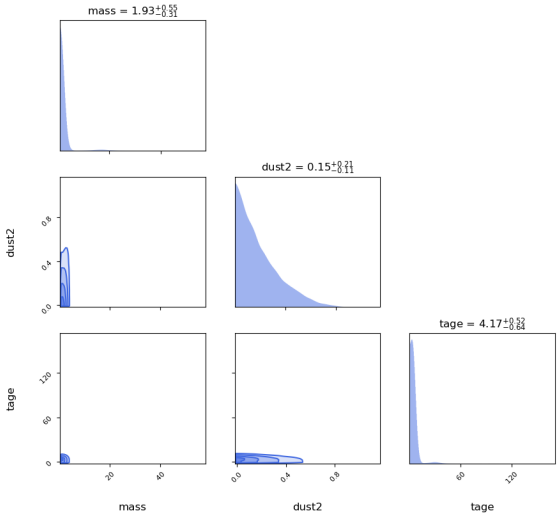

(a) Corner plots (MIST)

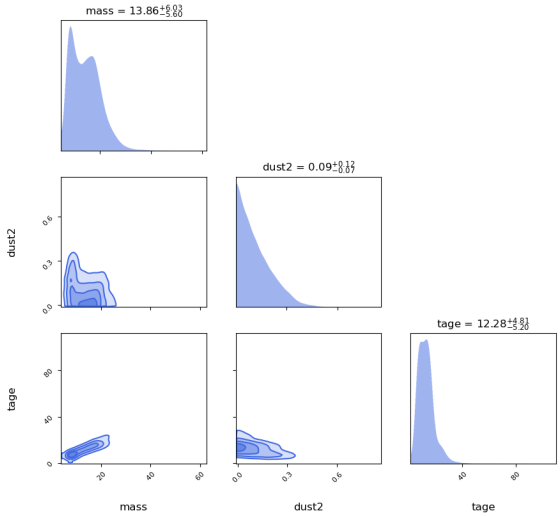

(b) Corner plots (BPASS)

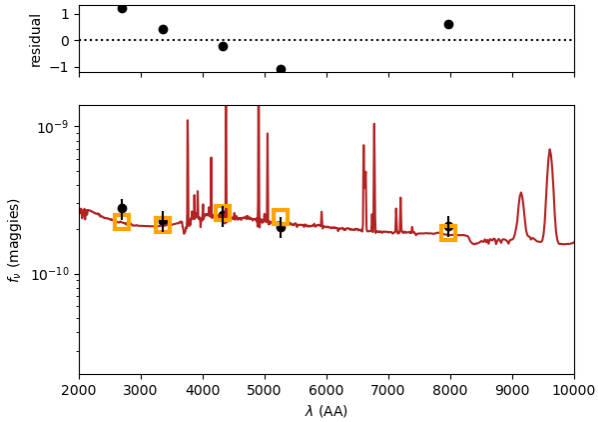

(c) Best-fit spectrum (MIST)

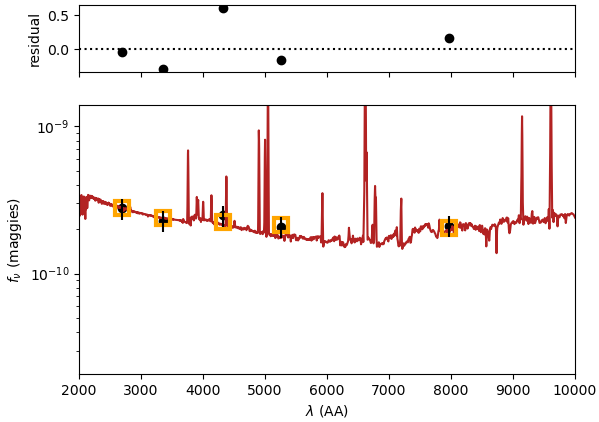

(d) Best-fit-spectrum (BPASS)

Figure 32: Corner plots (above) and best-fit spectra (bellow) for the cluster with ID_X 1 (ID 615), fitted using MIST (left) or BPASS (right) isochrones.

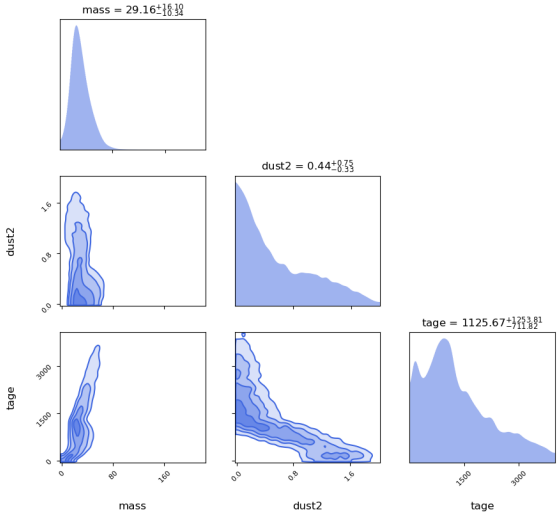

(a) Corner plots (MIST)

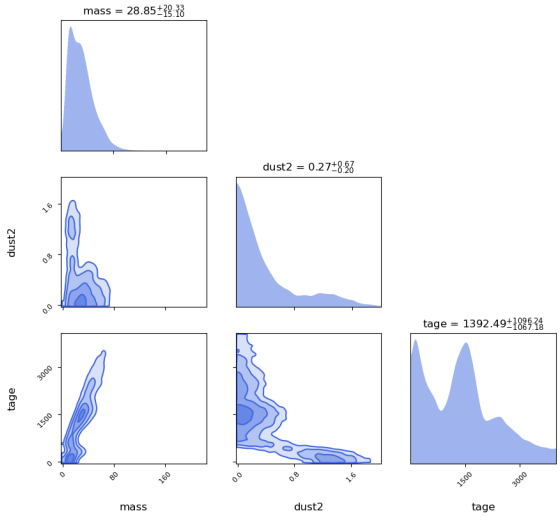

(b) Corner plots (BPASS)

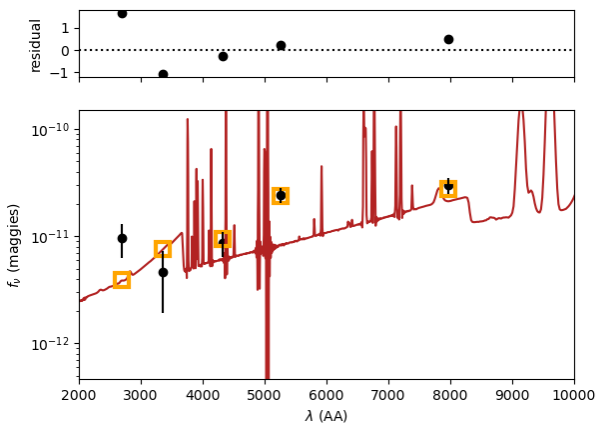

(c) Best-fit spectrum (MIST)

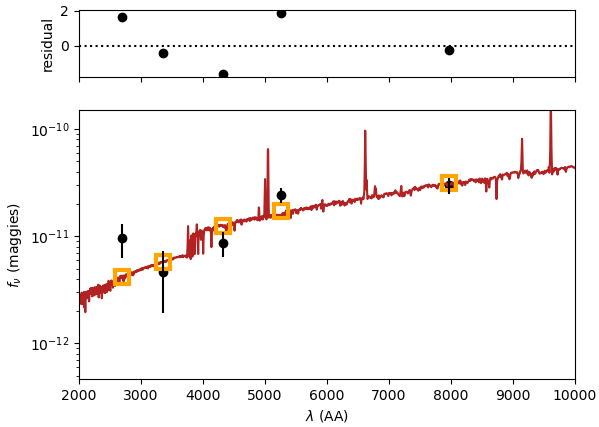

(d) Best-fit-spectrum (BPASS)

Figure 33: Corner plots (above) and best-fit spectra (bellow) for the cluster with ID_X 2 (ID 17885), fitted using MIST (left) or BPASS (right) isochrones.

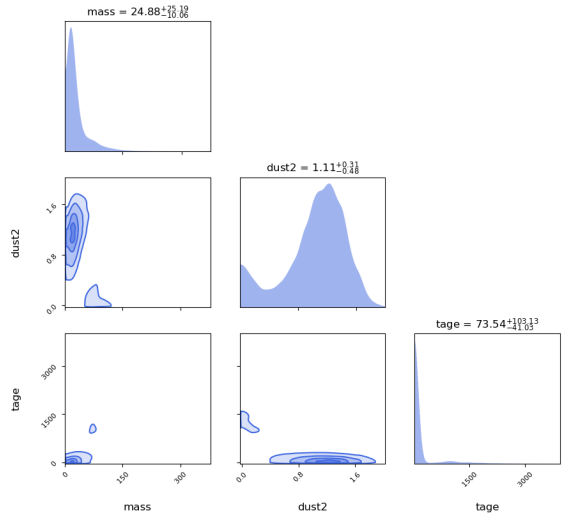

(a) Corner plots (MIST)

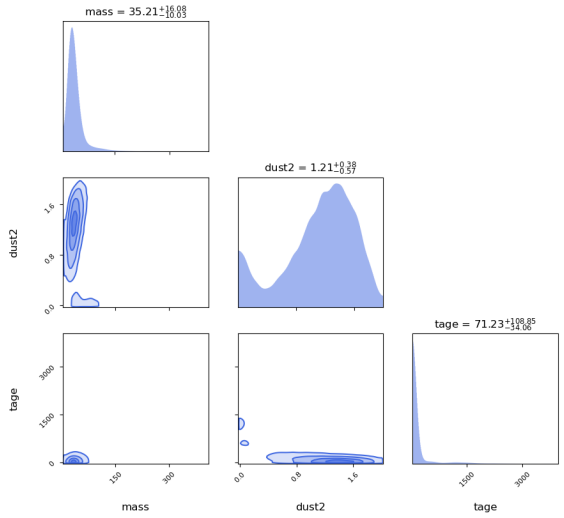

(b) Corner plots (BPASS)

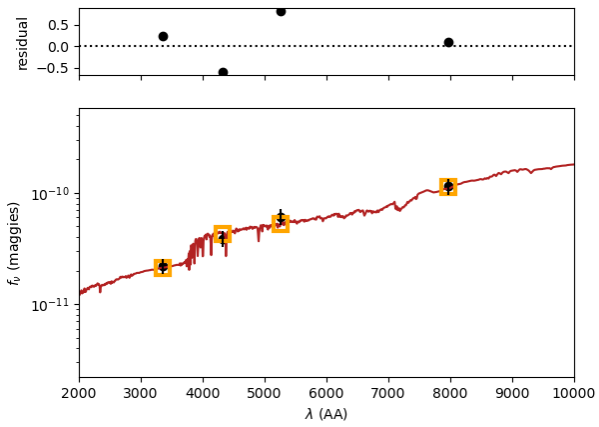

(c) Best-fit spectrum (MIST)

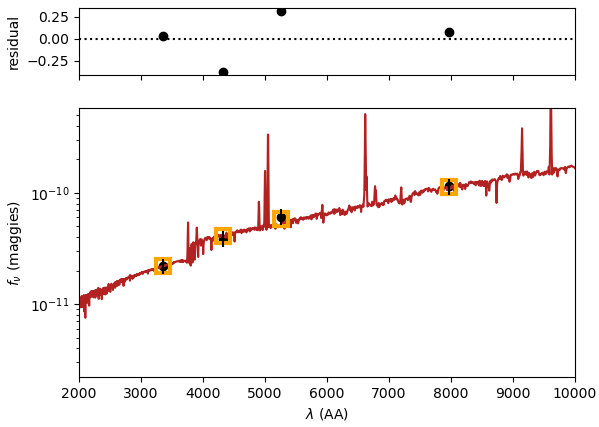

(d) Best-fit-spectrum (BPASS)

Figure 34: Corner plots (above) and best-fit spectra (bellow) for the cluster with ID_X 6^a (ID 3933), fitted using MIST (left) or BPASS (right) isochrones. This X-ray source is hypothesized to contain an IMBH (Mezcua et al., 2018).

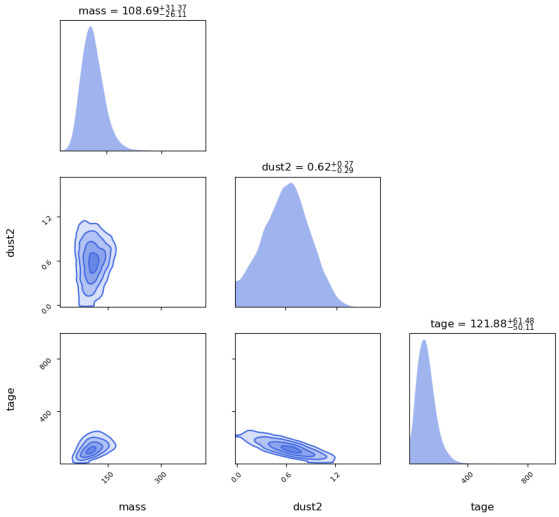

(a) Corner plots (MIST)

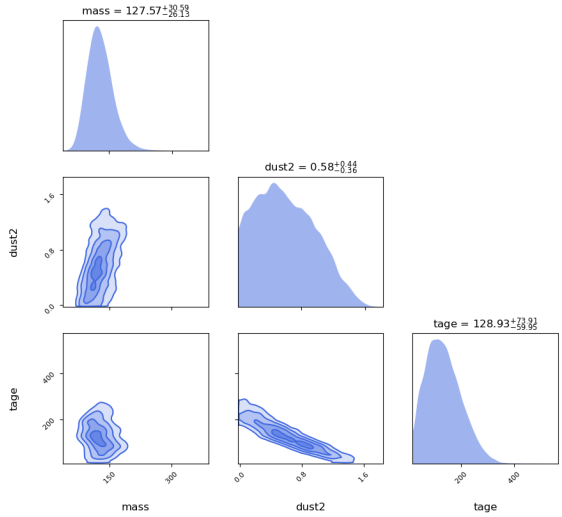

(b) Corner plots (BPASS)

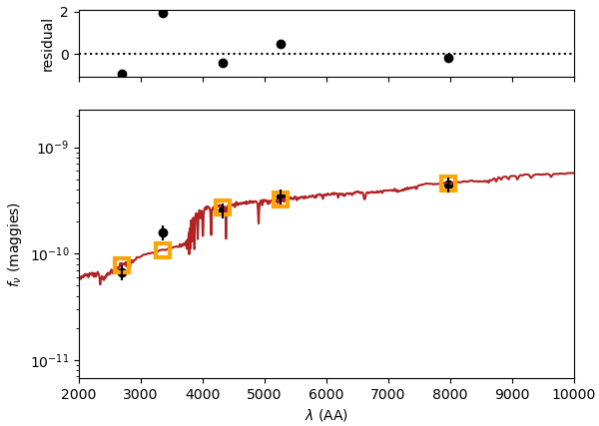

(c) Best-fit spectrum (MIST)

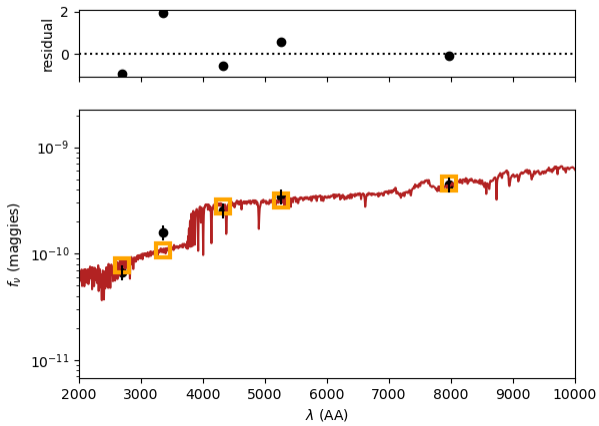

(d) Best-fit-spectrum (BPASS)

Figure 35: Corner plots (above) and best-fit spectra (bellow) for the cluster with ID_X 9^b (ID 383), fitted using MIST (left) or BPASS (right) isochrones. This X-ray source corresponds to the galactic nucleus.

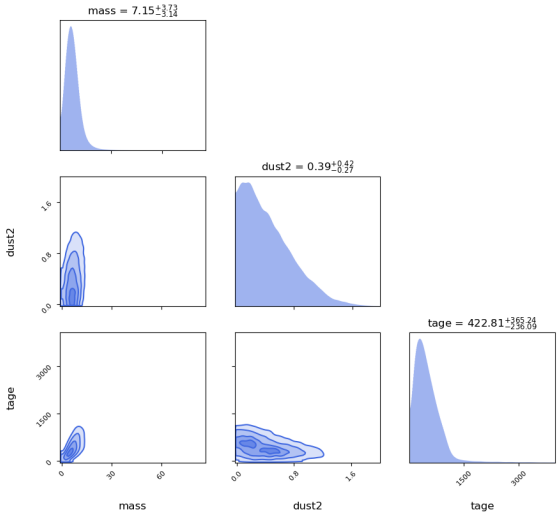

(a) Corner plots (MIST)

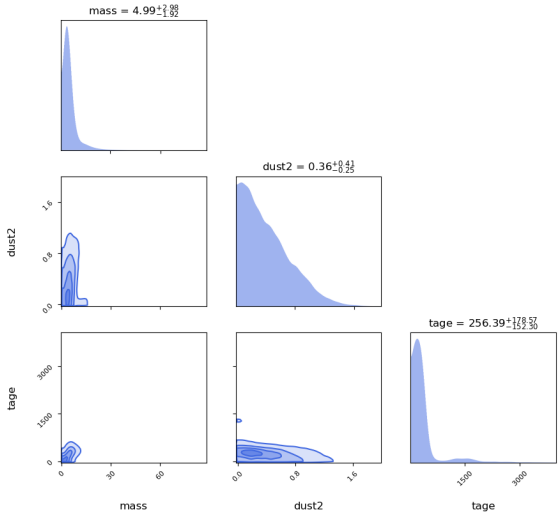

(b) Corner plots (BPASS)

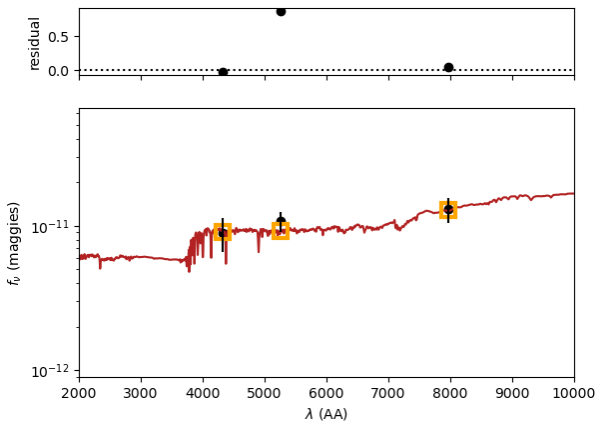

(c) Best-fit spectrum (MIST)

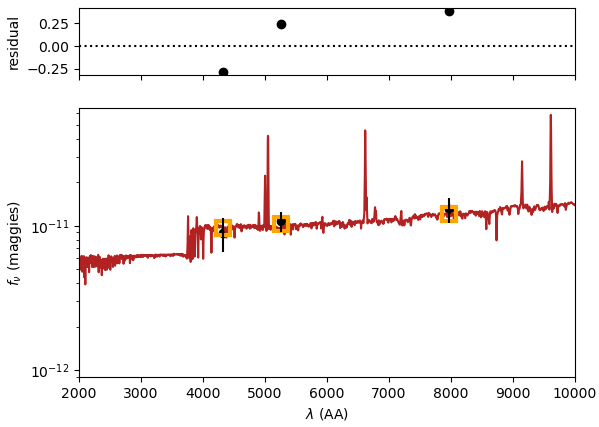

(d) Best-fit-spectrum (BPASS)

Figure 36: Corner plots (above) and best-fit spectra (bellow) for the cluster with ID_X 15 (ID 36659), fitted using MIST (left) or BPASS (right) isochrones. This fit includes only 3 bands since the photometry in F275W and F336W was bad.

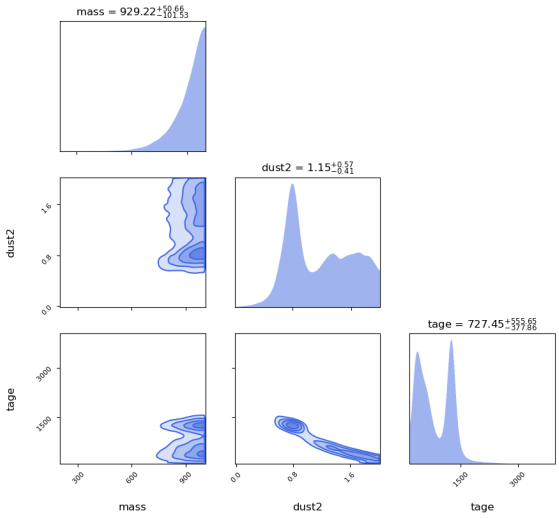

(a) Corner plots (MIST)

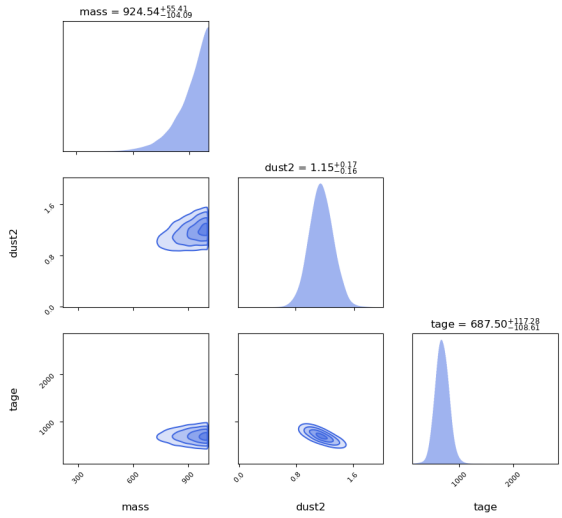

(b) Corner plots (BPASS)

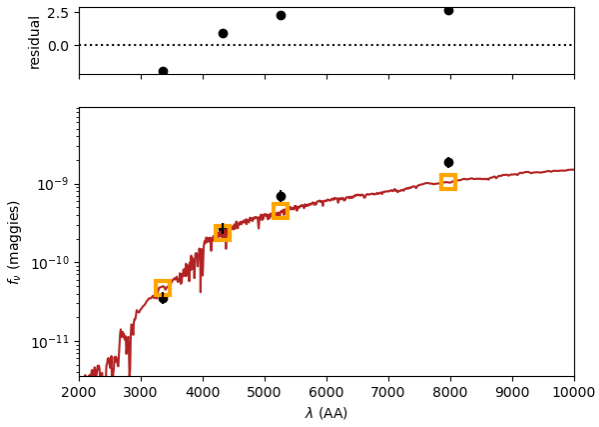

(c) Best-fit spectrum (MIST)

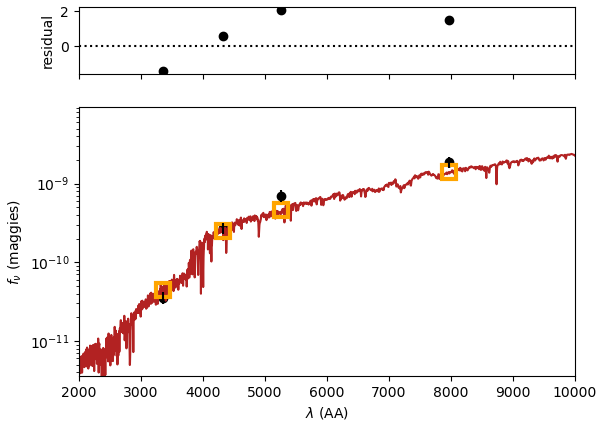

(d) Best-fit-spectrum (BPASS)

Figure 37: Corner plots (above) and best-fit spectra (bellow) for the cluster with ID_X 19 (ID 36659), fitted using MIST (left) or BPASS (right) isochrones. This fit includes only 4 bands since the photometry in F275W was bad. Notice that the mass posterior is truncated by the upper bound of the prior. That means that we would need to use a larger mass limit to get a correct fit, and the current fit is probably invalid. By looking at the source in the true-color image, its PSF profile looks rather extended for an isolated source and has high reddening comparatively to other sources. Those facts combined could indicate that this source is a background galaxy.

5 Results and Summary

As shown in Section 3.2, the evolutionary tracks seem to be in line with our data for both MIST and BPASS models, especially if we consider how those change when we change our assumption regarding metallicity and the wide range of dust extinction that clusters of a starburst galaxy could be experiencing. In color-color diagrams, it seems that the east side clusters have bluer colors than clusters in other regions of the galaxy. This trend disappears in the extinction-free Q-Q diagrams. That could be an indication of lower extinction for clusters in the east region comparatively to other regions. This is also consistent with the idea that these other regions experienced recent intense star formation due to compression and have therefore formed dense clusters with a high dust content. This is supported to some degree by the variation in the dust2 parameter obtained using SED fitting with a MIST model on the randomly selected clusters. For the east region clusters the extinction was found about an order of magnitude smaller compared to other regions. However, when using the BPASS model, this was not the case and the extinction was consistent in the different regions of the galaxy.

Regarding the star-cluster ages, most of the clusters seem to be concentrated near the $\sim 10 - 50$ Myrs part of the evolutionary tracks, both on the C-C and Q-Q diagrams. There are some clusters extending to ~ 1 Gyr ages up to ~ 5 Gyrs but those do not constitute the majority. The selection of attenuation law does not seem to greatly affect those results. Also, those results are consistent with both the BPASS and MIST tracks.

The CMDs and QMDs confirm that most clusters are concentrated near $\sim 10 - 100$ Myr ages. They also indicate that the observed star-clusters have masses in the $10^3 - 10^5 M_\odot$ range. East region clusters have larger absolute magnitudes compared to other regions. This is something we expected even from the true-color image of the galaxy and it indicates that they are older or less massive.

It is also very important to note that the cluster distributions in the aforementioned diagrams is in line with the BPASS model but could not be explained if we just considered the MIST model. Even if we consider different metallicity values, the BPASS tracks are still in better agreement with some of the data (for example see fig. 21). This confirms what we already know about the importance of binary evolution in stellar population composite spectra. It also highlights the importance of taking into account evolutionary models that incorporate binary evolution (for the time being the only such model available is BPASS). The parameters obtained by the fits were in agreement with our estimations from the C-C and Q-Q diagrams.

Further investigation of the trends of the cluster populations within the galaxy using SED fitting did not yield evidence for significant differences. This could be attributed to the small sample of clusters whose SEDs were fitted due to computational restrictions.

The last thing discussed in this investigation is the possible correlation between the characteristics of a cluster and the existance of an X-ray source in its vicinity. After matching our clusters catalogue with the X-ray catalogue of Anastasopoulou et al., 2019, we fitted the SEDs of the best-matched clusters. All of these sources turned out to be very massive, with masses $\sim 10 - 100 \times 10^3 M_\odot$ and ages ($\sim 10 - 100$ Myr). Some of them even exceed 100 Myr which is in disagreement with the expected XRB ages. There are many reasons this could be happening. Firstly, some of those sources

are located in very crowded areas of the galaxy. That means that they might be incorrectly matched with the X-ray source. There are also some X-ray sources matched with very faint optical sources that are expected to have somewhat unreliable photometry. This is evident from the number of sources with invalid photometry in the F275W (and even the F336W) filter. Nonetheless, in most cases the clusters in the vicinity of the X-ray sources are consistent with young ages, indicating that they are indeed HMXBs, especially in the west side of the galaxy. There are also some sources that could possibly be background sources or LMXBs.

Regarding sub-galactic scales, no significant difference is evident for the parameters of the clusters associated with the X-ray sources. This holds for both MIST and BPASS models. However, as already mentioned, there is an abundance of X-ray sources in crowded regions of the outer western spiral, which also contains a population of bright, blue optical sources. Many of these sources are not included in our analysis due to their unreliable photometry due to confusion.

A Attenuation Laws

To take into account the dust's effect on the observed spectrum, we considered two attenuation laws. An attenuation law describes the relationship between the average extinction $\langle \frac{A_\lambda}{A_V} \rangle$ (where A_λ is the extinction at the wavelength λ in magnitudes and is normalized by the extinction at the optical, A_V) and the optical slope $R_V \equiv \frac{A_V}{E(B-V)}$ (where $E(B-V)$ is the color excess defined as $E(B-V) \equiv A(B) - A(V)$, therefore describing how much larger the extinction is at the blue filter versus the optical filter).

A.1 Cardelli Attenuation Law

One parametrization for that relationship was proposed by Cardelli et al., 1989. If we define $x \equiv \lambda^{-1} \mu m^{-1}$, the parametrization is:

$$\left\langle \frac{A_\lambda}{A_V} \right\rangle = a(x) + b(x)\frac{1}{R_V}$$

where:
For $0.3\mu m^{-1} \leq x \leq 1.1\mu m^{-1}$ (infrared):

$$a(x) = 0.574x^{1.61}$$
$$b(x) = -0.527x^{1.61}$$

For $1.1\mu m^{-1} \leq x \leq 3.3\mu m^{-1}$ and $y \equiv x - 1.82$ (NIR-optical):

$$a(x) = 1 + 0.17699y - 0.50447y^2 - 0.02427y^3 + 0.72085y^4 + 0.01979y^5 - 0.77530y^6 + 0.32999y^7$$
$$b(x) = 1.41338y + 2.28305y^2 + 1.07233y^3 - 5.38434y^4 - 0.62251y^5 + 5.30260y^6 - 2.09002y^7$$

For $3.3\mu m^{-1} \leq x \leq 8\mu m^{-1}$ (ultraviolet):

$$a(x) = 1.752 - 0.316x - \frac{0.104}{(x-4.67)^2 + 0.341} + F_a(x)$$
$$b(x) = -3.090 + 1.825x + \frac{1.206}{(x-4.62)^2 + 0.263} + F_b(x)$$

where:
For $5.9\mu m^{-1} \leq x \leq 8\mu m^{-1}$:

$$F_a(x) = -0.04473(x-5.9)^2 - 0.009779(x-5.9)^3$$
$$F_b(x) = -0.2130(x-5.9)^2 + 0.1207(x-5.9)^3$$

and for $x < 5.9$:

$$F_a(x) = F_b(x) = 0$$

For $8\mu m^{-1} \leq x \leq 10\mu m^{-1}$ (far-UV):

$$a(x) = -1.073 - 0.628(x-8)0.137(x-8)^2 - 0.070(x-8)^3$$
$$b(x) = 13.670 + 4.257(x-8) - 0.420(x-8)^2 + 0.374(x-8)^3$$

A.2 Calzetti Attenuation Law

Calzetti et al., 2000 provide a different parametrization. Specifically, the parametrization is the following:
For $0.45\mu m^{-1} \leq x \leq 1.56\mu m$ (infrared-optical):

$$\begin{aligned} a(x) &= 1 \\ b(x) &= 2.659\,(-1.857 + 1.040x) \end{aligned}$$

For $1.56\mu m^{-1} \leq x \leq 8.33\mu m^{-1}$ (optical-far UV):

$$\begin{aligned} a(x) &= 1 \\ b(x) &= 2.659\left(-2.156 + 1.509x - 0.198x^2 + 0.011x^3\right) \end{aligned}$$

Both of these laws have been derived empirically (for a review of attenuation laws see Salim and Narayanan, 2020 and references within).

The two attenuation curves are show in fig. 38. The most apparent difference is the prominent bump on the Cardelli curve in the UV area. This peak is located at 2175Å and is absent in the Calzetti curve. Even though the origin of the bump is not totally understood, there is evidence that small grains of graphite or polycycle aromatic hydrocarbons (PAHs) are responsible (see Shivaei et al., 2022 and references within).

Some studies suggest that the strength of the bump is reduced even to near zero values, depending on the geometry of the dust and radiative transfer effects (Salim and Narayanan, 2020). The width of the bump is approximately 1000Å but the peak has been found to vary with a deviation of ∼5Å. This deviation on the peak's location was found to be uncorrelated with the width of the bump but correlated with the slope of the attenuation curve. Wider bumps usually indicate denser environments (Salim and Narayanan, 2020). The Calzetti attenuation law was derived by a sample of starburst galaxies, and is therefore usually used when studying them.

When calculating the average extinction using any of these laws, the value of R_V can vary, depending on our assumptions regarding the dust characteristics. In the case of Cardelli parametrization, a value of $R_V = 3.1$ for the slope is used, while for Calzetti parametrization, the value $R_V = 4.05$ is preferred. Both of these values have once again been determined empirically. It is also important to notice that we consider the extinction calculated using any of these two laws as a theoretical value carrying no error.

Lastly, when we use filters and want to calculate the extinction on a specific filter, we use the filter's effective wavelength[19]

[19]The effective wavelength of a filter is usually defined as the central wavelength of the filter's transmission curve.

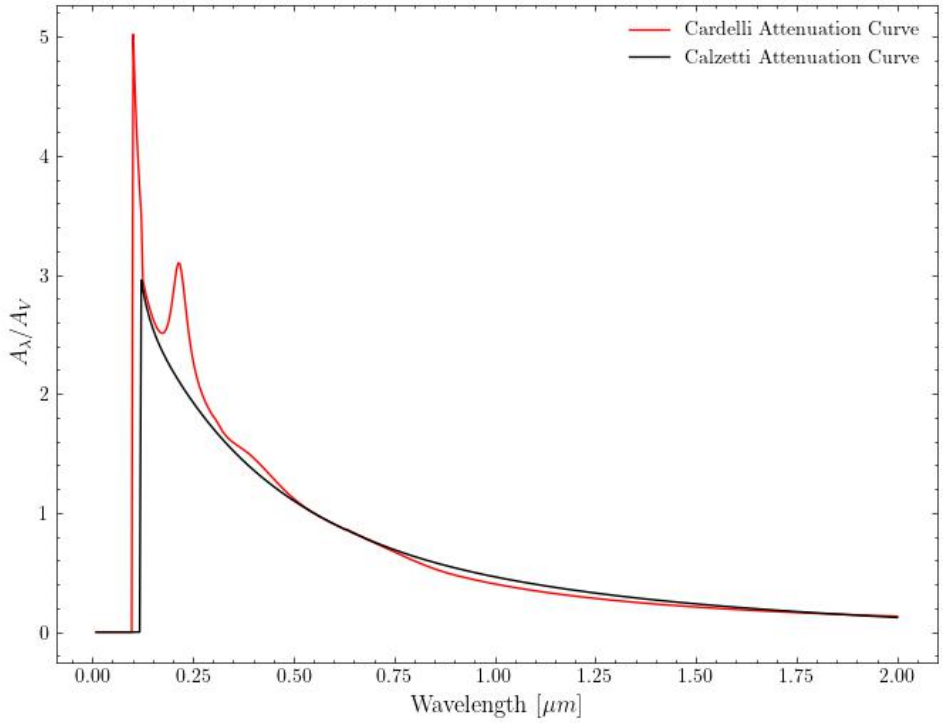

Figure 38: The Cardelli et al., 1989 (red) and Calzetti et al., 2000 (black) empirical attenuation curves, normalized at A_V. The Calzetti law is more suited to describing starburst galaxies while the Cardelli law was derived from Milky Way observations. Their most prominent difference is the 2175 Å bump.

B Reddening-Free Parameters (Q Parameters)

In our investigation we used the reddening-free parameters, also known as the Q parameters. These parameters were first introduced in Johnson and Morgan, 1953, and were defined as the interception of the line connecting reddened with un-reddened sources in color-color diagrams. If the color of an reddened source on the y-axis of the diagram is $m_1 - m_2$ and on the x-axis it is $m_3 - m_4$, while the colors of an un-reddened source are $(m_1 - m_2)_0$ and $(m_3 - m_4)_0$ respectively, then we have (see fig. 39):

$$m_1 - m_2 = (m_1 - m_2)_0 + E(m_1 - m_2)$$
$$m_3 - m_4 = (m_3 - m_4)_0 + E(m_3 - m_4)$$

where $E(m_1 - m_2)$ is the color excess between the filters 1 and 2, as defined in eq. (4)

By using the definition of the Q parameters (eq. (3)) together with the above equations on the definition we get:

$$Q = (m_1 - m_2)_0 + E(m_1 - m_2) - \frac{E(m_1 - m_2)}{E(m_3 - m_4)}[(m_3 - m_4)_0 + E(m_3 - m_4)] \Rightarrow$$
$$Q = (m_1 - m_2)_0 + E(m_1 - m_2) - \frac{E(m_1 - m_2)}{E(m_3 - m_4)}(m_3 - m_4)_0 - E(m_1 - m_2) \Rightarrow$$
$$Q = (m_1 - m_2)_0 - \frac{E(m_1 - m_2)}{E(m_3 - m_4)}(m_3 - m_4)_0$$

We can see that the parameter Q depends only on the reddening-free colors as well as the extinction law, which is something we have to assume and is therefore standard for all sources depending only on the filters.

The ability to define Q parameters even with three filters is what makes them extremely versatile and easy to use, even if there is a lack of filters used.

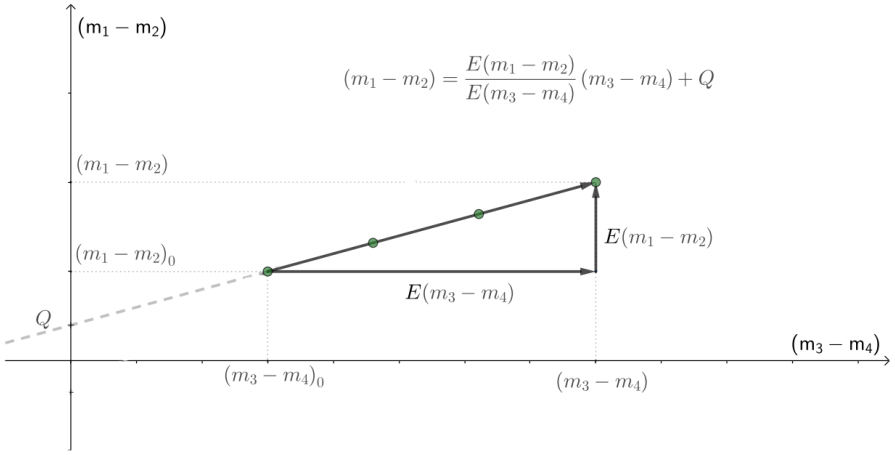

Figure 39: Calculation of the reddening-free Q parameters. The Q parameter is the intercept of the line between te un-reddened colors and the reddened ones. Credit: Aidelman and Cidale, 2023

C Photometry with DOLPHOT

C.1 Bad-pixel Masking and Background Calculation

As mentioned in 2.2, the very first step in image pre-processing is to mask bad columns and pixels. DOLPHOT has its own built in *mask* routine, which reads the data quality image[20] and masks all the pixels that are flagged as bad[21]. Cosmic rays are also masked that way. The masked pixels are ignored during the photometry.

Regarding the background, DOLPHOT's relevant module is *calcsky*. This module calculates a sky level for each pixel by calculating the robust mean intensity within a circular annulus centered on it. The masked pixels are not used in this calculation. To calculate the robust mean, an iterative process is used. In each iteration, pixels within a certain range from the previous mean are kept while the others are rejected. This is repeated until there are no pixels left to reject. Then the mean value of that final iteration is calculated and set as the sky value of the pixel. Finally, the image is smoothed before used in photometry to insure no steep variations of the background are left. This sky image can be used as the definitive sky value or just provide an initial guess for the sky, which will be re-calculated before the photometry[22]

C.2 Point-Spread Functions

No source appears point-like in a detector, no matter how far it is located. Even when a source should theoretically appear as a single point, if we look at an image of it in a CCD[23], its flux is not all concentrated in a single bright pixel, but rather follows a distribution which has a peak of maximum intensity at one pixel and that intensity is reduced when we get further away from it. We refer to this distribution as the Point-Spread Function (PSF).

There is a plethora of factors affecting how that distribution will look like. For instance, for ground based telescopes, the scattering of light by the atmosphere can vary in a timescale of seconds leading to an offset between the position where sequential rays arrive at the detector. Even if we eliminate that factor, for instance by using a space telescope like the HST, the sources would still not appear point-like. The reason for that is mainly the diffraction of light by the instrument's aperture. Additionally, the fact that the focal surface is a sphere rather than a plane will lead to even greater distortions as we move to the edges of the detector. Even the thickness of the detector can affect the PSF at the specific location due to charge diffusion effects. Because of the reasons mentioned, obtaining accurate PSFs for a detector can be very hard.

Knowing the PSF for a detector is very important since it can allow for very accurate photometry. For instance, if we know that the PSF follows a 2-D Gaussian profile, we can fit it on our data and then integrate it to get a very accurate value for the total flux of the source. Some of the most used models for PSFs are the following:

- GAUSS:

$$f(r) \sim \exp(-r^2)$$

[20]This is provided as an extension to the data image by STScI.

[21]Vignetted regions are also marked in more recent data.

[22]In our case we set the parameter *FitSky* to 2 which uses the sky image as an initial guess and re-calculates it before the photometry. This setting is suggested for crowded fields.

[23]Of course that is true for any kind of detector.

- MOFFAT:
$$f(r) \sim \frac{1}{(1+r^2)^a}$$
where a is usually 1.5 (then we call the profile MOFFAT15) or 2.5 (which is called a MOFFAT25 profile)

- LORENTZ/HUBBLE:
$$f(r) \sim \frac{1}{1+r^2}$$

- KINGc:
$$f(r) = \begin{cases} \left(\frac{1}{1+r^2} - \frac{1}{1+c^2}\right), & \text{if } z \leq c \\ 0, & \text{if } z \geq c \end{cases}$$
where c is known as the concentration parameter and takes the values 5, 15, 30 or 100. Another PSF profile that is commonly used is the sum of the GAUSS and the LORENTZ profiles.

Rather than providing an analytic profile and then fitting it, we can also provide a PSF in the form of a *fits* file, giving the intensity of the PSF at each pixel. This is called a *quantized* PSF since it has an intensity value for every pixel.

The quantized PSF function fitting has some important differences to the analytic models. The way the fitting works is as follows: after the center of the source is located[24], a PSF centered on that location is scaled (to minimize the χ^2 of the fit) and then subtracted from the image. What we are left with is what is remaining from that subtraction and is called the residual of that source. Then the counts are calculated in the following manner:

$$\text{counts} = \frac{\sum \text{residual} \times \text{PSF}/\sigma^2}{\sum \text{PSF}^2/\sigma^2} \tag{7}$$

where we sum on every pixel within a user-defined radius (as discussed more thoroughly in C.4)

C.3 Dolphot Point-Spread Functions Library

Since the PSFs do not vary a lot between observations with the same filter for the WFC3/UVIS detector, DOLPHOT uses its own library of (discrete) PSFs (unique for each filter) when performing PSF fitting photometry in an image taken with that detector[25]. As discussed in Dolphin, 2000, the recipe used for creating the PSF library for each filter, is the following:

- Using detector data, calculate synthetic (subsampled) Tiny Tim PSFs for different subpixel centerings.
- Apply a charge difussion correction (this accounts to smoothing the subsampled PSF with a Gaussian kernel)
- Apply a quantum efficiency correction. Quantum efficiency is the conversion rate of incident photons on the CCD to electrons.
- Repeat this process at different positions for each cheap. That will account for the spatial variation of the PSF due to distortion.

[24] In reality fitting and center location are done simultaneously as described in C.4

[25] In general, DOLPHOT can fit analytic PSFs but this is disabled for WFC3/UVIS images. It can also calculate new PSFs for each image but this is not suggested.

C.4 Star Detection and Fitting

First step on the star detection process is subtracting the sky image. Then an iterative process begins[26]. In each iteration (or pass), the brightest peaks are detected. Then a PSF is fitted for each detected source and then subtracted from the image. After the subtraction DOLPHOT does another peak detection, now for dimmer sources. If the photometry of source in the neighbourhood of a peak has changed significantly, this peak is flagged. In the next iteration, center detection and photometry are performed for the flagged peaks in the same manner. The user should use enough passes so that no sources are left undetected in the residual image.

In order to fit a PSF, the source's center location must be calculated. For that, first an initial guess for the center is calculated as a weighted average of the positions of the peak and adjacent pixels:

$$X_{center} = \frac{\sum x_i(R_i - R_{min})}{\sum(R_i - R_{min})}$$
$$Y_{center} = \frac{\sum y_i(R_i - R_{min})}{\sum(R_i - R_{min})}$$

where x_i and y_i are the coordinates of the pixels inside a predefined area centered on the peak, R_i is the residual at each pixel and R_{min} is the minimum residual determined by all the pixels inside that area. Using that initial guess, the algorithm assigns a goodness-of-fit value on it (it is defined below) and on its adjacent pixels by fitting PSFs centered around each of them, in the way described in the previous subsection. The process stops when the current center position yields the best fit. During this process, a robust median for the sky is calculated (instead of a robust mean) inside a specified ring surrounding the source[27] in the same manner as was done with *calcsky*. Then it is subtracted from the PSF.

Having obtained the PSF fit and the residual image we can calculate the signal, its error as well as the χ^2 of the fit. All of these values are calculated inside a circular aperture of a predefined *effective radius*[28]. These values are defined in the following manner:

$$\text{signal} = \frac{\sum_{x,y} R_{x,y} \times \text{PSF}_{x,y}/\sigma^2_{x,y} \times wt_{x,y}}{\sum_{x,y} \text{PSF}^2_{x,y}/\sigma^2_{x,y} \times wt_{x,y}}$$
$$\text{error} = \frac{\sqrt{\sum_{x,y} \text{PSF}^2_{x,y}/\sigma^2_{x,y} \times wt^2_{x,y}}}{\sum_{x,y} \text{PSF}^2_{x,y}/\sigma^2_{x,y} \times wt_{x,y}}$$
$$\chi^2 = \frac{\sum_{x_y} (R_{x,y} - \text{signal} \times \text{PSF}_{x,y})^2/\sigma^2 \times wt_{x,y}}{\sum_{x,y} wt_{x,y}}$$

where $R_{x,y}$ is the residual after sky subtraction, $PSF_{x,y}$ is the PSF value and $\sigma_{x,y}$ is the error of each pixel:

$$\sigma^2_{x,y} = R_{x,y} + \text{sky}_{x,y} + (\text{read noise})^2$$

[26]The number of iterations is defined by the user via the *SecondPass* parameter.

[27]The inner and outer radii of the ring are determing via the parameters *RSky1* or *RSky2* depending on the *FitSky* mode one is using.

[28]This is set by the *RAper* parameter for PSF fitting photometry. Even though the same aperture was used in the present investigation, one can determine a different aperture for the calculation of χ^2 via the *RChi* parameter.

The factor σ^2 is the same as $\sigma^2_{x,y}$ with the difference being that the former has an additional factor $c^2\text{signal} \times \text{PSF}^2_{x,y}$ in order to avoid very large values of χ^2 in the case of bright sources[29].

As for the weighting factor $wt_{x,y}$, it is equal to:

$$wt_{x,y} = R_{eff} + 0.5 - \sqrt{(x - x_c)^2 + (y - y_c)^2}$$

with x_c, y_c being the coordinates of the source's center and R_{eff} is the effective radius (the *RAper* DOLPHOT parameter).

Basically the signal is just eq. (7) weighted with $wt_{x,y}$ at each position. The error is calculated via error propagation. Finally, the χ^2 is the sum of the squared difference of the PSF and the residual, again weighted with $wt_{x,y}$. After obtaining the PSF fit, the SNR is calculated and the source is rejected if it is above a user defined limit[30].

Additionally, using these values the goodness-of-fit is determined, as:

$$\text{fit} = \frac{\text{signal}}{\text{error} \times \sqrt{\chi^2 + 0.1}}$$

The role of +0.1 inside the square root is to avoid infinite values in case a source is perfectly fitted. The reason for using that instead of just minimizing χ^2 is because that way even if the initial position guess is bad, the source will be found since we want a high SNR (that is why we essentially multiply $1/\chi^2$ with the SNR to get the goodness-of-fit). If say the inital position guess was on the wings of the source and a χ^2 minimization was used, the next guess could either go the correct way towards the actual peak of the source or head the wrong way down the wing until it hits another peak which will of course correspond to the wrong source.

Until now, we assumed that the same library PSFs were fitted for every image. That would be correct if the PSFs remained the same in each exposure but that is not the case. For that reason, after the first pass, an extra PSF fitting is performed to adjust the library PSFs for exposure-specific focus and tracking conditions that might have resulted in slightly different PSFs. That will mainly affect fainter sources since their photometry greatly depends on the shape of the PSF as can be seen from eq. (7). For that final adjustment, DOLPHOT selects some "PSF stars"[31] and calculates the average residuals around them using an iterative robust mean calculation. Since the mean residual counts sum up to some positive number, adding the residual to the library PSF will not conserve the counts (and of we course want our final PSF to have the same number of counts as the initial PSF, since we only want to see how the PSF shape changes in each exposure). In order to preserve the counts we multiply the sum of the PSF and the residual by a normalization constant:

$$\text{new PSF}_{x,y} = c(\text{PSF}_{x,y} + R_{x,y})$$

where:

$$\frac{1}{c} = 1 + \frac{\sum_{x,y} R_{x,y}}{\sum_{x,y} \text{PSF}_{x,y}}$$

[29]The value of c is chosen to provide a median χ^2 near one in the final photometry.

[30]That limit is set by DOLPHOT's *SigFind* parameter which sets the sigma detection threshold. Additionally, the *SigFinal* parameter cuts all sources below that detection threshold just before the final output.

[31]For the specific selection criteria see Dolphin, 2000.

Finishing the adjustment, the photometry of each PSF star is calculated until no PSF point changes significantly. Then DOLPHOT proceeds to the next pass.

Finally, after the last user defined pass, DOLPHOT combines the photometry of sources whose centers have a separation smaller than a user-defined limit[32]. DOLPHOT provides many more utilities that are not discussed here since they are not relevant to our investigation. To learn more about the software, reffer to Dolphin, 2000, A. Dolphin, 2011 and the manual on the program's website. Keep in mind that the Dolphin, 2000 paper is outdated at some points but the basics have not changed.

[32]That limit is defined via the *RCombine* parameter.

References

Aidelman, Y., & Cidale, L. S. (2023). Reddening-free q parameters to classify b-type stars with emission lines. *Galaxies 2023, Vol. 11, Page 31*, *11*, 31. https://doi.org/10.3390/GALAXIES11010031

Anastasopoulou, K., Zezas, A., Gkiokas, V., & Kovlakas, K. (2019). Do sub-galactic regions follow the galaxy-wide x-ray scaling relations? the example of ngc 3310 and ngc 2276. *Monthly Notices of the Royal Astronomical Society*, *483*, 711–733. https://doi.org/10.1093/mnras/sty3131

Bertelli, G., Bressan, A., Chiosi, C., Fagotto, F., Nasi, E., Bertelli, G., Bressan, A., Chiosi, C., Fagotto, F., & Nasi, E. (1994). *Theoretical isochrones from models with new radiative opacities*. https://ui.adsabs.harvard.edu/abs/1994A&AS..106..275B/abstract

Brown, G., & Gnedin, O. Y. (2021). Radii of young star clusters in nearby galaxies. *Monthly Notices of the Royal Astronomical Society*, *508*, 5935–5953. https://doi.org/10.1093/mnras/stab2907

Byler, N., Dalcanton, J. J., Conroy, C., & Johnson, B. D. (2017). Nebular continuum and line emission in stellar population synthesis models. *The Astrophysical Journal*, *840*, 44. https://doi.org/10.3847/1538-4357/aa6c66

Calzetti, D., Armus, L., Bohlin, R. C., Kinney, A. L., Koornneef, J., & Storchi-Bergmann, T. (2000). The dust content and opacity of actively star-forming galaxies. *The Astrophysical Journal*, *533*, 682–695. https://doi.org/10.1086/308692/FULLTEXT/

Cardelli, J. A., Clayton, G. C., Mathis, J. S., Cardelli, J. A., Clayton, G. C., & Mathis, J. S. (1989). The relationship between infrared, optical, and ultraviolet extinction. *ApJ*, *345*, 245. https://doi.org/10.1086/167900

Choi, J., Dotter, A., Conroy, C., Cantiello, M., Paxton, B., & Johnson, B. D. (2016). Mesa isochrones and stellar tracks (mist). i. solar-scaled models. *The Astrophysical Journal*, *823*, 102. https://doi.org/10.3847/0004-637x/823/2/102

Conroy, C. (2013). Modeling the panchromatic spectral energy distributions of galaxies. *Annual Review of Astronomy and Astrophysics*, *51*, 393–455. https://doi.org/10.1146/annurev-astro-082812-141017

Conroy, C., & Gunn, J. E. (2010a). Fsps: Flexible stellar population synthesis. *ascl*, ascl:1010.043. https://ui.adsabs.harvard.edu/abs/2010ascl.soft10043C/abstract

Conroy, C., & Gunn, J. E. (2010b). The propagation of uncertainties in stellar population synthesis modeling. iii. model calibration, comparison, and evaluation. *Astrophysical Journal*, *712*, 833–857. https://doi.org/10.1088/0004-637X/712/2/833

Conroy, C., Gunn, J. E., & White, M. (2009). The propagation of uncertainties in stellar population synthesis modeling. i. the relevance of uncertain aspects of stellar evolution and the initial mass function to the derived physical properties of galaxies. *Astrophysical Journal*, *699*, 486–506. https://doi.org/10.1088/0004-637X/699/1/486

de Vaucouleurs, G., de Vaucouleurs, A., Herold G., J. C., Buta, R. J., Paturel, G., & Fouque, P. (1991). Third reference catalogue of bright galaxies. *rc3*. https://ui.adsabs.harvard.edu/abs/1991rc3..book.....D/abstract

Dolphin. (2000). Wfpc2 stellar photometry with hstphot. *Astronomical Society of the Pacific*.

Dolphin, A. (2011). Dolphot/wfc3 user's guide version 2.0. http://purcell.as.arizona.edu/dolphot/

Dolphin, A., Dolphin, & Andrew. (2016). Dolphot: Stellar photometry. *ascl*, ascl:1608.013. https://ui.adsabs.harvard.edu/abs/2016ascl.soft08013D/abstract

Dotter, A. (2016). Mesa isochrones and stellar tracks (mist) 0: Methods for the construction of stellar isochrones. *The Astrophysical Journal Supplement Series*, *222*, 8. https://doi.org/10.3847/0067-0049/222/1/8

Draine, B. T., & Li, A. (2007). Infrared emission from interstellar dust. iv. the silicate-graphite-pah model in the post- spitzer era. *The Astrophysical Journal*, *657*, 810–837. https://doi.org/10.1086/511055

Eldridge, J. J., Izzard, R. G., & Tout, C. A. (2007). The effect of massive binaries on stellar populations and supernova progenitors. *MNRAS*, *384*, 1109–1118. https://doi.org/10.1111/j.1365-2966.2007.12738.x

Eldridge, J. J., & Stanway, E. R. (2009). Spectral synthesis including massive binaries. *MNRAS*, *400*, 1019–1028. https://doi.org/10.1111/j.1365-2966.2009.15514.x

Ferland, G. J., Porter, R. L., Hoof, P. A. V., Williams, R. J., Abel, N. P., Lykins, M. L., Shaw, G., Henney, W. J., & Stancil, P. C. (2013). *The 2013 release of cloudy*. http://arxiv.org/abs/1302.4485

Foreman-Mackey, D., Hogg, D. W., Lang, D., & Goodman, J. (2013). Emcee : The mcmc hammer. *Publications of the Astronomical Society of the Pacific*, *125*, 306–312. https://doi.org/10.1086/670067/XML

Fowler, J., Markwardt, L., Bourque, M., & Anderson, J. (2017). *Analysis of dragon's breath and scattered light detector anomalies on wfc3/uvis*. https://ui.adsabs.harvard.edu/abs/2017wfc..rept....2F/abstract

Gilfanov, M., Fabbiano, G., Lehmer, B., & Zezas, A. (2023). X-ray binaries in external galaxies. *Handbook of X-ray and Gamma-ray Astrophysics*, 1–38. https://doi.org/10.1007/978-981-16-4544-0_108-1

Girardi, L., Bressan, A., Bertelli, G., & Chiosi, C. (2000). Evolutionary tracks and isochrones for low- and intermediate-mass stars: From 0.15 to 7 $M_{\{\odot\}}$, and from $Z = 0.0004$ to 0.03. *Astronomy and Astrophysics Supplement Series*, *141*, 371–383. https://doi.org/10.1051/aas:2000126

Higson, E., Handley, W., Hobson, M., & Lasenby, A. (2019). Dynamic nested sampling: An improved algorithm for parameter estimation and evidence calculation. *Statistics and Computing*, *29*, 891–913. https://doi.org/10.1007/S11222-018-9844-0/TABLES/12

Hoffmann, S. L., Mack, J., Avila, R. J., Martlin, C., Bajaj, V., & Cohen, Y. (2021). The drizzlepac handbook - version 2.0. http://hsthelp.stsci.edu/

Johnson, B. D., Leja, J., Conroy, C., & Speagle, J. S. (2021). Stellar population inference with prospector. *The Astrophysical Journal Supplement Series*, *254*, 22. https://doi.org/10.3847/1538-4365/abef67

Johnson & Morgan. (1953). Fundamental stellar photometry for standards of spectral type on the revised system of the yerkes spectral atlas. *The Astrophysical Journal*, *117*, 313. https://doi.org/10.1086/145697

Kaaret, P., Alonso-Herrero, A., Gallagher, J. S., Fabbiano, G., Zezas, A., & Rieke, M. J. (2004). Displacement of x-ray sources from star clusters in starburst galaxies. *Monthly Notices of the Royal Astronomical Society*, *348*, L28–L32. https://doi.org/10.1111/J.1365-2966.2004.07516.X/2/348-2-L28-FIG003.JPEG

Koposov, S., Speagle, J., Barbary, K., Ashton, G., Bennett, E., Buchner, J., Scheffler, C., Cook, B., Talbot, C., Guillochon, J., Cubillos, P., Ramos, A. A., Johnson, B., Lang, D., Ilya, Dartiailh, M., Nitz, A., McCluskey, A., Archibald, A., … Angus, R. (2023). Joshspeagle/dynesty: V2.1.2. https://doi.org/10.5281/ZENODO.7995596

Kroupa, P. (2001). On the variation of the initial mass function. *Monthly Notices of the Royal Astronomical Society*, *322*, 231–246. https://doi.org/10.1046/j.1365-8711.2001.04022.x

Larsen, S. S., Larsen, & S., S. (2014). Baolab: Image processing program. *ascl*, ascl:1403.013. https://ui.adsabs.harvard.edu/abs/2014ascl.soft03013L/abstract

Mapelli, M., Ripamonti, E., Zampieri, L., & Colpi, M. (2011). Dynamics of massive stellar black holes in young star clusters and the displacement of ultra-luminous x-ray sources. *Monthly Notices of the Royal Astronomical Society*, *416*, 1756–1763. https://doi.org/10.1111/J.1365-2966.2011.18991.X/2/MNRAS0416-1756-F9.JPEG

Marigo, P., Girardi, L., Bressan, A., Groenewegen, M. A., Silva, L., & Granato, G. L. (2008). Evolution of asymptotic giant branch stars: Ii. optical to far-infrared isochrones with improved tp-agb models. *Astronomy and Astrophysics*, *482*, 883–905. https://doi.org/10.1051/0004-6361:20078467

Meynet, G., & Maeder, A. (2000). Stellar evolution with rotation v. changes in all the outputs of massive star models. *Astronomy and Astrophysics*, *361*, 101–120. http://arxiv.org/abs/astro-ph/0006404

Mezcua, M., Civano, F., Marchesi, S., Suh, H., Fabbiano, G., & Volonteri, M. (2018). Intermediate-mass black holes in dwarf galaxies out to redshift 2.4 in the chandra cosmos-legacy survey. *Monthly Notices of the Royal Astronomical Society*, *478*, 2576–2591. https://doi.org/10.1093/MNRAS/STY1163

Moeckel, N., & Clarke, C. J. (2011). Collisional formation of very massive stars in dense clusters. *Monthly Notices of the Royal Astronomical Society*, *410*, 2799–2806. https://doi.org/10.1111/J.1365-2966.2010.17659.X/3/MNRAS0410-2799-F4.JPEG

Poutanen, J., Fabrika, S., Valeev, A. F., Sholukhova, O., & Greiner, J. (2013). On the association of the ultraluminous x-ray sources in the antennae galaxies with young stellar clusters. *Monthly Notices of the Royal Astronomical Society*, *432*, 506–519. https://doi.org/10.1093/MNRAS/STT487

Ptak, A., Colbert, E., van der Marel, R. P., Roye, E., Heckman, T., & Towne, B. (2006). Optical counterparts of ultraluminous x-ray sources identified from archival hst wfpc2 images. *The Astrophysical Journal Supplement Series*, *166*, 154–187. https://doi.org/10.1086/505218/FULLTEXT/

Rangelov, B., Chandar, R., Prestwich, A., & Whitmore, B. C. (2012). X-ray binaries and star clusters in the antennae: Optical cluster counterparts. *Astrophysical Journal*, *758*, 99. https://doi.org/10.1088/0004-637X/758/2/99

Rangelov, B., Prestwich, A. H., & Chandar, R. (2011). The connection between x-ray binaries and star clusters in ngc 4449. *ApJ*, *741*, 86. https://doi.org/10.1088/0004-637X/741/2/86

Rasmussen, J., Ponman, T. J., & Mulchaey, J. S. (2006). Gas stripping in galaxy groups - the case of the starburst spiral ngc 2276. *Monthly Notices of the Royal Astronomical Society*, *370*, 453–467. https://doi.org/10.1111/j.1365-2966.2006.10492.x

Salim, S., & Narayanan, D. (2020). The dust attenuation law in galaxies. *Annual Review of Astronomy and Astrophysics*, *58*, 529–575. https://doi.org/10.1146/annurev-astro-032620-021933

Sanchez-Blazquez, P., Peletier, R., Jimenez-Vicente, J., Cardiel, N., Cenarro, A. J., Falcon-Barroso, J., Gorgas, J., Selam, S., & Vazdekis, A. (2006). Miles: A medium resolution int library of empirical spectra. *Monthly Notices of the Royal Astronomical Society*, *371*, 703–718. https://doi.org/10.1111/j.1365-2966.2006.10699.x

Schaller, G., Schaerer, D., Meynet, G., Maeder, A., Schaller, G., Schaerer, D., Meynet, G., & Maeder, A. (1992). *New grids of stellar models from 0.8-solar-mass to 120-solar-masses at z=0.020 and z=0.001.* https://ui.adsabs.harvard.edu/abs/1992A&AS...96..269S/abstract

Seward, F. D., & Charles, P. A. (2010). *Exploring the x-ray universe, second edition* (Vol. 9780521884839). Cambridge University Press. https://doi.org/10.1017/CBO9780511781513

Shivaei, I., Boogaard, L., Diaz-Santos, T., Battisti, A., Cunha, E. D., Brinchmann, J., Maseda, M., Matthee, J., Monreal-Ibero, A., Nanayakkara, T., Popping, G., Vidal-Garcia, A., &

Weilbacher, P. M. (2022). The uv 2175å attenuation bump and its correlation with pah emission at z 2. *Monthly Notices of the Royal Astronomical Society*, *514*, 1886–1894. https://doi.org/10.1093/MNRAS/STAC1313

Skilling, J. (2006). Nested sampling for general bayesian computation. *https://doi.org/10.1214/06-BA127*, *1*, 833–859. https://doi.org/10.1214/06-BA127

Skilling, J., Skilling, & John. (2004). Nested sampling. *AIPC*, *735*, 395–405. https://doi.org/10.1063/1.1835238

Speagle, J. S. (2020). Dynesty: A dynamic nested sampling package for estimating bayesian posteriors and evidences. *Monthly Notices of the Royal Astronomical Society*, *493*, 3132–3158. https://doi.org/10.1093/MNRAS/STAA278

Stanway, E. R., & Eldridge, J. J. (2018). Re-evaluating old stellar populations. *Monthly Notices of the Royal Astronomical Society*, *479*, 75–93. https://doi.org/10.1093/mnras/sty1353

Wolter, A., Esposito, P., Mapelli, M., Pizzolato, F., & Ripamonti, E. (2015). Ngc 2276: A remarkable galaxy with a large number of ulxs. *Monthly Notices of the Royal Astronomical Society*, *448*, 781–791. https://doi.org/10.1093/mnras/stv054

Zezas, A., & Fabbiano, G. (2002). Chandra observations of "the antennae" galaxies (ngc 4038/4039). iv. the x-ray source luminosity function and the nature of ultraluminous x-ray sources. *The Astrophysical Journal*, *577*, 726–737. https://doi.org/10.1086/342135

Zezas, A., Fabbiano, G., Baldi, A., Schweizer, F., King, A. R., Ponman, T. J., Rots, A. H., Zezas, A., Fabbiano, G., Baldi, A., Schweizer, F., King, A. R., Ponman, T. J., & Rots, A. H. (2008). Vizier online data catalog: Chandra sources in antennae galaxies, ngc 4038/39 (zezas+, 2006). *yCat*, J/ApJS/166/211. https://ui.adsabs.harvard.edu/abs/2008yCat..21660211Z/abstract

Zinn & R. (1985). The globular cluster system of the galaxy. iv. the halo and disk subsystems. *ApJ*, *293*, 424. https://doi.org/10.1086/163249

Zwart, S. F. P., McMillan, S. L., & Gieles, M. (2010). Young massive star clusters. *https://doi.org/10.1146/annu astro-081309-130834*, *48*, 431–493. https://doi.org/10.1146/ANNUREV-ASTRO-081309-130834